1-1-2017

Development Of A Programmed Electrospun Three Dimensional (3d) Nanofiber Collecter And It's Application To Orthopedic Implant Coatings

Liang Chen
Wayne State University,

DEVELOPMENT OF A PROGRAMMED ELECTROSPUN THREE DIMENSIONAL (3D) NANOFIBER COLLECTER AND IT'S APPLICATION TO ORTHOPEDIC IMPLANT COATINGS

by

LIANG CHEN

DISSERTATION

Submitted to the Graduate School

of Wayne State University,

Detroit, Michigan

in partial fulfillment of the requirements

for the degree of

DOCTOR OF PHILOSOPHY

2017

MAJOR: BIOMEDICAL ENGINEERING

Approved By:

Advisor: Wei-Ping Ren, MD., Ph.D.	Date
Mai T. Lam, Ph.D.	Date
Harini Sundararaghavan, Ph.D.	Date
Wen Chen, Ph.D.	Date

ACKNOWLEDGEMENTS

Firstly, I would like to express my sincere gratitude to my advisor Dr. Weiping Ren for the continuous support and guidance of my Ph.D. study and related research, for his patience, motivation, and immense knowledge. His guidance helped me in all the time of research and writing of this thesis. I could not have imagined having a better advisor and mentor for my Ph.D. study. Besides my advisor, I would like to thank the rest of my thesis committee, Dr. Mai T. Lam, Dr. Harini Sundararaghavan and Dr. Wen Chen, for their insightful comments and encouragement on tissue engineering and electronic device development, but also for the hard question, which incented me to widen my research from various perspectives.

My sincere thanks also goes to Dr. Wei Song and Ms. Tong Shi, whose experience and knowledge in materials science, tissue engineering and biology gave me lot guidance in my research. Without they precious support it would not be possible to conduct this research. Many thanks go to Dr. Nancy Jackson, and Christopher Bergum at Providence Hospital, Dr. Xin Wu and Ameer AL Shawk at Mechanical Engineering, Dr. Guangzhao Mao and Linxiao Xie at Chemical Engineering and Dr. Paul Begeman, Hanna Mazeh, Joseph Seta and all faculties in Biomedical Engineering for their great help to my research. Great thanks go to Christopher Rea for their help to my research, especially in device development.

Last but not the least, I am incredibly grateful thank to my family: my parents, my husband and my baby daughter for continued love, supporting me spiritually.

TABLE OF CONTECTS

LIST OF TABLES

LIST OF FIGURES

CHAPTER 1 BACKGROUND AND MOTIVATION

Problem Statements

Orthopedic implants are manufactured and routinely used to fix and support long bone or spine fractures, replace arthritic joints, and repair other orthopedic and maxillofacial defects (Goodman, Yao et al. 2013). Historically, the design of implants simply focused on mechanical properties, which should stabilize fractures, bear loading and facilitate more normal use of injured joints or limbs, and biological aspects were overlooked. It was believed if the implants were appropriately fixed, the bone would be self-healed (Goodman, Yao et al. 2013). However, every year in the United States about 600,000 fractures have delayed union and 100,000 fractures are nonunion (Bishop, Palanca et al. 2012). Some joint prosthetics cannot integrate to the surrounding bone (Aro, Alm et al. 2012). A long-term survival of implants needs early osseointegration (the formation of a direct interface between an implant and bone). Ryd et al.(Ryd 1992) reported that early implant loosening in both hips and knees might result in implants failure. Kärrholm et al. (Kärrholm J 1994) also concluded that the subsidence of the implant could increase the risk of aseptic loosening (AL).

The lack of early osseointegration also increases the risk of later aseptic loosening (AL), and is the main reason for the failure of total joint replacements (Kroell, Beaule et al. 2009, Bahraminasab 2012). Every year over 700,000 total joint replacements surgeries (hips and knees) are performed in the United States (Berry, Harmsen et al. 2002). Polymethylmethacrylate (PMMA) is a commonly used fixation material for cemented implants (Haboush 1996). As the cement

aged, the brittleness of PMMA creates debris (Howie, Haynes et al. 1993). At the same time the metallic implants (titanium or its alloy) them generate debris when they rub against other materials. Duo to wear debris accumulating around the implant and bone interface; macrophages differentiate into osteoclasts, which start osteolysis and enlarge the gap between the implants and bones resulting in loosening (Lennox, Schofield et al. 1987, Bullough, DiCarlo et al. 1988, Boos, Fink et al. 2008, White, Carsen et al. 2012). Early osseointegration can reduce wear debris, an inducement of AL, which is formed by rubbing. These facts stimulate scientists to pay more attention to modify the implants with biological and porous coatings (Figure 1). A “bone-like” implant interface between implant and bone could provide reliable mechanical support and robust bone healing, which could reduce AL via assisting early osseointegration.

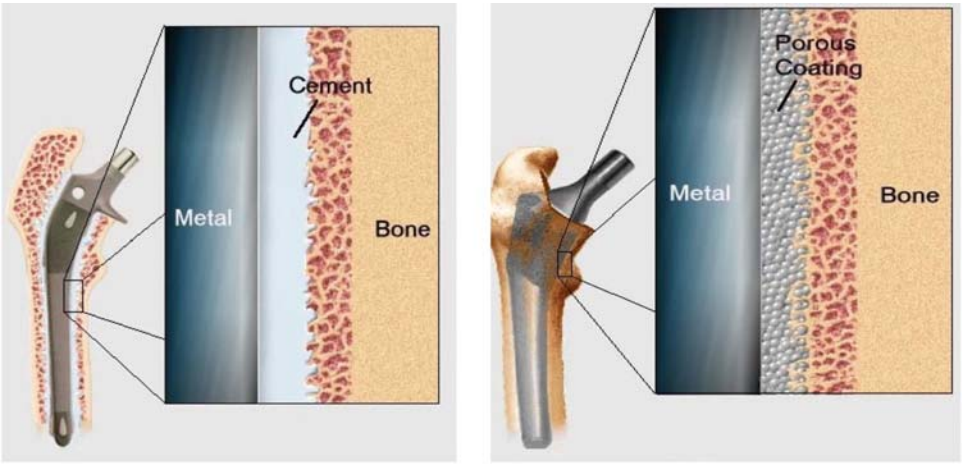

Figure 1. The cement fixation implant (left) and the implant with biological coatings

Bone tissue anatomy and circulations

An appropriated physiochemical and biologic milieu can boost the rate, quality and quantity of the early osseointegration. It is necessary to understand

the anatomy and physiology of the native bone for the design of an implant. This review would address the anatomy, physiology and repairing of the native tissue.

Bone is a highly mineralized connective tissue that is able to support the human body and maintain mineral homeostasis (Baroli 2009). Macroscopically, bone tissue can be classified into compact bone (cortical bone) and spongy bone (trabecular bone) (Baroli 2009). Compact bone is mainly responsible for supporting and protecting. It is formed by plenty of osteons. Blood vessels longitudinally pass through the osteon via the Haversian canal (Baroli 2009). The blood vessel inside the transverse Volkmann's canal connects each osteon. Thus, the Haversian canal and the Volkmann's canal form the blood vessel network for the bone's nutrition feeding and signal transduction (Baroli 2009). Spongy bone is a lightweight, highly porous tissue where riches in blood vessels and contains bone marrow. The main blood vessel, lymphatics and nerve fibers go through the center of spongy bone. It has the function of supplying nutrition for bone cells, hematopoiesis, and keeping mineral balance in body. The outer layer and coating of bone is the periosteum, which is a highly vascularized connective tissue. Not only can it connect one bone tissue with another or with muscle tissue, but also has the ability to regenerate bone during body development and bone healing because of the amounts of bone cells that accumulate at the inner layer of periosteum (Baroli 2009).

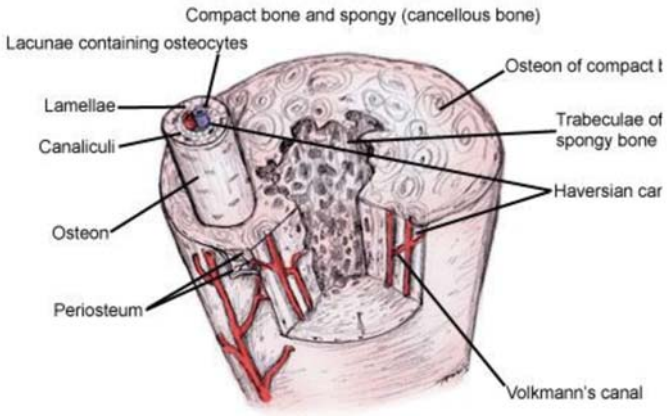

Figure 2. The anatomy of bone

The extracellular matrix of bone tissue is composed of with 65% minerals and 35% organic matrix (Baroli 2009). The organic material is mainly type I collagen (Col), which provides bone its flexibility and resilience. Col is important for cell adhesion and migration, and signal transduction of growth factors. The inorganic material consists of crystalline mineral hydroxyapatite (HA), which is precipitated in the collagen, and is responsible for the stiffness and strength of bone. HA nanocrystals are crucial for biomineralization and osseointegration (Wei and Ma 2004). The organic–inorganic constituents combine to provide a mechanical and supportive role in the body (Pramanik, Mishra et al. 2009).

There are several types of bone cells related to bone formation, such as mesenchymal stem cells (MSCs), osteoblasts (OB), osteocytes (OC), osteoclasts, and chondrocytes (Baroli 2009). The mesenchymal stem cells located in bone marrow are small, long and thin cells with a large nucleus. They have a great capacity of self-renewal and can differentiate into adipocytes, chondrocytes, osteoblasts, hepatocytes, and pneumoncytes. In the vascularization area, the

mesenchymal stem cells would differentiate into osteoblasts; but while they are under the non-vascularization area, they form chondrocytes (Uccelli, Frassoni et al. 2007). The osteoblasts are immature bone cells and produce osteoid matrices that are mainly composed of type I collagen, alkaline phosphatase, and other proteins (Xiao, Fu et al. 2007). After osteoblasts are trapped and deposited in the bone matrix, they eventually develop into mature bone cells, osteocytes. Like osteoblasts, the osteocytes can secrete hydroxyapatite, calcium carbonate and calcium phosphate bone matrix (Uccelli, Frassoni et al. 2007, Xiao, Fu et al. 2007). Additionally, they are very sensitive to mechanical strain and can secrete many growth factors to help cell proliferation and differentiation. The osteoclasts are large and multinuclear cells that are important for bone degradation and resorption (Baroli 2009).

Adult bones continuously undergo remodeling in order to maintain their integrity and biomechanical strength. The remodeling process is associated with two steps: osteoclasts resorption of bone and osteoblasts rebuilding of bone. This process happens in special vascularized structures called bone remolding units (BRUs) (Saran, Gemini Piperni et al. 2014). The BRUs recruit the osteoblasts and osteoclasts or their precursors and signal molecules from circulation to the site of remodeling. The BRUs facilitate the direct cell interactions between osteoblasts and osteoclasts, and secretion of receptor activator NF-κB ligand (RANKL) by osteoblasts promotes osteoclasts differentiation and activations (Baroli 2009, Saran, Gemini Piperni et al. 2014). It is crucial to keep a precise balance between the bone resorption and bone

formation (Saran, Gemini Piperni et al. 2014). Imbalance between these processes, such as an increase in bone resorption without adding bone formation, results in an onset of osteoporosis usually seen in post-menopausal women. The loss of bone mass and density cause weakening of bone strength and increase the risk of bone fracture.

In the event of injury, bone is able to regenerate to its original structure through several stages of healing, which are: impact-induced inflammation, granulation (primary soft callus formation), callus mineralization (hard callus formation), callus remodeling and concurrent modeling (Figure. 3) (Baroli 2009). When the fracture happens, the injured area is immediately invaded with blood that will form a blood clot or a hematoma. The hematoma will release various signaling factors and angiogenetic growth factors, which in turn recruit inflammatory cells such as macrophages and repairing cells including fibroblasts, osteoblasts, mesenchymal stem cells (MSCs) and vascular endothelial cells (Ferrara, Gerber et al. 2003, Brandi and Collin-Osdoby 2006, Golub, Kim et al. 2010). Meanwhile the fracture area is a hypoxic environment because of compromised blood supply, disruption of oxygen and acute necrosis of the surrounding tissue. Hypoxia is an important physiological signal in bone repair as it up regulates the VEGF expression by the osteoblasts that in turn promote endothelial cells (ECs) proliferation and differentiation (Ball SG 2007, Saran, Gemini Piperni et al. 2014). The ECs secrete osteogenic growth factor for osteogenesis (Brandi and Collin-Osdoby 2006, Ball SG 2007). In these conditions, osteoprogenitor cells and osteoblasts deposited close to the

undamaged bone form osteoids that are subsequently mineralized to form the granulation /soft callus around an injured area. The soft callus will undergo endochondral ossification bridging the fracture gap. Finally, the healing bone will undergo remodeling to restore its structure and mechanical strength.

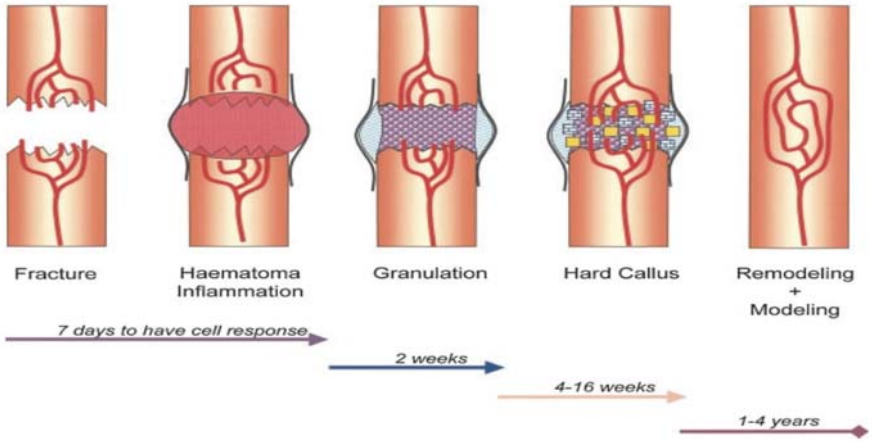

Figure 3. Schematic representation of bone healing phase and duration (Baroli 2009).

Current implant coatings

Many efforts have been done on implant surface coatings in order to add biologic properties to the implants and improve osseointegration. Calcium phosphate-like coatings have been used in the orthopedics because of their similar components to the native bone. Titanium (Ti) implants with HA coating in cementless hip replacements have been used to enhance bone ingrowth since 1987(Geesink RG 1987). Current studies found no significant improvement in clinical outcomes in patients with a cementless hip replacement as compared to those with a cemented hip replacement (de Jonge, Leeuwenburgh et al. 2008). The limitations of a HA coating include (1) a non-physiological surface of HA

coating leads to diminished initial osseointegration (Goosen JH 2008); (2) brittle nature (Song Y 2010); (3) poor adhesion strength (de Jonge, Leeuwenburgh et al. 2008) and (4) the lack of controllable drug release (Renwen Zhang 2004). Our previous study within 24h found about three quarter of erythromycin loaded onto a Ti implant with a HA coating was released (Ren, Zhang et al. 2010). Another coating is a biomolecule coating that is divided into three categories: layer-by-layer (LBL) coatings, hydrogel coatings and immobilization (Goodman, Yao et al. 2013). Hydrogel coatings are composed of simply immersing implants into a hydrogel solution with biomolecules. Many researches proved that collagen (Rammelt, Schulze et al. 2004, Sartori, Giavaresi et al. 2015), decorin (Stadlinger, Pilling et al. 2008), chondroitin sulphate (Stadlinger, Pilling et al. 2008) and BMP2 embedded hydrogel coating for titanium implants can enhance early bone remodeling around the implant and increase osseointegration (Dupont, Boerckel et al. 2012). However, it is difficult to control the loading efficiency and drug releasing kinetics. The LBL techniques repeatedly dip implants into polyelectrolye solutions with opposite charges to load the coating materials and biomolecules. It has the potential to carry dual molecules and to control the releasing kinetics through changing the number of layers and the properties of polyelectrolytes. Shah NJ et al. coated VEGF and BMP-2 to the surface of PCL/ β-TCP scaffolds via LBL to mimic the bone healing processes (Shah, Hong et al. 2012). Doped with these two proteins, the implant facilitated blood vessel ingrowth and bone formation (Shah, Hong et al. 2012). However, several barriers inhibited the board application of LBL techniques: (1) labor intensive and expensive, (2) toxic to

tissue, (3) mechanical instability (Goodman, Yao et al. 2013). Biomolecules including peptides and proteins immobilized onto the metallic implant surface utilize cross-linking or covalent bonding, which may alert bioactivity of molecules. Future developments of implant coatings should emulate the host environments that induce cell adhesion and osseointegration via released biomolecules.

Electrospinning Technology and Electrospun Nanofibers (NFs) Implant Coatings

The native microstructures of the extracellular environments (ECMs) of bone tissues are nano-fibrous collagen networks. The basic building block of bone is mineralized and highly ordered collagen I fibrils (Weiner S 1998), only a few nanometers thick (Fratzl P1 1992), with collagen. The collagen I fibrils are aligned and arranged to form a higher order structure until a complete bone tissue (Zhang R 2000, Li WJ 2001, White CA 2012). One of the promising technologies created to mimic bone nanoscale extracellular matrix (ECM) structure is electrospinning (Baker, Handorf et al. 2009).

Electrospinning was developed in the early 1930s and had applications in various industries, such as highly efficient filters, lightweight and protective cloth and battery cells (Katti, Robinson et al. 2004, Ramaseshan R 2006, K Fujihara A Kumar 2007). It uses an electrical charge to overcome the surface tension of a charged polymer solution, and form very fine (typically on the micro or nano-scale) fibers from a liquid (Reneker DH 1996). With the expanding availability of polymer materials electrospun NFs have been applied to tissue engineering as scaffolds, and its unique characteristics has drawn increased attention (Doshi J 1995). One of the characters is its high surface area, high mass to volume ratio

and a small inter-fibrous pore size with high porosity (Ifkovits, Sundararaghavan et al. 2009), which makes it an ideal matrix for cell adhesion and growth. In tissue engineering, the electrospun NFs also has been used as a controllable drug delivery device by embedding antibiotics, peptides, proteins and other drugs (Song, Yu et al. 2013). We have developed doxycycline (Doxy)-doped polycaprolactone/polyvinyl alcohol (PCL/PVA) NFs, which successfully inhibited bacterial infection up to 8 weeks in vivo by sustaining release of Doxy (Song, Yu et al. 2013). The potential application of NFs for the enhancement of osseointegration is promising but often is overlooked. Our previous works have demonstrated that Doxy-dope PCL/PVA NFs can improve osseointegration (Song, Seta et al. 2017). The bone-implant surface (%) in the NFs coated titanium implant groups was significantly higher ($p<0.05$) than the non-coated groups after implantation for 2, 4 and 8 weeks in a Staphylococus aurus infected tibia implantation rat model. Additionally, there are a few papers (Kohgo, Yamada et al. 2011) (Huang, Daniels et al. 2008) that demonstrated the NF structural cues alone can be used to create an osteogenic environment and that the cell attachment, proliferation, and differentiation of bone cells are influenced by the physiochemical properties of the NFs (Huang, Daniels et al. 2008). More efforts are needed to understand the interplay between the physiochemical natures of NFs and the fate of local bone cells.

Current Electrospinning Technologies to Form Three-dimensional (3D) Nanofibers and Limitations

One of limitations of electrospun NFs in tissue engineering is its dense, compact and flat structure. This structure inhibits further cell infiltration,

proliferation, and vascularization (Nam, Huang et al. 2007, Skotak 2011). There is still a technical challenge to fabricate loose, thick and bulky scaffolds (3D scaffolds) with controlled microstructures and properties (Ma 2011). It is well accepted that a defined 3D microenvironment and porous structure of NF scaffolds are critical for cell growth and tissue regeneration (Barthes, Ozcelik et al. 2014). Many efforts have been explored in past decades to prepare 3D porous and looser NF scaffolds. Salt leaching (Nam, Huang et al. 2007) has been used to create depth during electrospinning (Teo 2011). It sprinkles salt particles in a polymer solution during electrospinning. The salt would be built inside a thick NF scaffold. Finally, these particles would be washed out of the NF scaffold and leave a porous and thick NF scaffold (Nam, Huang et al. 2007). A similar technology is an ice crystal method. Ice crystals are formed inside of the NFs when NFs are under low temperature in order to freeze water molecules inside (Leong, Rasheed et al. 2009, Schneider O D 2009). Porous 3D NFs could be formed as soon as the temperature is increased and the ice crystals melted. The limitation of these methods is that they are time-consuming. The fiber formation is slow and the pore sizes may still be relatively small. Some methods are effective in reducing the deposition speeds of NFs. Miyamoto et al. applied a negatively charged electrode to neutralize the charged electrospinning jet. The polymer jet traveled slowly to the collector and formed a fluffy 3D NF scaffold (Miyamoto, Atarashi et al. 2009). However, the pore sizes were difficult to control with this method.

It has been demonstrated that collection methods act most effectively on constructing 3D fibers and manipulating the elaborate fibrous structure (Teo and Ramakrishna 2006). Some advanced collection techniques have been reported including wet electrospinning (Yokoyama 2009), rolling or stacking collectors (Pham, Sharma et al. 2006, Thorvaldsson, Stenhamre et al. 2008, Shim, Suh et al. 2009), and yarn (Smit 2005). These technologies can be used to prepare 3D NF scaffolds. For instance, the yarn technology uses a water bath as a collector instead of a flat metallic, grounded collector. Through water vortex, the NF yarns are collected in the basin below the vortex (Teo 2011). Some researchers use an organic solvent bath rather than a water bath because the organic solvent has a lower surface tension and the NFs would sink into the solvent and would be discharged immediately. In this condition, the deposition area would be smaller but the accumulating speed would be faster and would form 3D NFs as a result (Ki C S 2007). Using a micro-patterned collector is another collection technique, allowing the formation of highly porous NFs. Li et al. developed patterned static collectors consisting of conductive and non-conductive void spaces (Li D 2004, Li, Ouyang et al. 2005). NFs were aligned across a non-conductive void. These methods make it possible to form 3D NFs scaffolds in certain forms. However, the processing is relatively complex, slow, and difficult to be controlled and this process cannot create scalable, block scaffolds with an interconnected porous structure. An efficient and real-time 3D NFs fabrication method is still required and necessary for its further application in tissue engineering.

We have developed a novel 3D NFs collector with arranged, movable and electrically conductive needles on the tips of which electrospun NFs are gradually deposited and form 3D NF architecture (Wei S. 2017). We have compared these 3D NFS with 2D PCL NFs, and found that the 3D NFs assisted cell proliferation and infiltration. Based on this study, our goal is to develop the customized collector into an automatic electrospun NFs collector to fabricate 3D NFs and control the microstructure of NFs via accurately changing the velocities of collector movements. The objectives of this study are to determine whether the microstructures of 3D NFs are reproducible using this programmed collector, compare the responses of different cells when cultured on these 3D NFs with different pore sizes, and study the osseointegration ability of the 3D NFs as a drug delivery vehicle. The NFs could be utilized as implant coating materials to improve and satisfy various cell adhesion, growth and differentiation and to induce early osseointegration via controlled release of biomolecules.

CHAPTER 2 THREE-DIMENSIONAL (3D) POLYCAPROLACTONE (PCL) NANOFIBERS FABRICATED BY A NOVEL AUTOMATIC COLLECTOR AND ITS CHARACTERIZATION

Introduction

Background

Natural bone is a nano-fibrous network, which is a porous, highly mineralized and well-organized structure (S Weiner 1998). The basic unit is collagen I fibers (only a few nanometers thick) (Fratzl P 1992, Zhang R 2000). They are aligned and arranged to form a higher order structure unit of a basic bone matrix (Zhang R 2000, Li WJ 2002, White CA 2012). Various types of bone substitutes have been developed in order to assist bone healing. Although many of them have the desired mechanical strength, they have insufficient abilities of osteoconduction and osteoinduction to enhance bone ingrowth (Goodrich JT 2012). The ideal substitute should mimic the extracellular matrix environment (ECM) of the bone tissue, the nano-fibrous network, and aim to help bone cells adhesion, growth and differentiation onto the implants (Jang JH 2009, Holzwarth and Ma 2011).

Electrospun nanofibers have similar diameters as compared to the natural fibers of the bone ECM (Sundararaghavan HG 2010). In addition, nanofibers have a higher surface to volume ratio and high porosity and interconnectivity that are critical to facilitate cell attachment and growth (Pham, Sharma et al. 2006, Teo and Ramakrishna 2006, Yokoyama 2009). These characters ensure electrospinning as one of the promising technologies to mimic the nanoscale extracellular matrix of bone (Baker, Handorf et al. 2009). Porous structure is

another requirement of a scaffold. The nutrition and waste of cells should be transported and removed through the pores (Rampichová M 2013). Cells growth and differentiation demand a porous structure. It is well acknowledged that different cells require different pore sizes (Rampichová M 2013). For example, vascularization happens at pore sizes over 300 μm in the bone tissue (Karageorgiou V 2005); while fibroblasts prefer a pore size of 6-20 μm (Lowery JL 2010). Thus, ideal electrospun NFs scaffold should have three-dimensional shape and macroscale pores, which provide sufficient space for cell infiltration and differentiation (Blakeney BA 2011). In this aspect, traditional electrospun NFs are limited by their dense and tightly packed structure, which only allows superficial penetration of the cells.

Many methods have been used in an effort to create 3D NFs with larger pore sizes. Some focused on changing parameters of electrospinning like an external force on a spinneret jet, electric charge and a magnetic field (Teo 2011); others used a solid support, which eventually was leached out, to introduce large pores, such as salt particles (Nam, Huang et al. 2007), ice crystals (Teo 2011), and photo patterning (Goodman, Yao et al. 2013). In addition, advanced techniques like wet electrospinning (Yokoyama 2009), yarn (Smit 2005) and rolling or stacking collectors (Pham, Sharma et al. 2006) are suitable for mass production. However, most of them fail to control the desired porosity and pore size. Moreover, these techniques are time consuming and expensive that greatly limits intended application. Therefore, it is essential to develop real-time and one-

step 3D NFs fabrication technology that can be used to control the matrices and geometry of formed nanofibers during electrospinning.

The principle of 3D NFs collector

The working mechanism of electrospinning is that driven by high voltage, a charged polymer jet overcomes its surface tension and deposits onto low potential targets in the form of numerous nanofibers. Conventionally, the solidified fibers deposit on the flat surface with equipotential density. However, if a sharp needle projects from the surface, a corona discharge would favorable build up at the tip of the needle (Wei S. 2017). As a result, the local electric field around the needle tip creates strength much higher than the surrounding conductor, resulting in an acceleration of free electrons to a high velocity, which ionizes neutral air molecules (Wei S. 2017). Thus, the charged polymer jet prefers to deposit onto the sharp tip of the needle during the electrospinning (Figure 4).

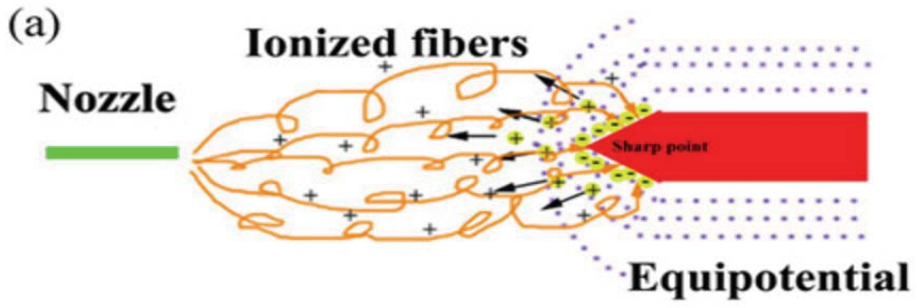

Figure 4. A diagram of electrospinning setup aims to explain the phenomenon of the nanofibers depositing on the needle tip (Wei S. 2017).

According to this mechanism, we have designed a collecting device with numerous movable needles where electrospun NFs are gradually deposited to form 3D architectures (Figure 5 (a)). Figure 5 (b) shows a 2D cross-sectional

view of electrospinning build-up between the spinneret and a grounded collector. A discharge prefers to occur in the vicinity of a sharp point where a highly curved region exists, for instance, projecting point of a needle or edging corner, shown as point A or B/C in Figure 5 (b). Unlike conventional electrospinning that lays down a uniform deposition, the electric field vectors in the vicinity of the collector in this study majorly target two fractions—the projecting points of needles (A) and the edging corner of the platform (B/C), which enforces the deposition of spinning nanofibers along the alignment of B-A-C and allows a triangle-shaped fiber sheet formation, as shown in Figure 5 (b, 1). When two points are more prominent on the surface of collector such as points D and E, the spinning fibers are deposited to these points giving a wave-shaped fiber sheet formation (Figure 5 (b)). Figure 5 (c) shows the photograph of a typical 3D nanofibers scaffold during electrospinning with fibers directly deposited on pierced needles and platform corners to form a wave shape.

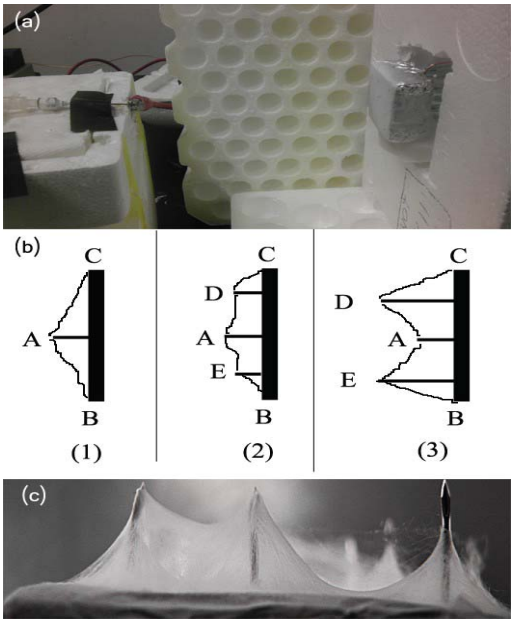

Figure 5 . Fabrication of PCL 3D nanofiber scaffolds. (a) electrospinning setup with self-designed needle pierced collector. (b) Illustration in cross-sectional view of electrospun fibers built-up between the spinneret and needle -collector. (c) Photograph of collected fibers deposited along needles and platform during electrospinning.

Our strategy is to build up a loose and hollow structured 3D scaffold constructed by stacking multi-layers of fiber-sheet into bulk. We performed multiple rounds of electrospinning steps to construct different fiber sheets along various angles. When the collector was fully covered by a deposited fiber sheet, the needles' positions were re-adjusted by gradually pushing those pierced needles forward. At the same time, a new fiber sheet would start depositing on the tips. Each round lasted the same time. After several rounds, 3D NFs architectures were gradually built on the surface of the collector (Figure 6). Thus, using the coronal charge effect provides a simple and feasible approach to develop the 3D nanofibers.

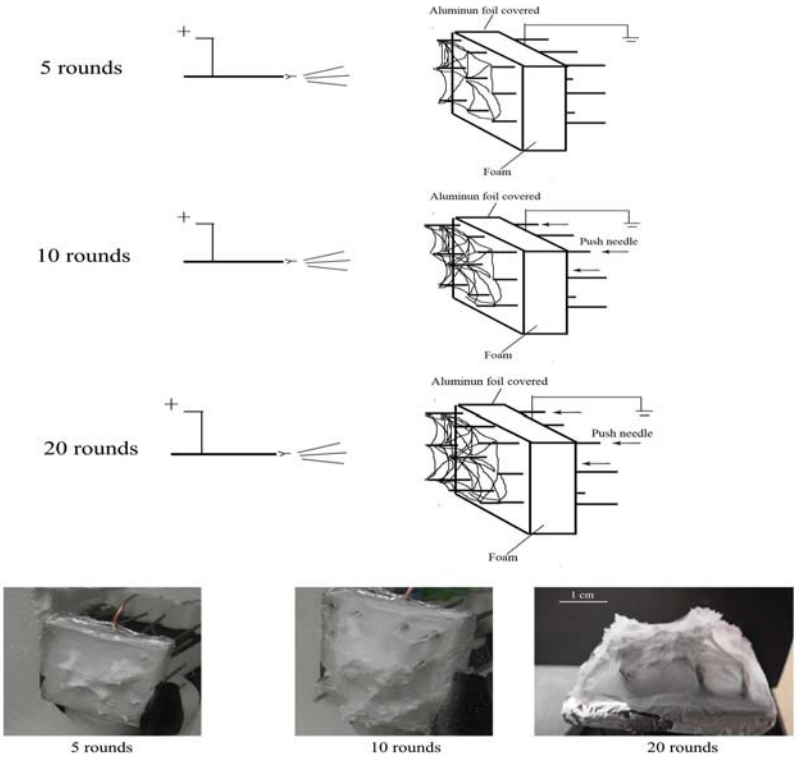

Figure 6. Multiple rounds (5, 10 and 20) for building 3D nanofibers on a needle collector.

We have confirmed that in comparison to the 2D PCL nanofibers, the 3D PCL nanofibers have a looser microstructure and larger pore sizes via scanning electron microscopy (Figure 7)(Wei S. 2017). The pore sizes of 2D NFs was in the range of 0 -1μm^2; and about 80% of pores in 2D NFs was smaller than 0.1 μm^2 (Figure 7c). The 3D NFs had a much looser structure and the pores were mainly in the range of 0.1 to 10 μm^2 (Figure 7a,c).

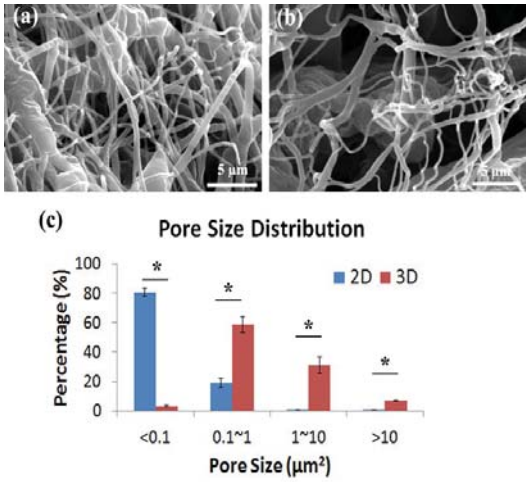

Figure 7. The cross-sectional 2D (a) and 3D(b) of PCL nanofibers by SEM. (c) pore size distribution calculated by Image J (n=3), $p<0.05$ (Wei S. 2017)

In addition, we found these looser structures of the 3D nanofibers elevated murine pre-osteoblastic MC3T3-E1 cells infiltration, proliferation and differentiation (Figure 8) (Wei S. 2017). The preosteoblast cells infiltrated the entire 3D PCL nanofibers, while they only spread on the surface of 2D nanofibers (Figure 8 a and b). A significantly higher cellular proliferation was also discovered on 3D NFs at 7-day culture than that on the 2D NFs ($p<0.01$, Figure 8d). The looser structure further increased the differentiation level of the cells, which had a significantly higher alkaline phosphatase (ALP) concentration on 3D NFs ($p<0.01$, Figure 8e) (Wei S. 2017).

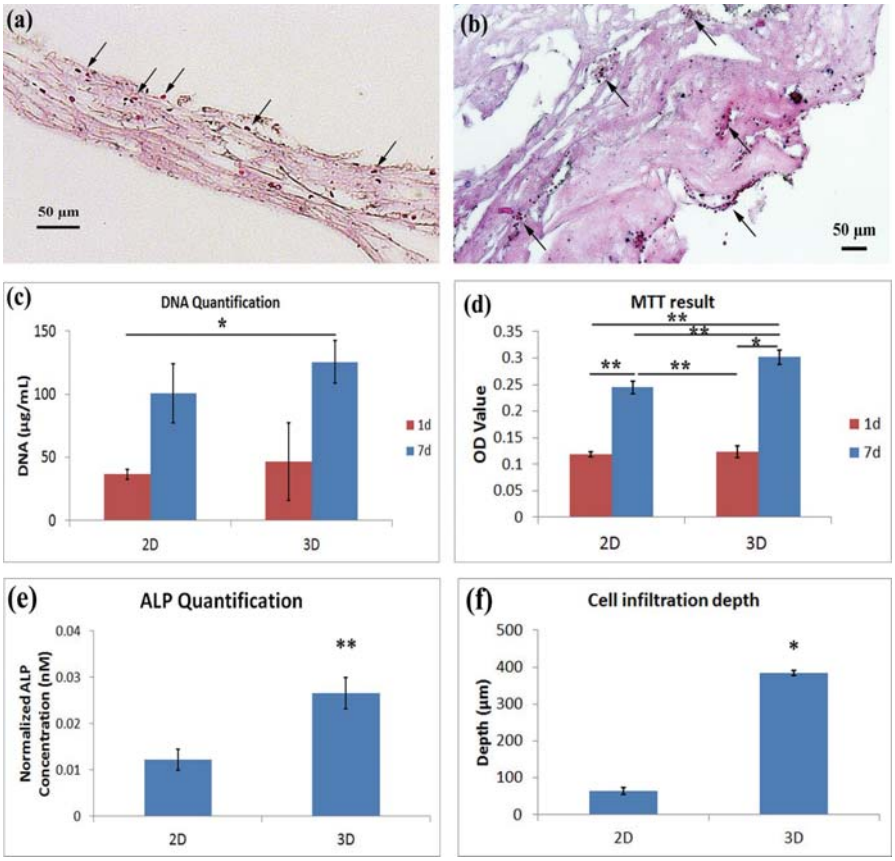

Figure 8 . Hematoxylin-eosin (H&E) staining of 2D (a) and 3D (b) nanofibers with MC3T3 -E1 cultured for 7 days. In the cross section images of nanofiber, cells grown on the superficial layer of the 2D sample; while they infiltrated throughout the whole 3D sample. MC3T3-E1 cells proliferation on the 2D and 3 D PCL scaffold were measured by DNA quantification (c) and MTT method (d). The cell differentiation was tested by ALP quantification (e). (f) Quantification of the depth of the cell infiltration based on H&E images (Wei S. 2017)

In order to precisely repeat each fabrication, we cooperated with Dr. Wen Chen, an assistant professor from the Department of Engineering Technology at Wayne State University, and Mr. Christopher Rea who is an experienced engineer to develop an automatic controllable 3D NF collector. The collector should be able to alter the microstructure of the 3D nanofiber via different moving speeds (0-0.232mm/min). We used polycaprolactone (PCL) in this study to fabricate the nanofiber. PCL is a biocompatible and biodegradable material,

which is approved by Food and Drug Administration in USA for many tissue-engineering applications. We used SEM, micro-CT, and confocal microscopy, etc. to investigate physiochemical characteristics of the NFs formed using this NF collector. We hypothesized that the NFs formed by different speeds should be accurate and reproducible, and the microstructure changes of NFs (porosity, pore size, etc.) should be proportional to the changes of the collector-moving speeds.

Materials and Methods

Polycaprolactone (PCL, Mw = 70,000−90,000), chloroform, and dimethyl-formamide (DMF) were purchased from Sigma-Aldrich (St. Louis, MO).

Description of a concept-proving prototype of the automatic NF collector

The design of the prototype of the NF collector was shown in Figure 9.

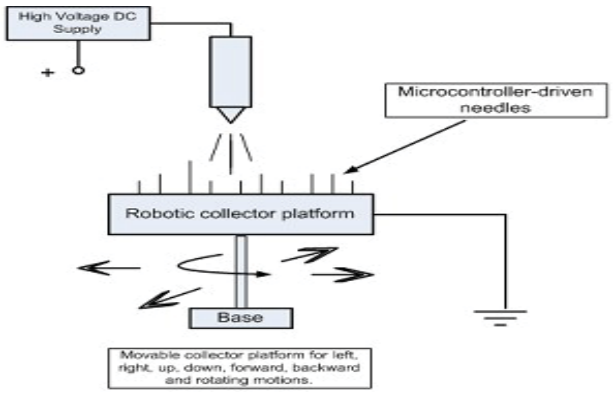

Figure 9. Illustration of a novel 3D NF collector

It consists of (1) a high voltage DC supply, (2) a commercial spinneret, (3) a syringe pump for material supply, and (4) a novel robotic collector device. The robotic collector has a collector platform pierced by many electro-conductive needles. Microcontrollers are used to control stepper motors to drive the collector

platform. The microcontroller is a small computer on a single integrated circuit that includes a processor core, memory, and programmable input/output. Microcontrollers have been widely used in automobile engine control; implantable medical device and other embed control systems because of their small size and acceptable cost. In current applications, it is used to change various settings, such as moving speeds (0, 0.085, 0.158 and 0.232 mm/min) and direction (forward, stand and backward), by programming the assembly language easily. More importantly, it is able to accurately control the stepper motor movement by using a microcontroller named UNO (Arduino). The UNO sends out impulses with microsecond durations, leading to a perfectly controlled performance. In the concept-proving prototype NF collector device, there are four microcontrollers that controls four stepper motors movement independently (Figure 10). They provide forward, stand and backward movements for the platforms. Simultaneously, each of the platforms were programmed a defined moving speed (0, 0.085, 0.158 and 0.232 mm/min respectively). The rationale for the selected range of moving speeds was that the microstructures of NFs formed using these settings were similar to the extracellular environment of cells that had been tested in our previous experiments. Nine needles arranged in a square shape were fixed on each collector for NFs deposition. In Richard Barber Interdisciplinary Summer Research Program, Ameer Hussein Ali Al Shawk and Dr. Xin Wu from Mechanical Engineering Department of Wayne State University designed and produced a new collector platform produces more uniform electrical field and allows more even NFs distribution. It contained seven evenly

grounded needles (0.18mm diameter) arranged in a hexagonal shape (Figure 11). Thus, with the automatic controller system, this prototype NF collector allows an accurate control of the collector platform movement, which might affect the microstructure of NFs deposited on the surface during the electrospinning.

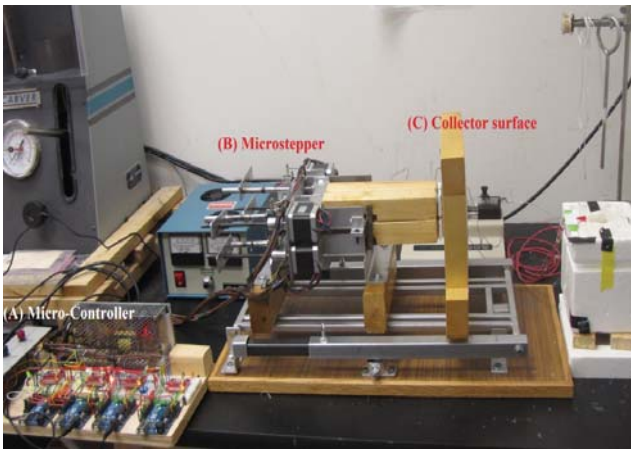

Figure 10 . Prototype of automatic NF collector device. (A) Micro-controller; (B) Microstepper, and (C) collector surface

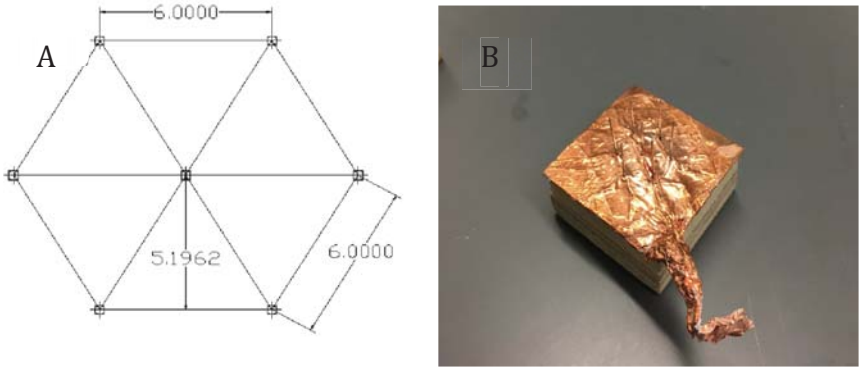

Figure 11. The hexagonal collector with seven electrical conductive needles. (A) Designed and drawn by Ameer Al Shawk (Al-Shawk, A,2019).

Environmental controllable cabinet

The closed cabinet was fabricated by polycarbonate with the dimension of 42'x30'x24'. This cabinet was equipped with a humidifier, a circulation system (a fan), two heaters, a sensor, and an internal control unit. This closed environment cabinet keeps a constant environment at 25°C and 70% humidity during the electrospinning process (Figure 12).

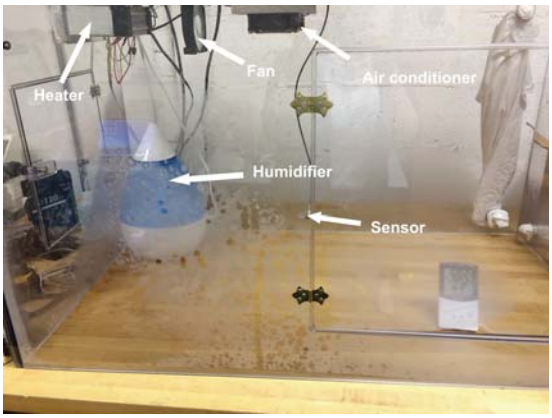

Figure 12. The electrospun cabinet for environmental control

Fabrication of electrospun 3D PCL nanofibers

11% (w/v) PCL was prepared by dissolving PCL into chloroform/dimethylformamide (DMF)(1:1,v/v) overnight to homogenize (Song, Yu et al. 2013). The PCL solution was uploaded to a 5ml syringe (BD Scientific, Franklin Lakes, NJ) and connected to a syringe pump (R100E, Razel Scientific Instruments, St. Albans, VT) with a set flow rate Q. The PCL was ejected through a blunt 26 G needle tip that was connected to a high voltage supply (ES40P, Gamma High Voltage Research Inc., Ormond Beach, FL) with alligator clips. The electrospinning process was performed with the following settings: flow rate (Q) = 1 mL/h, voltage (V)=15 kV, and a needle tip-to-collector plate distance of 10 cm.

The four collector platforms of the automatic collector were constantly moving forward at speed of 0, 0.085, 0.158 and 0.232mm/min, respectively. The PCL NFs deposited on the four needle areas quickly. Six rounds of electrospinning were conducted at 10min/round. At the end of each round, the needles were manually pushed and pierced the formed matrix. The 2D PCL nanofibers were collected on a flat aluminum surface with the aim to compare with the 3D nanofibers.

Scanning electron microscopy (SEM)

The 3D NFs samples were gold-coated (Gold Sputter EFFA Coater, Redding, CA, USA) and the morphology of the NFs was characterized by using scanning electron microscopy (SEM) (JSM-6510LV-LGS, MS, USA) at a 25kV accelerating voltage.

Micro-computerized tomography (μ-CT)

Four types of 3D NFs were scanned with the VivaCT 40 (SCANCO Medical AG, Fabrikweg, Brüttisellen, Switzerland) respectively using a voltage of 45 kVp and a current of 177 μA at10 μm resolution. The morphology of the scaffolds was determined using software from the manufacturer to measure porosity and pore size distribution.

3D confocal laser scanning microscopy (CLSM)

The NFs were scanned and analyzed by a color 3D confocal laser-scanning microscope (Keyence VK-9700, Itasca, IL) (Wei S. 2017). Each measurement forms three types of images: light intensity, color height, and 3D images. The pore volume distribution and surface roughness were measured

using VK-Analyzer software (Keyence). For pore volume measurements (color height image, 400× magnification), about 100 pores at the same height along the z-axis were selected and their volumes measured individually in each scaffold (n = 3). The pore volume distribution was calculated as the percent of a range of pore volumes versus the total pore volume. The surface roughness was represented by the arithmetic mean roughness (Ra), which is automatically calculated using eq 1 according to JIS B 0601-1994 surface texture parameter:

$$R_a = \frac{1}{\ell}\int_0^{\ell} \left| f(x) \right| \, dx \quad (1)$$

Where ı indicates the whole measuring length and x indicates the distance from measuring point-to-point 0.

Atomic force microscopy (AFM)

The nano-scale mechanical properties of PCL NFs were measured by AFM (Bruker). AFM images of the NFs were captured using Contactor Tapping Mode in air (Anagnostakos, Furst et al. 2006). The integrated optical microscope was used to position the cantilever on the top of the NFs within micrometer accuracy. Data was collected by mapping the NFs within a 20×20 μm^2 sized grid. The cantilever tip deflection was used as a feedback signal to maintain a constant force over the scanned area. Young's modulus was automatic calculated by built-in software.

Raman spectrometer

The crystallinity of NFs was measured by Invia Raman Microscope (Reinshaw, uk). Spectra were measured at 10% laser power for three

accumulations of 10s each over the spectral range 200-1500 cm^{-1} with spectral resolution varying from 0.87 to 1.11 cm^{-1}.

Macro-tensile testing

The four types of NFs were cut into 3.8 × 1.3 cm rectangular dumbbell-shaped tensile testing samples with cross sectional width of 0.9 cm for testing region. Sample thickness was measured with an iGAGING caliper (iGAGING, San Clemente, CA). Macro-tensile measurements were performed using an electromechanical universal tester (Instron, Elancourt, France). All samples were mounted between holders at a distance of 1 cm. Tensile testing was conducted at a rate of 0.1 mm/s. A photograph of the experimental setup is shown in Figure 26A.

Statistical analysis

Data was analyzed using SPSS Version 12.0 (SPSS Inc., Chicago, IL, USA). All values were presented as mean ± standard deviation. One-way analysis of variance (one-way ANOVA) was used to analyze the data of each experiment. Statistical significance was $p<0.05$.

Results

The 3D PCL nanofibers were prepared by using the classic electrospinning setting, but collected by the automatic collector (Figure 13) Within 1 hour of fabrication, the thickness of each type of NFs was shown in Table 1 (n=3). The thickness of the NFs increased by the increased movement of the collector. The NF-high has the thickest structure (0.906±0.039mm). Moreover, the thickness of the NFs was increased proportional to the fabrication time. For

NF-high, the thickness of the sample with 15 min fabrication was 0.457 ±0.0388mm (Figure 13A); the thickness was enhanced to 0.906±0.039mm after 1 h fabrication (Figure 13B). The 3D nanofibers have the densest structure in the needle tip area and the loosest structure in between two needles. When we characterized the samples, we chose the central area between two needles, because it has a relatively homogenous structure (Figure 14).

	NF-zero (0 mm/min)	NF-low (0.085mm/min)	NF-mid (0.158mm/min)	NF-high (0.232mm/min)
Thickness (mm)	0.212±0.011	0.498±0.094	0.778±0.103	0.906±0.039

Table 1 the thickness of four types of nanofiber after 1 h fabrication

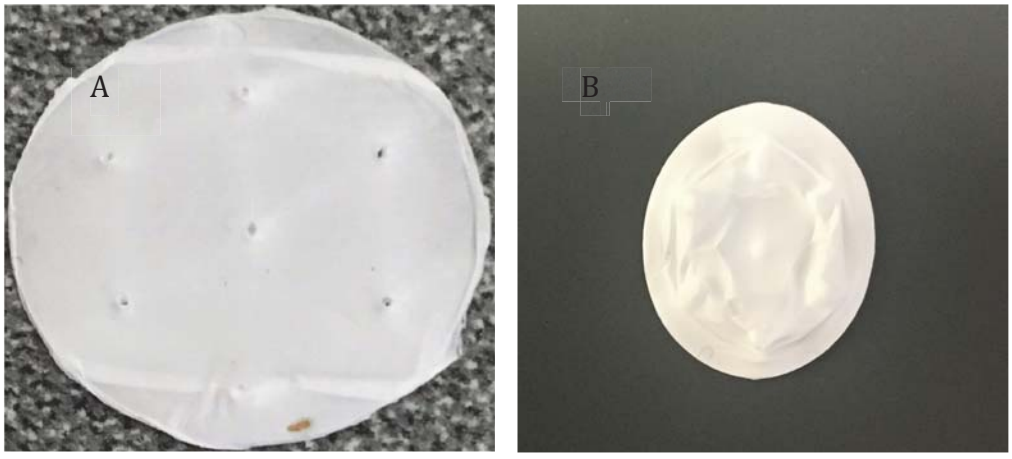

Figure 13 3D PCL nanofiber after 15min (A) and 1 hour (B) fabrication

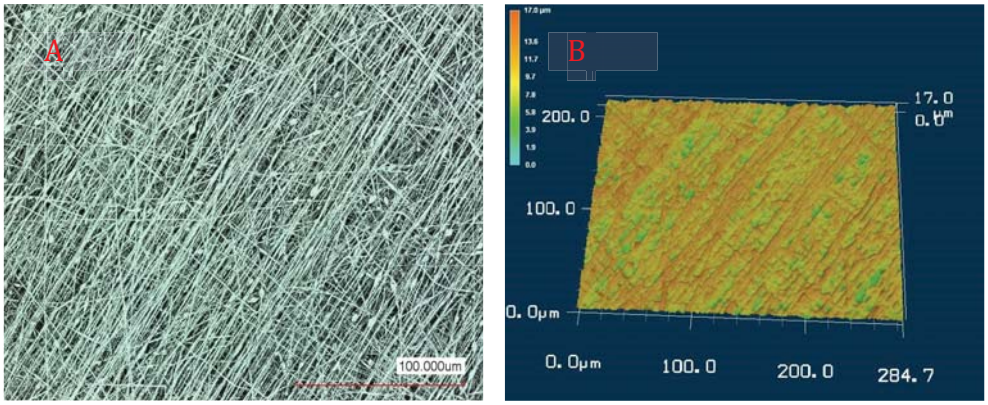

Figure 14 the laser image (A) and height image (B) of the central area of the NF-low captured by the CLSM. The magnification was 3000X.. (Al-Shawk A,2019)

The microstructure characterization of 3D PCL NFs--Scanning electron microscopy (SEM)

As shown in Figure 15, the density of the NF matrices was influenced by the moving-speed of the collectors. The NF-zero exhibited the densest microstructure; with increasing the moving speed from 0.085 to 0.232mm/min, the NF matrices became fluffier (5000X).

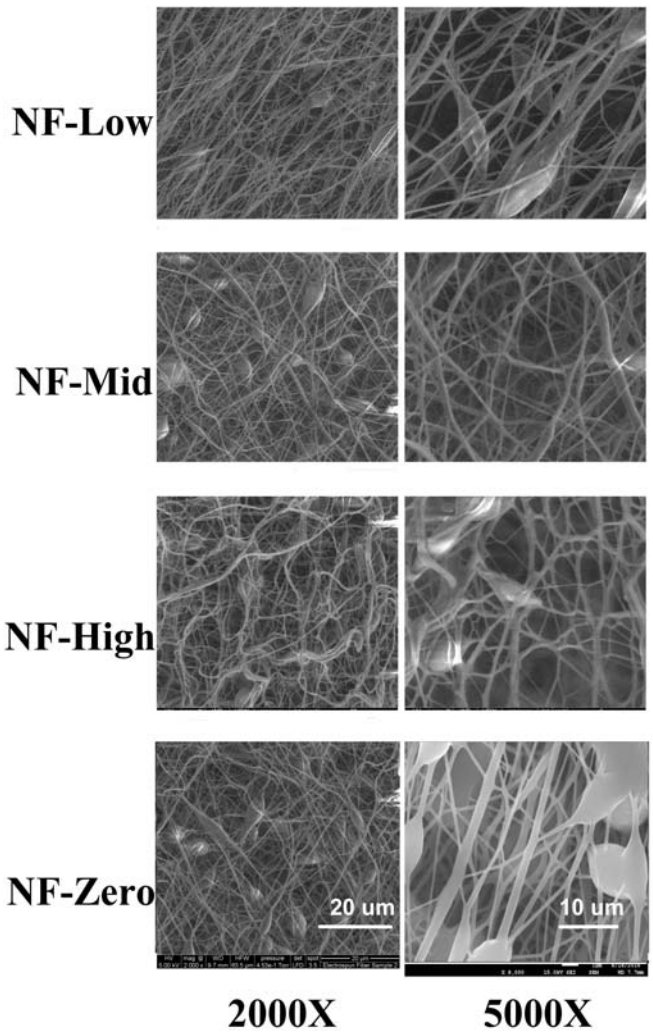

Figure 15. The SEM images of four types of NFs with 2000X and 5000X magnifications

The microstructure characterization of 3D PCL NFs--Micro-computerized tomography (μ-CT)

The entire area of the NFs were scanned using μ-CT aimed with the aim to understand the porosity and pore size (μm^2) of the whole matrix (Rampichová M 2013, Wei S. 2017). Figure 16 revealed that the majority of the pore sizes of the four types of NFs distributed in the range of 50-100 μm^2; however, the percentage of pores was gradually reduced with increased moving speeds.

Notably, in the larger pore size range (>100μm^2), the amount of pores in the NFhigh was dominant. The percentage of pores in NF-high was 34.4% in >100 μm^2, which was higher than NF-mid and -low (18.9%), and NF-zero (3.5%). Similarly, NF-high had the largest porosity, 93%; and the porosity dropped when the moving speeds decreased (Figure 17).

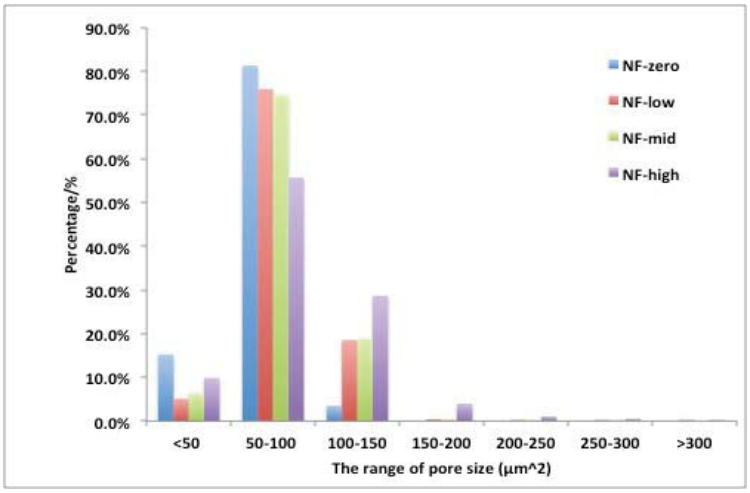

Figure 16. The pore size distribution of four types of nanofibers. Approximately, 100 pores were measured for each sample by μ-CT.

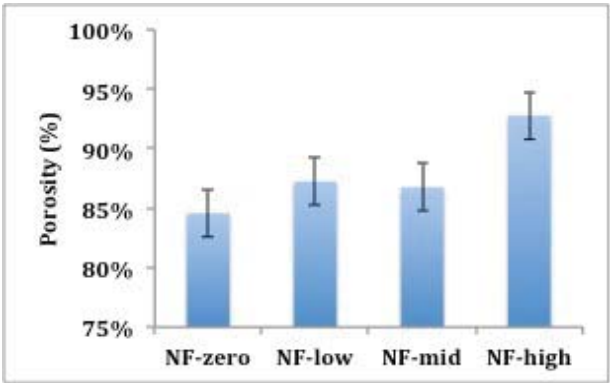

Figure 17. The porosity of four types of NFs calculated by μ-CT (n=3).

The microstructure characterization of 3D PCL NFs--3D confocal laser scanning microscopy (CLSM)

The confocal laser scanning microscopy was used to investigate the 3D morphology, pore volume and surface roughness of the NFs. Three types of images were captured by CLSM, and they were laser image, height image and 3D images (Figure 18). The color in the height and 3D images represented the location of fibers along the z direction. Thus, the character at the z direction could be obtained. The SEM results were further confirmed by CLSM. The NFs became less dense when the collector movement increased (Figure 18) (Al-Shawk A. et al, 2015). The NFs were prepared by nine needles array collector.

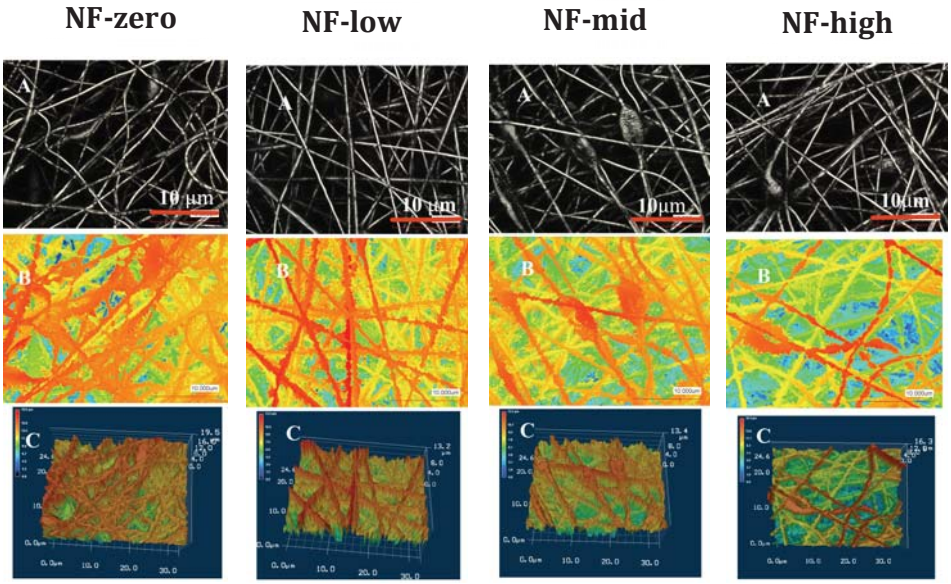

Figure 18. The laser image (A), height images (B) and 3D images (C) of four types of NFs (15,000X). In the height and 3D images, the same color represented the NFs located at the same height along z direction. (Al-Shawk A. et al, 2015)

Based on the height images (400X), the pores located at the same level of the z-axial were picked, and the volume of picked pores was measured by built-in

software. The pore volume distribution was presented in Figure 19. Generally, the pore volume was increased following an increase of moving speed. More than 60% of pores in NF-zero had the volume less than 10,000 μm^3, whereas only 0.1% of pores in NF-high had the volume distributed in this range, and the percentages of pores in NF-low and –mid were 18.1% and 4.3%. In order to better understand the pore volume distribution, we combined some ranges of the pore volume and the data was shown in Figure 20. We found the gradual increase of the larger pore volume range (>60,000 μm^3) with the increase of moving speed provides a favorable microenvironment because larger pores are expected to better support the cell infiltration and growth. In this range, NF-high had the highest percentage, 51.7%, and the percentage of NF-mid, NF-low and NF-zero was 37.7%, 21.7% and 12.4% respectively.

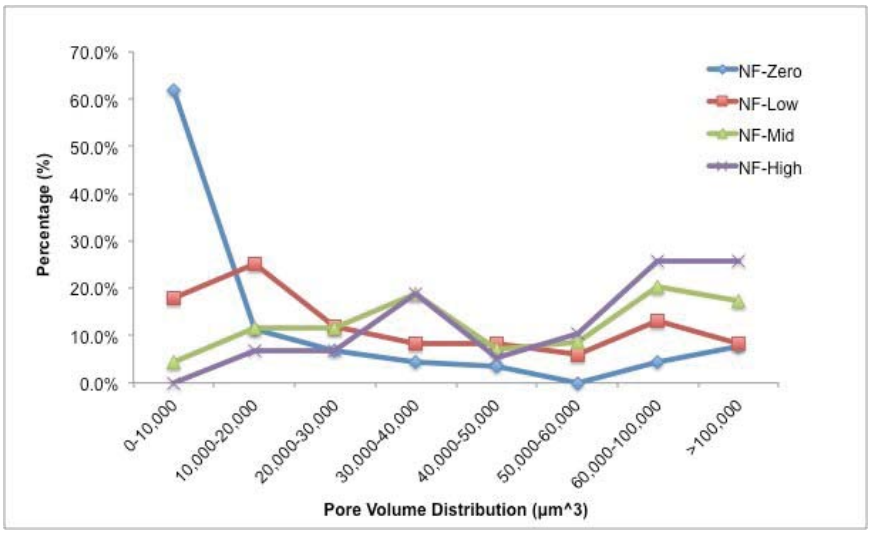

Figure 19. Pore volume distribution of NF-zero, NF-low, NF-mid and NF-high (n=3, 100 pores picked from each sample). 3D scanning data was measured by Ameer Al-Shawk.

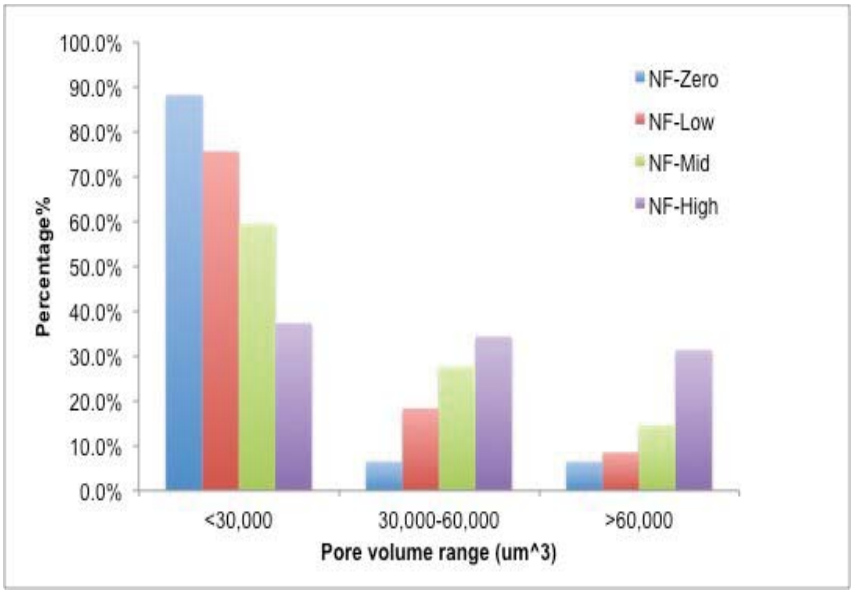

Figure 20. The percentages of four types of NFs in the range of pore volume <30,000, 30,000-60,000 and >60,000 μm^3

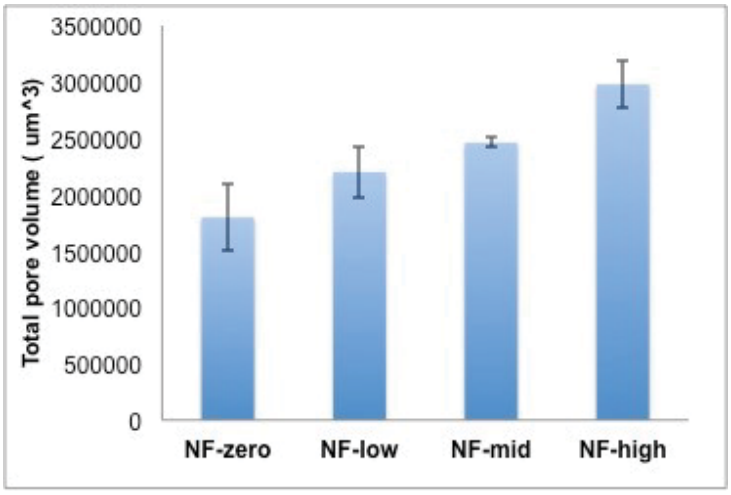

Figure 21. The total pore volume of the four types of NFs measured by CLSM at 400X magnification. (n=3, $p<0.05$). 3D scanning data was measured by Ameer Al-Shawk.

The total pore volume of scanned NFs was measured by CLSM with 400X magnification at the same time. The NF-high had the highest total pore volume (Figure 21). The surface roughness was gradually increased by the increase of

moving speeds (Figure 22). The surface roughness of the NF-high was significantly higher than the NF-zero and NF-low ($p<0.05$) (Figure22).

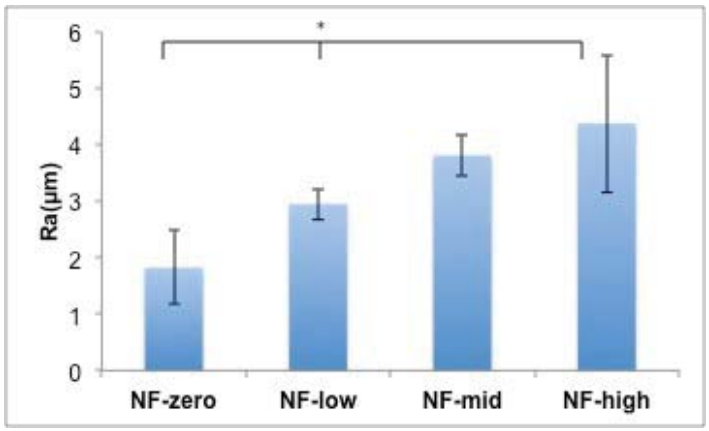

Figure 22. The surface roughness of NFs (Ra, μm) measured by CLSM. 3D scanning data was measured by Ameer Al-Shawk.

Mechanism properties of the 3D NFs –nanoscale mechanism properties (AFM)

The Young's modulus of a single nanofiber was measured and calculated by contactor tapping mode of the AFM. Figure 23B exhibited the nanofibers collected by the moving collector had a higher stiffness than the one formed on the non-moving collector, in which the Young's modulus of NF-mid and NF-high were significantly higher than the NF-zero.

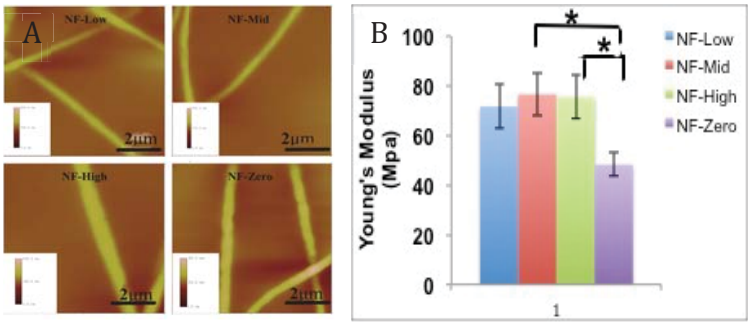

Figure 23. Nano-scale mechanical properties tested by AFM. (A) Contact tapping mode images; (B) Young's modulus (E) of single fiber (n=100)

Mechanism properties of the 3D NFs –macro-scale mechanism properties

In Figure 24, all samples' maximum stress was between 0.2-0.3 MPa. It was lower than the 2D PCL NFs, which was about 0.85 MPa according to our previous work (Wei S. 2017), because 3D samples have a much looser structure.

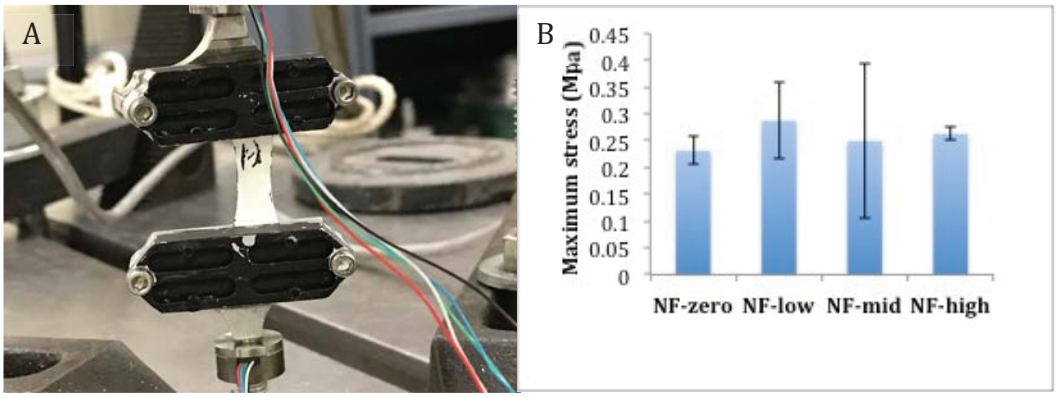

Figure 24. Macro-tensile tests of four types of PCL NFs, experiment set-up (A), and maximum stress (B)

Mechanism properties of the 3D NFs –crystallinity (Raman spectroscopy)

We obtained Raman spectra of 3D NFs, which are sensitive to the degree of crystallinity (Figure 25). The increased crystallinity of NF-high, NF-mid and NF-low fibers relative to NF-zero were confirmed by enhanced peak intensities of the main PCL bands reflecting crystalline domains: 1100 cm^{-1} (skeletal stretching)

and 1443 cm^{-1} (δ CH_2) (G.Kister 2000, PaolaTaddei 2005). In addition, the presence of the board band at 868cm^{-1}, and the absence of 1107 cm^{-1} narrow peak were also associated to the character of the amorphous part of the PCL (G.Kister 2000).

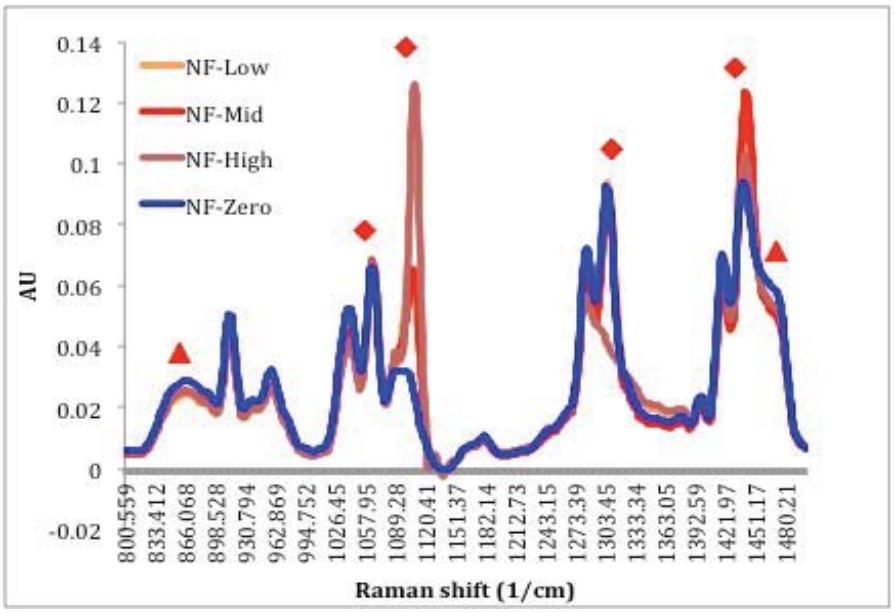

Figure 25. Raman spectra of four types of NFs to represent the crystallinity of NFs. Red triangle means amorphous wavenumber of PCL; Red diamond shape means crystal wavenumber of PCL

Discussion

In this study， I described a simple and one-step method to fabricate 3D nanofiber matrices with desired porous structure by designing a moving electrospinning collector mounted with a panel of hexogen needles array. Moreover, the collector was allowed to move forward at constant speed via an electronic control system. Interestingly, the collector movement altered the physiochemical properties of the NFs. Results of SEM, CLSM, and micro-CT demonstrated that the porosity and pore size/volume were proportional to the

moving speeds. Faster movement produced thicker matrixes, which also proved that less dense structure is formed by faster movement. The collector movement also changed the mechanical properties via elevating crystallinity of fibers. With this novel fabrication, not only it did produce 3D matrixes, but it also controlled physiochemical properties of the matrices.

There are many other methods to produce 3D nanofibers. Ekaputra et al. developed PCL NFs employing sacrificial co-fiber (poly ethylene oxide (PEO)), which would be leached out eventually. This PCL NFs further combined with Heprasil, a hyaluronic acid-derivative hydrogel to form a 3D matrix. They found that the 3D matrix especially enhanced human fetal osteoblasts infiltration and assisted cell attachment and proliferation (Baker BM 2008). Pham et al. used stacking multilayers of PCL microfibers and PCL nanofibers to build a 3D scaffold and to increase the pore sizes (Pham, Sharma et al. 2006). Results showed the microfiber layer significantly increased the pore size to 20-45 μm, which was beneficial to cell infiltration; and the nanofiber layer enhanced cell spreading after 24h culture (Pham, Sharma et al. 2006). Rampichova et al. modified the texture of the collector surface and received PCL meshes with knitted structure, which consisted of a less dense and a thick area. The thick area supported enough mechanical strength, and the loose area was beneficial to bone marrow derived mesenchymal stem cells (MSCs) penetration and proliferation (Rampichová M 2013). Other methods like yarn (Smit 2005), ice crystals (Teo 2011), and photopaterning (Goodman, Yao et al. 2013) are able to fabricate NFs with a 3D structure. Compared to these methods, the advantage of our method is its one-

step and high efficiency fabrication, which allows us to simply control the thickness, microstructure, and chemical and mechanical properties of the NFs via collector movement. It would not be necessary to remove the pore-forming agent like the leach-out method; or to stack meshes together like the layer-by-layer method. It is real-time and just a one-step production. In addition, the quality and microstructure of formed NFs are guaranteed and reproducible. Firstly, we used a closed electrospun cabinet to keep the electrospinning process in an environment with a constant humidity and temperature. Secondly, the collector movement is precisely controlled. Thirdly, the needle array in the hexogen shape kept the same electrical charge at each needle tip (Al-Shawk A, 2019). With this technology we could make various types of NFs with different structures based on the requirement of the application. The composite NFs seem to be very promising for tissue engineering applications.

Several techniques had been applied to characterize the microstructure of our samples. As we know each technology has merits and limits, and we tried to combine their advantages and characterized the NFs from different aspects. It was necessary to point out that our sample was not homogenous (needle area—dense structure), and we only characterized the NFs located at the center area between two needles, because this area has a relatively loose and homogenous structure, which should be suitable for cell growth. In comparison, the SEM images visually (Figure 15) revealed the NF-high and –mid had a relatively looser structure with a larger space between the nanofibers than the NF-low and NF-zero. Micro-CT scanning further proved the SEM results. The NF-high had the

highest porosity (92.8%) that was higher than NF-mid (87%), NF-low (86.8%) and NF-zero (85%). We demonstrated that the porosity was increased by the increase of the moving speed. Followed by elevating moving speed, the pore size was also increased. The pore size distribution of NF-zero, -low, -mid and high was 0-100, 0-250, 0-250 and 0-300μm^2. Notably, a very little portion of pore in NF-high had >300μm^2 diameter. This pore size of NFs has not been reported. Large pore size is critical to cell infiltration and tissue regeneration, especially for blood vessel ingrowth, for example, in bone repair, vascularization happens at highly porous area with pore size over 350 μm (Karageorgiou V 2005). The main advantages of the micro-CT include that it is a non-destructive method and enable to scan and analyze the entire sample (Ho ST 2006, Marelli B 2010, A. Cipitria 2011). However, the relatively low resolution (10 μm) limits its application on nano-scale materials characterization. The second quantification method we used was CLSM. Compare to the SEM and micro-CT, it's able to obtain the 3D characters of the samples and has high resolution (1nm). Similarly, the NF-high had the largest total pore volume, and it was significantly higher than the NF-low and –zero. According to the magnification, the measured sample size was about 147*147*147 μm. Thus, after covering to the porosity, the NF-zero was 60.7%; NF-low was 70.8%; the NF-mid was 76.8%; and the NF-high was 93.01%. It showed the same tendency of the porosity measured by micro-CT. Most of published literature reported the porosity of PCL NFs was between 60% to 80% (A. Cipitria 2011). The higher porosity like NF-high may benefit to cell growth, while it may impair mechanical strength at the same time. The pore volume

results showed about 80% and 55% of pores in NF-zero and -low had volume less than 30,000 μm^3 respectively, whereas, the most of pores' volume in NF-high were larger than 60,000 μm^3. Notably, 25.9% pores of NF-high had volume over 100,000 μm^3, which should be large enough for cell infiltration. In this range, the percentage of pores decreased followed by slower movement. Taken together, our results proved that faster collector movement could build less dense nanofiber matrices via enlarging the porosity and pore size/ volume. In comparison, during the same time, the moving distance of the needle tip (collector) with faster movement was longer than the slower moved collector. These larger distances elongate the nanofibers and increase the space between each fiber, which results in a looser structure. This mechanism also explained the results of surface roughness. The NF-high should have higher peaks along the z-axis than others, corresponding to a rough surface.

The mechanical properties of scaffold are essential for bone tissue engineering, because they should withstand the forces exerted by physiological activity and by tissue growth. The nano-scaled mechanical properties of the materials relate to the interaction between the materials and cells; the macroscaled mechanical properties used to describe the ability of the scaffold to bear loading. Results of AFM showed higher Young's modulus of the single nanofiber formed at the moving collector than that of NFs formed without movement (NF-zero). The crystallinity of nanofiber relates to its mechanical properties (Shing-Chung Wong 2008, A. Cipitria 2011). Higher crystallinity enhances the stiffness of fiber (Shing-Chung Wong 2008). During the

electrospinning, rapid removing solvent is expected to result in little opportunity for crystal nucleation. The process of crystallization finally completed in the whipping region of the jet through orientation of the polymer chain (C.T. Lim 2008, A. Cipitria 2011). The NFs formed by the moving collector were found to have higher crystallinity as well, which explained the results of AFM. The movement of collector created a pulling force, which results in the nanofibers of NF-low, mid and high was stretched during electrospinning. Crystallization would be orientated and enhanced by the stretch (Shing-Chung Wong 2008). Results of macro-tensile test showed the maximum stress of four samples was between 0.2-0.3MPa, and there was no significant difference among the samples. Commonly, the looser structure of NFs may impair the tensile strength, because fewer fibers entangled. While the maximum stress of the NF-high was not much lower than others. We thought its higher crystallinity might help to enhance the tensile strength. Overall, the tensile strength of the NFs was lower than sponge bone as reported within 0.92-5.38 MPa (Røhl L 1991). Thus, further study on the biomineralization of the 3D NFs is necessary.

Conclusion

A novel 3D NF fabrication technology has been developed based on coronal charge effect. The automatic 3D NF collector and the environment control cabinet further precisely control the process of electrospinning. The technique ensures the accuracy and reproducibility of NFs. Moreover, we can control the thickness, physiochemical and mechanical properties of the 3D NFs by simply through changing the collector movement, and discover the pore size

and porosity of the NFs are proportional to the moving speed. Interestingly, the collector movement also increased the crystallinity, which enhanced the stiffness of the fiber. We are continuing develop and update a second-generation collector. It should be more convenient to operate. Users are allowed to set different moving speeds, moving directions and patterns via a control board or a mobile application. In order to comprehensive describe the NFs; we still need to character the dense area (around needle tip) of the NFs.

The nanofiber is one of the promising materials to mimic the nano-fibrous structure of the ECM. A porous and 3D structure scaffold is predominantly required in tissue engineering. Our composited 3D NFs with a controllable microstructure could mimic different ECMs and be applied to the various areas of tissue engineering. As a bone implant coating material, in the next chapter we would investigate its biological properties by in vitro cell culture and defined the optimal NF microstructure that can be used for cell adhesion, proliferation and differentiation.

CHAPTER 3 THE BIOLOGICAL PROPERTIES OF BONE CELLS CULTURED ON THE 3D NANOFIBERS

Introduction

Tissue engineering develops different biocompatible scaffolds with the aim to mimic the ECM of native tissues and assist tissue regeneration. The microstructure of a scaffold, such as pore sizes, porosity and interconnectivity plays essential role in guiding cell ingrowth (Chen L 2016). Many types of cells are involved in bone healing including macrophages, fibroblasts, osteoblasts, mesenchymal stem cells (MSCs) and vascular endothelial cells. These cells have different requirements of the favorable extracellular environment for their growth and differentiation. For example, osteogenesis occurs at a highly porous area with large pore sizes (>350μm) in vivo (Karageorgiou and Kaplan 2005); whereas fibroblasts have been demonstrated to prefer an area with the pore sizes of 6-20 μm (Lowery, Datta et al. 2010). In a separate study, we developed a calcium polyphosphate scaffold with gradient pore sizes (Chen L 2016). We found that MC3T3-E1 (pre-osteoblasts) had much higher growth rate and differentiation level in the zone with the larger pore sizes (>250 μm) than the zones with smaller pore sizes (<250 μm) (Chen L 2016). In this continuing study, we will determine the most favorable extracellular microenvironment for the growth and differentiation of different bone cells. More specifically, we investigated the cellular behaviors of the different types of cells when they grown on the 3D NF matrices with different and well-defined microstructures. This study is important and essential because a better understanding of the various cell responses grown on the 3D NFs in vitro is critical for the further application of the 3D NFs as

a new implant surface coating to enhance implant stability by enhancing new bone formation.

We have chosen three cell lines for this study. (1) Murine pre-osteoblast MC3T3 cells (bone forming cells), murine pre-osteoclast RAW 264.7 cell (bone dissolving cells) and rat adipose tissue-derived stem cells (ASC). We had established MC3T3-E1 and RAW cell line models (Song, Yu et al. 2013, Chen L 2016), and believed cells should be very sensitive to their living environments. Since we discovered the different properties of the four types of 3D NFs in Chapter 2, we could investigate how the cells chose their preferential environments. We cultured the three types of cells on the four types of PCL NFs NF-zero, NF-low, NF-mid and NF-high, respectively. The cell behaviors of adhesion, proliferation, distribution and differentiation were investigated. An optimized 3D NF would be defined as a coating material for a further drug loading investigation (Chapter 4) with an aim to enhance osseointegration. We hypothesized that a favorable cellular response should be expected when cells were cultured on the 3D PCL NFs with less density and large pore sizes. We proposed that cells were very sensitive to the changes of the NF microstructures (pore sizes, pore shapes, porosities and topologies) and that the requirements of NF microstructures should be different among different cell lines.

Materials and Methods

Alpha-modified Minimum Essential Medium, trypsin, fetal bovine serum, penn/strep, Dulbecco's phosphate-buffered saline (DPBS buffer), and DiI celllabel solution were purchased from Invitrogen (Grand Island, NY).

Collagenase II and CelLytic MT cell lysis reagent were purchased from Sigma-Aldrich (St. Louis, MO). Murine MC3T3-E1 pre-osteoblast cell line and murine pre-osteoclast RAW 264.7 cells culture was purchased from American Type Culture Collection (ATCC, Manassas, VA). Quant-iT Pico- Green dsDNA Assay Kit was purchased from Thermo Fisher Scientific (Waltham, MA). Alkaline Phosphatase Activity Colorimetric Assay Kit was purchased from BioVision (Milpitas, CA).

Cell culture

Murine pre-osteoblast MC3T3 cells culture: MC3T3 cells (ATCC) were cultured in complete α-modified minimum essential medium (α-MEM) medium including α-MEM, 10% fetal bovine serum and 1% penn/strep at 37°C with 5% CO_2.

Murine pre-osteoclast RAW 264.7 cells culture: RAW cells (ATCC) were cultured in DMEM medium containing 10% fetal bovine serum and 1% penn/strep at 37°C with 5% CO_2.

Rat adipose tissue-derived stem cells (ASCs) isolation and culture: ASCs were isolated from the belly adipose tissue of adult female Sprague-Dawley rats following Dr. Main Lam's instruction, and the technique was also described elsewhere (Veronesi F 2014). Briefly, adipose tissues were washed by serial solutions of Betadyne followed by PBS, and then chopped into small tubes and digested by 150ug/ml collagenase II in agitation for 1 h at 37°C. The enzymatic reaction was stopped by the addition of DMEM (high glucose) with 10% FBS

added. The nucleated cells were plated into 75-cm^2 tissue culture flasks and cultured in complete DMEM medium for expansion.

NFs preparation and sterilization

The NF-zero, -low, -mid and –high was produced by method introduced in chapter 2. Each sample (size: 1x1 cm) was sterilized by UV light for 4h (2h for each side). The sterilized samples were placed in 40mm petri dish pre-filled with cell culture medium overnight prior to cell seeding.

Cellular proliferation

The MC3T3 cell, RAW and ASCs suspension with cell density of $8X10^5$ cells/ml were respectively and manually pipetted on the top of each NF sample (four types of samples) with 10μl per droplet. Each scaffold was loaded with 100μl cell suspension. The cellular proliferation was measured by DNA quantification through Qaunt-iT Pico-green DNA kit after 3 days and 7 days culture. Briefly, the cells grown on the NFs were lysed by mixing with 200 μl CelLytic MT cell lysis reagent overnight at 4 °C. 50 μl cell lysate was mixed with 50 μl PicoGrenn dsDNA reagent and then added into 96 well plates. The fluorescence values were measured by microplate reader at 528 nm after excitation with 485 nm light. The DNA concentration was converted from an OD value on the basis of standard curve.

Cellular distribution

To better understand the cell interaction with the NFs, the NFs and cells were labeled by fluorescent dyes and observed under confocal laser scanning microscopy. 5ml PCL solution was labeled by adding 20 μl green fluoresce

Calcein, and then the fluorescent labeled PCL solution was used to prepare 3D PCL NFs. Three types of cells were cultured on these NFs respectively. After 3 days culture, the NFs was firstly washed by PBS three times. The cells were labeled by Dil cell-labeling solution at 37 °C for 15 min. Dil is a lipophilic membrane stain, which can stain the entire cell. The NFs were then washed by PBS three times and soaked in PBS for observation. The fluorescent images were obtained by Leico TCS SP II confocal laser-scanning microscopy (Buffalo Grove, IL) under 10X objective. 3D reconstruction was performed used Volovity (PerkinElmer, Waltham, MA) via stacking images along z direction to reveal the cell migration.

Cellular differentiation

Murine pre-osteoblast MC3T3 cells differentiation: After cell seeding, MC3T3 cells were cultured in osteogenic media containing 10 mM β-glycerophosphate and 50 μg/ml L-ascorbic acids for 14 days. The cell differentiation levels were measured by alkaline phosphatase (ALP) assay (Song, Markel et al. 2012). Briefly, the cells were lysed overnight. The ALP activity in the cell lysates was measured utilizing the conversion of a colorless p-nitrophenyl phosphate to a colored p-nitrophenil. Microplate reader was used to measure the color changes at 405nm. The AKP activity levels were normalized and converted from optical density (OD) value to protein concentration based on the standard curve.

Murine pre-osteoclast RAW 264.7 cells differentiation: The RAW cells were cultured in the presence of receptor activator of nuclear factor kappa B

ligand (RANKL, 30 ng/ml) for 14 days. The formation of osteoclast and osteoclast-like cells were evaluated using the Tartrate-Resistant Acid Phosphatase (TRAP) assay, and the presence of $TRAP^+$ cells were represented as the percentage of total cells, as we described elsewhere (Ren, Li et al. 2004).

Data analysis

All the variables were summarized and expressed as mean ± SD. The statistical significance of results was determined by ANOVA for differences among multiple groups. $p<0.05$ was considered the statistically significance.

Results

Cell proliferation

The number of cells cultured on NFs was measured by a PicoGreen assay. For MC3T3 cells, the cell number on NF-zero, NF-low, NF-mid and NF-high was slightly increased on day 3 (Figure 26). On day 7 the highest cell amount was found on NF-high; and the lowest cell amount was found on NF-zero and that number was significantly lower than other groups ($p<0.05$) (Figure 26). The cell number on NF-low, -mid and –high rapidly increased 10 to 15 folds between 3 and 7 days, and the increase was significant ($p<0.05$) (Figure 26).

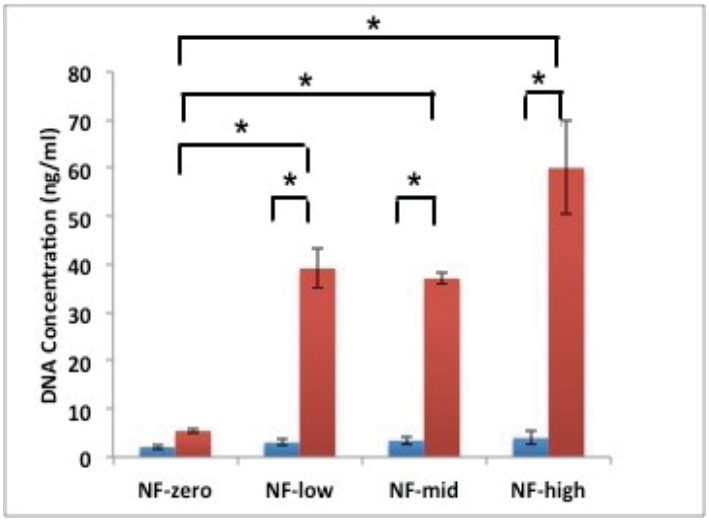

Figure 26. MC3T3-E1 cells proliferation on NF-zero,-low,-mid, and -high for 3 and 7days culture, analyzed via DNA quantification ($p<0.05$).

For RAW cell, on third day the cell number slightly decreased followed by the increase of moving speeds, and the highest cell amount was found on NF-zero (Figure 27). On day 7 the cell number on NF-mid was the highest (Figure 27). The cell number of ASC was gradually increased from NF-zero to NF-high, in which the NF-high had the highest cell amount (Figure 28). The amount of cell on the NF-zero was significantly lower than other groups ($p<0.05$).

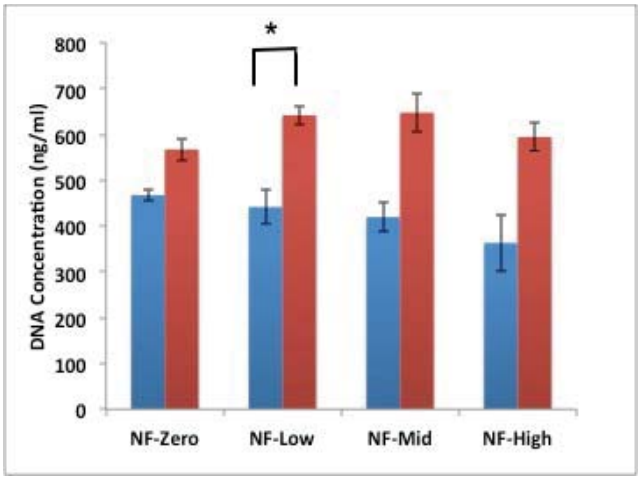

Figure 27. RAW cells proliferation on NF-zero,-low,-mid, and -high for 3 and 7days culture, analyzed via DNA quantification ($p<0.05$)

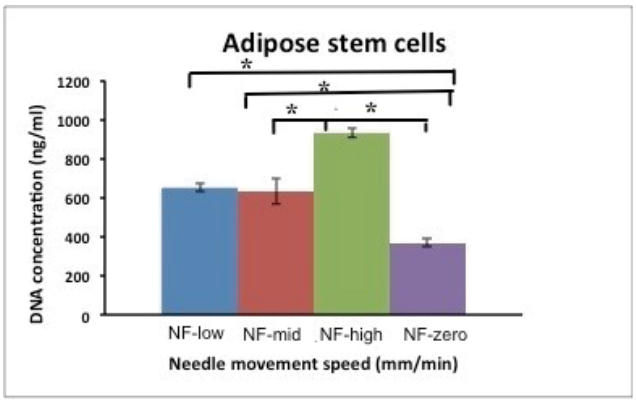

Figure 28. ASC cell proliferation NF-zero,-low,-mid, and-high for 3 culture, analyzed via DNA quantification, $p<0.05$.

Cell distribution

Three days after cell seeding, the NFs were stained by a green fluorescein Calcein and the cells were labeled by a red fluorescein DiI. The confocal laser-scanning microscopy was used to visualize the cell locations inside of the NFs. As shown in Figure 29, all three types of cells were trapped in the superficial layer of the NF-zero at the z-direction; In contrast, the RAW cells on the NF-high

migrated much deeper with a depth of 621.8 μm. The migration of ASC and MC3T3 was not as obvious as the RAW cells did; however the distinctly more amount of cells were observed on NF-high than on the NF-zero.

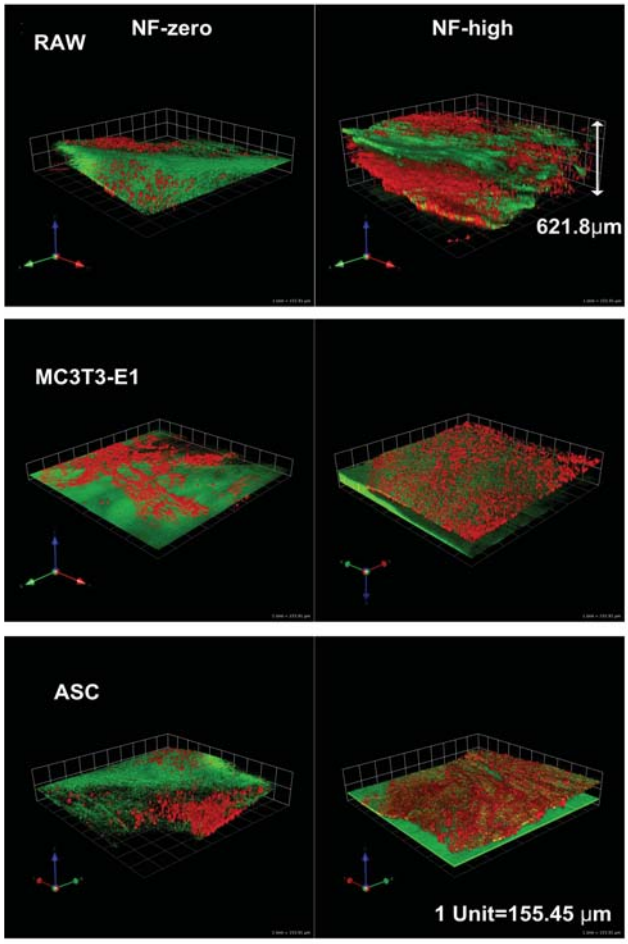

Figure 29. RAW cells, MC3T3-E1 and ASC cells distribution on NF-zero (left) and NF-high (right) 3 days after seeding. Confocal microscopy z-stack images (10X) showed cell migration (red) on two types of NFs (green color).

Cell differentiation

The differentiation level of the MC3T3 was represented by the expression level of AKP, an osteoblasts marker. The AKP concentration was normalized by

total protein concentration. Results indicated that the NF-high had highest expression level of AKP, and it was significantly higher than the expression level on the NF-mid and NF-zero (Figure 30).

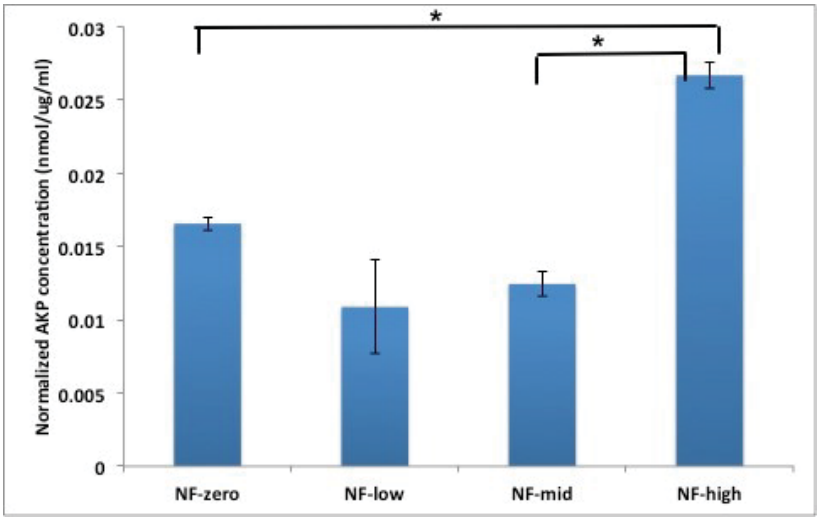

Figure 30. MC3T3-E1cell differentiations on NF-zero,-low,-mid, and -high measured by AKP assay, $p<0.05$.

The RAW cells were cultured in the presence of the receptor activator of nuclear factor kappa B ligand (RANKL, 30ng/ml) for 14 days. The formation of osteoclasts and osteoclast-like cells was evaluated using the Tartrate Resistant Acid Phosphatase (TRAP) Assay. Cells on the NFs-high showed highest differentiated level (Figure 31).

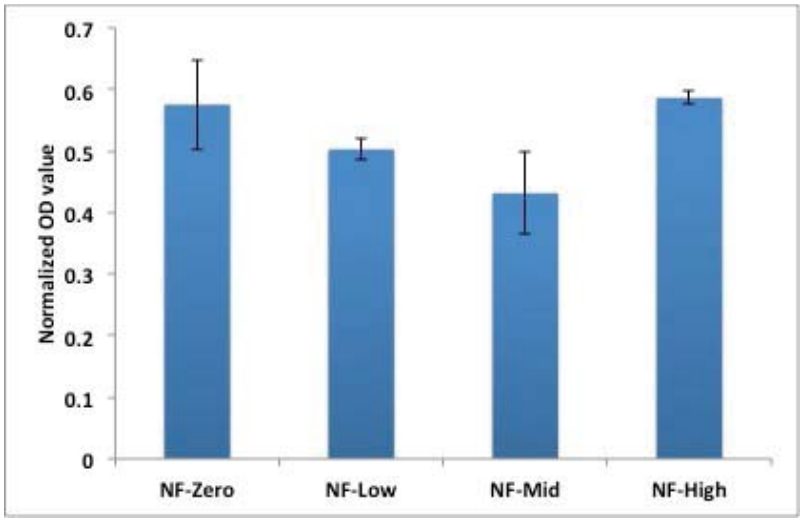

Figure 31. RAW cell differentiations on NF-zero,-low,-mid, and -high analyzed by TRAP assay, $p<0.05$.

Discussions

Bone cell microenvironment is composed of factors directly surrounding the cells. These factors including biochemical signals, geometry, microstructures and mechanical stimuli decide the fate of cells. It have been reported that a minor modification of the sintering temperature of a CaP ceramic has a consequence on its microstructure (Barthes J 2014), crystal sizes (Glawe JD 2005), and mechanical strength (Glawe JD 2005). The changes of these parameters in turn enhanced the osteoconductive properties of the scaffold and expressed by elevating the cell expressions of alkaline phosphatases and osteocalcins (Crouch AS 2009). Thus, the extracellular microenvironment is essential, and it should be the ideal model for the design of a bone substitute.

The microstructure of a bone scaffold including pore sizes, porosity, interconnectivity, and surface areas plays an important role on the effect to the cell behavior. Generally, the high portion of well-connected macro-pores can allow sufficient culture medium with enough nutrients and oxygen to pass

throughout of the scaffold (Barthes J 2014); whereas the micro-pores areas of the scaffold have high mechanical strength and slow degradation rate (Barthes J 2014). We produced the four types of NFs with different microstructures that have significant impacts on the cell growth. The cellular proliferation results of the MC3T3 and ASC indicated that the both cell lines grown faster on the NF-high, and the cell number on the NF-high was significantly higher than the number on the NF-zero (7 day culture, $p<0.05$). According to the data of chapter 2, we understood that the NF-high had the highest porosity (93%), and about 85% pores of the NFs were larger than 30,000 μm^3. Probably due to its looser structure, it allowed sufficient nutrients and oxygen to transport to the cells. The cell amount gradually decreased when cultured on a denser structure (NF-low and NF-zero) because less nutrients and oxygen were available at this area. These results are in the good agreement with our previous work regarding to the comparison of cell growth between 3D NFs and 2D NFs (Wei S. 2017). The 3D NFs had the pore sizes mainly distributed in the 0.1-10 μm^2, while the primarily pores of the 2D NFs were much smaller (<0.1 μm^2). The infiltration and proliferation of the MT3T3 cells were increased due to the loose pore structure of the 3D NFs (Wei S. 2017). Badami AS et al. and Schofer MD et al. reported that an ideal electrospun NFs should have nano-scale fibers with macro-scale pores between 10 to 500 μm, and this porous structure permitted the growth of human mesenchymal stem cells (hMSCs) and their differentiation to osteoblasts (Badami AS 2006, Schofer MD 2008, Blakeney BA 2011). Other research groups like M. Rampichova et al. concluded their 3D PCL NFs with larger pore size

areas (average 10 μm^2) than 2D NFs (5 μm^2) significantly increased mesenchymal stem cells migration and proliferation (Rampichová M 2013). For RAW cells, we surprised found the looser structure of the NFs didn't obviously help its proliferation. The cell number on the NF-low and –mid even slightly higher than the number on the NF-high (7 day culture). The reason for this might due to the smaller size of the RAW, it made cells difficult to bridge the large pores in the NF-high and that impacted cell growth rate (Holtorf, Datta et al. 2005, Gomes, Holtorf et al. 2006, Mygind, Stiehler et al. 2007, Thorvaldsson, Stenhamre et al. 2008).

The less dense structure of the NFs assisted cell infiltration and differentiation as well. The confocal laser-scan image of RAW cells showed the cells were able to penetrate much deeper on the NF-high (621.8 μm), while they only spread on the superficial layer of the NF-zero. This phenomenon also explained the significantly higher growth rate (cell amount on 7day/ cell amount on 3 day) of MCT3T cells. The growth rate of MC3T3 on NF-high was about 6 times higher than on the NF-zero, because NF-high allowed cell migrated into deeper area when the surface area was fully occupied. More space in the NF matrices allowed the constantly proliferation of the cells. The AKP is an early osteoblast differentiation biomarker (Andrea Di Luca 2016). It showed that the AKP level on the NF-high was significantly higher than its on the NF-mid and the NF-zero ($p<0.05$). Our results have been supported by several previous publications. Andrea Di Luca et al. stated that the AKP activity of the hMSCs increased with the increase of scaffold pore sizes (Andrea Di Luca 2016). Using

gradient calcium polyphosphate scaffolds, we found that a much higher osteoblastic cell differentiation and mineralization can only be found on the area with larger pore sizes (> 250 μm), as manifested by AKP assay and position emission tomography scan (PET scan) (Chen L 2016). However, the similar changes cannot be observed in the RAW cells. The cell differentiation of RAW cells was not enhanced by the increase of the NF pore sizes. We propose that RAW cells are relatively small and need a relatively dense NF microstructure for the growth and differentiation. In addition, as compared to the MC3T3 preosteoblasts, the RAW cells have much stronger migration capacity that will help RAW cells to transform to osteoclasts during cell differentiation. The detail mechanism behind these differences is worthy further investigation.

The surface roughness of the ECM is another important factor that affects cell behavior. The average roughness of the native bone tissue is 32nm (Erica Palin 2005). The surface roughness of our samples was between 1 to 5 μm, in which the NF-high has the highest roughness (>4 μm), and the roughness decreased gradually with a slower collector movement (Figure 22). The surface roughness is closely related to cell attachment and differentiation. It had been reported that the presence of micron and submicron surface roughness on the scaffold enabled to robust bone differentiation (Mendonça G 2010, Gittens, McLachlan et al. 2011, Gittens RA 2011). One study examined osteoblasts differentiation on various titanium nanonodules with the diameters of 100, 300, and 500nm. They found the best differentiation of osteoblast was on the nanonodule with 500nm diameter (Ogawa, Saruwatari et al. 2008). These

findings are in agreement with our results, which the highest ALP level was found on NF-high.

As bone is a highly mineralized tissue with high stiffness, in order to better mimic the ECM of bone, biomechanical modification of the scaffold is necessary. In addition, bone cells are very sensitive to the stiffness of the ECM; for example, the maintenance of the osteoblasts phenotypes needs a ECM with a relatively high stiffness, while the chondrocytes would dedifferentiate where they grow at a rigid area (Weber, Bjerke et al. 2011). NFs is a relatively soft scaffold compared to other CaP ceramic bone substitutes, thus the fiber mineralization is important for the enhancement of the fiber stiffness. H.S. Yu et al. added hydroxyapatite into a PCL nanofiber surface, which showed the improvement of osteoblasts adhesion and growth than non-mineralized NFs (Jang, Castano et al. 2009, Yu, Jang et al. 2009). The single NF stiffness of the NF-low, -mid and –high was increased significantly by the higher crystallinity than the NF-zero ($p<0.05$). We propose that the better cell proliferation and differentiation on these samples than they on the NF-zero that might due to their relatively higher NF stiffness. The increased NF stiffness enhanced the cell response, such as adhesion (Wei S. 2017), growth (Yu, Jang et al. 2009) and differentiation (Rosenzweig, SolarCafaggi et al. 2012). .

In order to better mimic the bone ECM matrices and enhance cell growth and differentiation, we plan to develop the 3D NF scaffold to a local drug delivery tool by embedding bioactive agents/drugs in polymer solutions before electrospinning. The candidates of biomolecules can be glycosylation (Zhang

and Ten Hagen 2011) and fibronectin (stimulating cell adhesion and proliferation), bone morphogenetic protein 2 (BMP-2) (stimulating MSCs differentiation to osteogenic linage and calcification (Li, Vepari et al. 2006), and antibiotics (prevent and treat local bone infection) (Song, Yu et al. 2013, Song, Seta et al. 2017). Moreover, mechanical stimuli could be induced by dynamic cell culture via bioreactor system to mimic the movement of physiological fluid.

In conclusion, the microenvironment of the NFs affected cell behavior. Larger pore sizes and porosity, increased surface roughness and stiffness assist cell infiltration, growth and differentiation. In the next chapter, we would embed Strontium Chloride ($SrCl_2$) into a coaxial 3D NF with the aim to enhance osseointegration. In that study, we would select the NF-high formula to fabricate a Sr^{2+} doped coaxial 3D NF because the pre-osteoblasts have best proliferation and differentiation on the NF-high.

CHAPTER 4 DEVELOPMENT OF SR^{2+}-DOPED PCL/PLGA-PVA COAXIAL NFS FOR OSSEOINTEGRATION ENHANCEMENT

Introduction

The lack of early osseointegration is one of the major reasons of orthopedic implant failures (Song, Seta et al. 2017). Every year in the Unite State about 600,000 fractures have delayed union and 100,000 fractures are nonunion (Bishop, Palanca et al. 2012, Goodman, Yao et al. 2013). Some joint prosthetics cannot integrate to the surrounding bone (Aro, Alm et al. 2012). Many researches have confirmed that defective rapid osseointegration causes implant instability, micromotion, osteolysis and loosening (Song, Seta et al. 2017). Ryd et al. reported that implant instability and micromotion in both hips and knees might result in implants failure (Ryd 1992). These facts stimulate scientists to develop and modify the implant surface because the physiochemical and biological properties highly impact the quality and quantity of implant early osseointegration (de Jonge, Leeuwenburgh et al. 2008).

Many implant surface coatings have been developed. One of the earliest used coatings is hydroxyapatite (HA) coating for titanium (Ti) implants. It was used to enhance bone ingrowth; however, recent clinical studies found there is no significant difference of long-term clinical outcomes between HA coated hip replacement and cementless hip replacement (Song, Seta et al. 2017). It may be caused by the brittle nature of HA coating, poor adhesion strength and uncontrollable drug release. Other coatings techniques like layer-by-layer (LBL), hydrogel coating and immobilization have limitations such as lack of controllable drug release, expensive, and mechanical instability (Goodman, Yao et al. 2013).

Therefore, more research efforts are needed to develop a ‘bone-like’ implant surface at nanoscale to enhance osseointegration.

Electrospun nanofibers (NFs) are one of promising substitutes to mimic the nano-fibrous collagen network of the bone extracellular environment. The advantages of nanofibers include its high surface area and high mass to volume ratio, which could activate cell responses such as cell adhesion and proliferation (Ifkovits, Sundararaghavan et al. 2009). Both Wang X. et al. and Huang Z et al. demonstrated that the physiochemical properties of the NFs can be used to create an osteogenic environment without use of exogenous factors, because it assisted osteoblasts attachment, proliferation and differentiation in vitro (Huang, Daniels et al. 2008, Kohgo, Yamada et al. 2011, Wang, Gittens et al. 2012). The electrospun NFs can also be used as a controllable drug release system via forming a coaxial core-sheath structure (Gluck, Rahgozar et al. 2011). The coaxial electrospinning is a process where a concentric spinneret can accommodate two different polymer solutions (Gluck, Rahgozar et al. 2011).

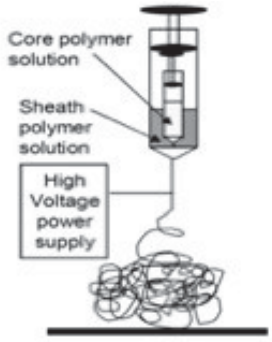

Figure 32. Spinneret for coaxial electrospinning

During the electrospinning the coaxial setup allows for the injection of one solution into another at the tip of customized spinneret (Figure 33). The sheath solution acts as a guide and surrounds the core solution. The sheath structure represents a physical barrier to reduce the initial burst release and

protects the drugs in the core fiber. We have developed a coaxial electrospun polycaprolactone/polyvinyl alcohol (PCL/PVA) NFs. The PCL was chosen because of its ideal biocompatibility, slow degradation rate and good mechanical properties (Lee and Goodman 2008, Pulido, Ghanem et al. 2008). The PVA had good fiber formation property, which was used as the core material for drug reservoir. Doxycycline (Dox), a tetracycline class antibiotic, was loaded. The results showed the Dox was released from the coaxial PCL/PVA NFs constantly and sustainably for more than 4 weeks (Song, Seta et al. 2017). The slow degraded PCL reduced the doxy diffusion from PVA (core materials. Thus, the controllable drug release from coaxial NFs is achieved by concentration gradient and the degradation rate of the barrier (Szentivanyi, Chakradeo et al. 2011). We also observed that these coaxial NFs significantly enhanced the attachment and proliferation of murine pre-osteoblasts MC3T3-E1 cells (Song, Yu et al. 2013).

Next，we tried to coat the titanium (Ti) implant with the optimized coaxial PCL/PVA NFs. The Dox doped coaxial PCL/PVA NFs were directly deposited on the Ti implant surface during electrospinning with the aim to improve osseointegration. The bone-implant surface (%) in the NFs coated titanium implant groups was significantly higher ($p<0.05$) than the non-coating groups after implantation 2, 4 and 8 weeks in a Staphylococcus aureus infected tibia implantation rat model (Song, Seta et al. 2017). In addition, the Dox loaded NFs inhibited bacterial growth up to 8 weeks in vivo (Song, Seta et al. 2017). These two studies showed the great potential of NFs in the enhancement of implant osseointegration, and established techniques of coaxial electrospinning and drug

release testing methods for further study. However, the coaxial NFs we used did not have the 3D structure. In the previous chapters, we have shown the benefit of 3D NFs with larger porosity and pore size to the pre-osteoblasts cell growth. 3D NFs should behave better for early osseointegration than the 2D NFs. Another shortage is the relatively slower degradation rate of PCL both in vitro and in vivo (6 month or longer) (Fu, Meng et al. 2014). A match of NF coating degradation rate with the physiology of osseointegration (~1 month) is critical (Lu, Peter et al. 2000).

In this study, we would develop a coaxial polycaprolactone (PCL)/ poly (lactide-co-glycolide) (PLGA) ^{sheath}-polyvinyl alcohol (PVA) ^{core} nanofibers matrix. PLGA is a FDA-approved co-polymer of poly lactic acid (PLA) and poly glycolic acid (PGA) with long clinical experience (Dawes, Fratila-Apachitei et al. 2010). In the past two decades the PLGA has been used as a vehicle for sustained drug delivery. A controllable drug release by PLGA is coupled with its degradation rate (Makadia and Siegel 2011). The rate of PLGA degradation could be controlled by manipulating the composition and ratio of the co-polymers. For example, PLGA with 50:50 PLA: PGA ratio exhibits the fastest degradation (about one month). In order to match the physiological osseointegration rate (~1month), we selected the PLGA with 50:50 PLA: PGA in this study (Abdal-hay, Hwang et al. 2012, Xiao, Liu et al. 2014). To better control the degradation rate of sheath solution, we mixed PCL with PLGA with the ratio of 4:1, 1:1 and 1:4 (v/v), and proposed that the incorporation of faster degrading PLGA could speed up the degradation rate of the sheath fiber. Another benefit of PLGA is its stronger binding to the Ti

surface than that of PCL. One reason for this is that PLGA has a much higher ratio of oxygen atoms in its molecular structure than does PCL, which provides for more electrostatic interactions of the Ti surface with coated NF matrices (Makadia and Siegel 2011). We proposed to identify an optimal formula to fabricate coaxial NFs from these three ratios based on the morphology, in vitro degradation rate (weight change), and albumin release study. Based on that, we would produce 3D coaxial NFs by automatic 3D NFs collector. The fastest collector movement was selected based on the data generated in Chapter 3.

Strontium (Sr^{2+}) is a minor element and can be found in our body and daily diet. Approximately, 99% of Sr^{2+} ions deposit in bone. Like calcium ion, the Sr^{2+} ion has the similar cellular transport pathway, which has strong affinity for the incorporation in the bone matrix during mineralization (Nielsen 2004, Meka, Jain et al. 2016). Sr^{2+} enhances bone strength through the inhibition of osteoclasts and activation of osteoblasts (Marie 2003, Barbara, Delannoy et al. 2004, Yang, Yang et al. 2011, Schumacher, Lode et al. 2013). The molecular mechanism of Sr^{2+} action is in part due to the activation of calcium-sensing receptors (CaSRs) (Schumacher, Lode et al. 2013). Data from a clinical trial of osteoporosis patients under the administration of 2g/day strontium ranelate concluded a significant increase of bone mineral density (Reginster, Seeman et al. 2005, Meunier, Roux et al. 2009). However, several long-term side effects have been reported in patients who have taken high dose of strontium containing drugs (Nielsen 2004, Lee, Lie et al. 2009). Local delivery of Sr^{2+} ion is an alternative method for the supplement of Sr^{2+} ions in the body. Many researchers have reported the

benefits of applying strontium doped biomaterials, including calcium phosphate (Kim, Koh et al. 2004, Zhang, Shen et al. 2011), nanofibers, and bio-glass (Kim, Koh et al. 2004). In this study, we planned to develop Sr^{2+} doped coaxial PCL/PLGA-PVA NFs as the implant coating material to enhance osseointegration. Studies regarding the role(s) of Strontium in implant osseointegration are limited and still at the experimental stage (Karrholm, Borssen et al. 1994, Makadia and Siegel 2011). Park *et al.* found that Sr^{2+}-embedded titanium (Ti) implants significantly enhanced implant osseointegration in a rabbit tibia implantation model (more bone apposition on the implant surface and higher bone-to-implant contact percentages), as compared with the control Ti implants. In addition, Strontium enhances angiogenesis by stimulating the proliferation of endothelial cells (Kurtz, Ong et al. 2010) and increasing the production of vascular endothelial growth factor (VEGF) (Bozic, Kurtz et al. 2009). These findings are important because angiogenesis at the implant/bone interface plays a key role in the early osseointegration.

In this study, we developed Sr^{2+} doped coaxial 3D PCL/PLGA-PVA NFs. The physiochemical properties of formed coaxial 3D PCL/PLGA-PVA NFs have been extensively tested, including in vitro drug release profiles and mechanical properties. In addition, the biological behaviors of MC3T3 pre-osteoblasts were carefully evaluated by both indirect and direct contact methods. Data generated from these experiments provided essential information for the further in vivo testing of Sr^{2+}-doped coaxial NFs as Ti implant coating using a rat tibia implantation model.

Materials and Methods

Polycaprolactone (PCL, Mw = 70,000−90,000), PVA (mw ~205,000), Poly (D,L – lactide-co-glycolide) (PLGA, Mw=54,000-69,000), chloroform, and dimethyl- formamide (DMF) were purchased from Sigma-Aldrich (St. Louis, MO). Alphamodified Minimum Essential Medium, trypsin, fetal bovine serum, penn/strep and Dulbecco's phosphate-buffered saline (DPBS buffer) were purchased from Invitrogen (Grand Island, NY). CelLytic MT cell lysis reagent was purchased from Sigma-Aldrich (St. Louis, MO). Murine MC3T3-E1 pre-osteoblast cell line and murine pre-osteoclast RAW 264.7 cells culture was purchased from American Type Culture Collection (ATCC, Manassas, VA). Quant-iT Pico- Green dsDNA Assay Kit was purchased from Thermo Fisher Scientific (Waltham, MA). Cytotoxicity Detection Kit (LDH) and Alkaline Phosphatase Activity Colorimetric Assay Kit were purchased from BioVision (Milpitas, CA).

Fabricate and define optimal formula of coaxial 3D PCL/PLGA-PVA NFs

11% (w/v) PCL and 15% (w/v) PLGA was prepared by dissolving PCL and PLGA respectively into chloroform/dimethylformamide (DMF)(1:1,v/v) overnight to homogenize (Song, Yu et al. 2013). 15% (w/v) PVA was prepared by dissolving PVA into distill water. In order to adjust the degradation rate of the sheath solution, the PCL/PLGA mixer was prepared by the ratio of 4:1, 1:1 and 1:4 (v/v). Coaxial electrospinning was achieved by using custom made coaxial nozzle composing of a hollow t-junction with fully penetrating 19-gauge core needle. PCL/PLGA mixer (sheath) and PVA (core) were uploaded to the 5 ml syringes. The syringes were attached to the syringe pumps set at flow rate (Q) of

1ml/h for PCL/PLGA and 0.48ml/h for PVA. 20 KV voltages were applied to the nozzle. The distant between nozzle and collector was 10 cm. The three types of coaxial NFs, PCL/PLGA (4:1)-PVA NFs, PCL/PLGA (1:1)-PVA NFs, and PCL/PLGA (1:4)-PVA NFs, were collected by automatic 3D NF collector at the moving speed of 0.232mm/min. Six rounds of electrospinning were conducted at 10min/round. The optimal formula of coaxial NFs would be decided by transmission electron microscopy (TEM), in vivo degradation and albumin release study.

Transmission electron microscopy (TEM):

The Coaxial PCL/PLGA (4:1)-PVA NFs, PCL/PLGA (1:1)-PVA NFs, and PCL/PLGA (1:4)-PVA NFs were directly deposited onto Cu-grids covered with ultrathin carbon layers and observed under a TEM (jeol-2010 FasTEM, USA) at accelerating voltage of 200 kV to characterize its coaxial structure.

In vitro degradation:

The degradation rate of NFs was presented by weight change. 0.1 g (Wo) three types of coaxial NFs were entirely soaked in ultrapure water at 37°C respectively. The NFs were air dried after 1 week, 1 month and 3 month and measured the dry weight (Wi). The percentage of weight remain was calculated by equation (2):

$$\text{Weigh remain } (\%) = (Wo - Wi)/Wo * 100\% \quad (2)$$

Albumin release study:

Albumin-FITC were incorporated into both sheath and core solution at the final concentration of 0.11mg/ml and 0.35mg/ml respectively. Three types of

coaxial NFs were soaked into ultrapure water (0.1g/ml). The eluent was totally collected and replaced at time points of 1, 2, 4, 6 hour, 1, 2, 5 days, 1, 2, 3, and 4weeks. The fluorescence intensity of collected eluent at each time point was measured by UV/VIS Spectrophotometer (BioTek Synergy HT, USA) with excitation/emission wavelength of 485/528nm. The albumin release curve was created by time versus albumin release percentage.

Fabricate coaxial 3D Sr^{2+} doped PCL/PLGA (1:1)-PVA coaxial 3D NFs

Strontium chloride was loaded into both sheath and core solutions with the 10mmol/ml final concentration. The Sr^{2+} dose selected is based on previous reports of both in vitro and in vivo animal studies (de Jonge, Leeuwenburgh et al. 2008). The optimal formula of PCL/PLGA was 1:1 (v:v). The Sr^{2+} doped coaxial NFs were fabricated as described previous.

Transmission electron microscopy (TEM)

The TEM was used to observe the coaxial structure of formed the NFs. The Sr^{2+} doped coaxial PCL/PLGA-PVA nanofibers were directly deposited on onto Cu-grids covered with ultrathin carbon layers and observed at accelerating voltage of 200 kV. Dispersive X-Ray spectrometry (EDAX) was used to analyze the chemical composition in area of sample surface of interest.

3D confocal laser scanning microscopy (CLSM)

Samples were scanned by a color 3D confocal laser-scanning microscope (Keyence VK-9700, Itasca, IL) [3D]. The pore volume distribution and total pore volume were measured using VK-Analyzer software (Keyence). For pore volume measurements (color height image, 400× magnification), about 100 pores at the

same height along the z-axis were selected and their volumes measured individually in each scaffold (n = 3). The pore volume distribution was calculated as the percent of a range of pore volumes versus the total pore volume.

Macro-tensile testing

NF scaffolds were cut into 3.8 × 1.3 cm rectangular dumbbell-shaped tensile testing samples with cross sectional width of 0.9 cm for testing region. Sample thickness was measured with an iGAGING caliper (iGAGING, San Clemente, CA). Macro-tensile measurements were performed using an electromechanical universal tester (Instron, Elancourt, France). All samples were mounted between holders at a distance of 1 cm. Tensile testing was conducted at a rate of 0.1 mm/s.

Strontium (Sr^{2+}) in vitro release study

The strontium doped coaxial NF was immersed in ultrapure water (0.1g/ml) at 37 °C. The eluent was totally collected and replaced with the same amount of water at time points, 1, 2, 4, 6 hour, 1, 2, 5 days, 1, 2, 3, 4, 5, 6, 7, and 8 weeks. We measured Sr^{2+} concentration using an inductively coupled plasma optical emission spectrometry system (ICP-OES, Thermo Fisher Scientific, Waltham, USA). The samples were diluted in 13.5ml distill water and 0.5ml HNO_3 for analysis. The concentration was determined from standard curve prepared by salt solution of known concentration.

Scanning electron microscopy (SEM)

The 3D coaxial NFs after Sr^{2+} release were gold-coated (Gold Sputter EFFA Coater, Redding, CA, USA) and the morphology of the NFs was

characterized by scanning electron microscopy (SEM) (JSM-6510LV-LGS, MS, USA) at a 25kV accelerating voltage.

Cellular study—indirect contact

According to the strontium release curve, the eluent collected at 4 hours, 1, 2, 3 and 4 weeks time points were selected for cell study. The eluent treated preosteoblasts cell would be test for toxicity, proliferation and differentiation. We would use the similar approach for cell culture and test described in Chapter 3.

Proliferation:

The MC3T3-E1 cells were seeded into 24 well plates with the amount of $1.5x10^5$/well. After cell attached, 50μl eluent at different time point was added into each well respectively. Cell culture medium was collected for toxicity test and refreshed every 3 days, at the same time, 50μl eluent at different time points were added as well. The cellular proliferation was measured by DNA quantification through Qaunt-iT Pico-green DNA kit after 3 days and 7 days culture. Briefly, the cells grown on the NFs were lysed by mixing with 200 μl CelLytic MT cell lysis reagent overnight at 4 °C. 50 μl cell lysate was mixed with 50 μl PicoGrenn dsDNA reagent and then added into 96 well plates. The fluorescence values were measured by microplate reader at 528 nm after excitation with 485 nm light. The DNA concentration was converted from an OD value on the basis of standard curve.

Toxicity:

LDH reagent was mixed by dye solution and catalyst (45:1,v:v), and then 100 μl reagent was added into 96 well plated followed by adding 50μl collected

medium at different time points. Microplate reader was used to measure the color changes at 450nm.

Differentiation:

After cell seeding, MC3T3 cells were cultured in osteogenic media containing 10 mM β-glycerophosphate and 50 μg/ml L-ascorbic acids for 14 days. The cell culture medium and different time points eluents were replaced every 3 days. The cell differentiation levels were measured by alkaline phosphatase (ALP) assay(Song, Markel et al. 2012). Briefly, the cells were lysed overnight. The ALP activity in the cell lysates was measured utilizing the conversion of a colorless p-nitrophenyl phosphate to a colored p-nitrophenil. Microplate reader was used to measure the color changes at 405nm. The AKP activity levels were normalized and converted from optical density (OD) value to protein concentration based on the standard curve.

Cellular study—direct contact

The MC3T3-E1 cells were directly seeded on the Sr^{2+} doped coaxial NFs and coaxial NFs with the amount of $8X10^4$ cells/scaffold. The cells were cultured and tested (proliferation, toxicity and differentiation) by the same methods described above.

Results

Define the optimal formula of coaxial 3D PCL/PLGA-PVA NFs

Three types of coaxial NFs with different sheath ratios, PCL/PLGA (4:1), PCL/PLGA (1:1), and PCL/PLGA (1:4), were successfully produced. They all formed clear coaxial structures (Figure 33).

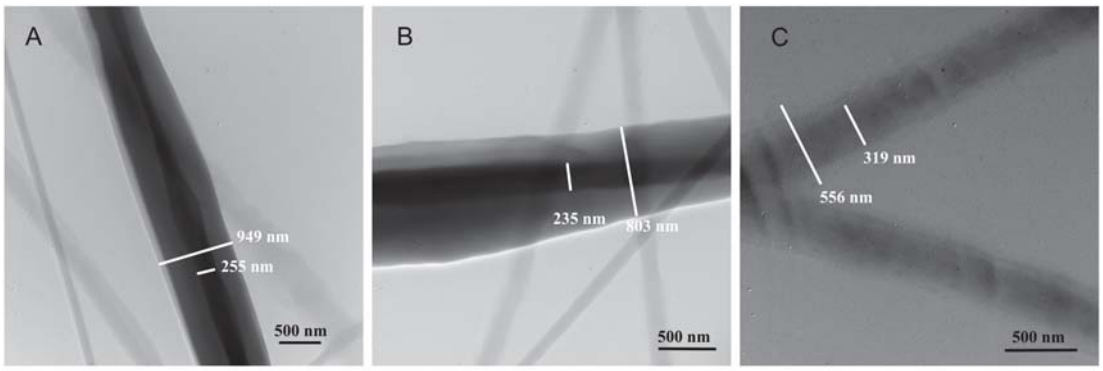

Figure 33. TEM images show the coaxial structure of 3 types of NFs. (A) PCL/PLGA(4:1)^{sheath}-PVA^{core}; (B) PCL/PLGA(1:1)^{sheath}-PVA^{core}; (C) PCL/PLGA(1:4)^{sheath}-PVA^{core}

The PLGA did accelerate the degradation rate of PCL. As shown in Figure 34, at 3 month, the remained weight of coaxial NFs was conversely proportional to the amount of PLGA. About 60%, 40% and 10% NFs remained for PCL/PLGA (4:1), PCL/PLGA (1:1), and PCL/PLGA (1:4). At the same time, the PCL decreased the degradation rate of PLGA, which used to degrade within one month. There was no obvious difference of cumulative albumin release curve between three types of coaxial NFs, and all of them were able to sustain release the albumin over a month (Figure 35).

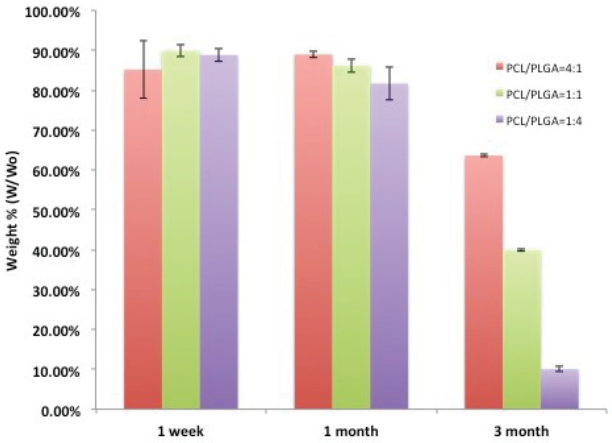

Figure 34. The remained weight of three coaxial PCL/PLGA-PVA NFs after 1 week, 1month and 3 month degradation in vivo (n=3).

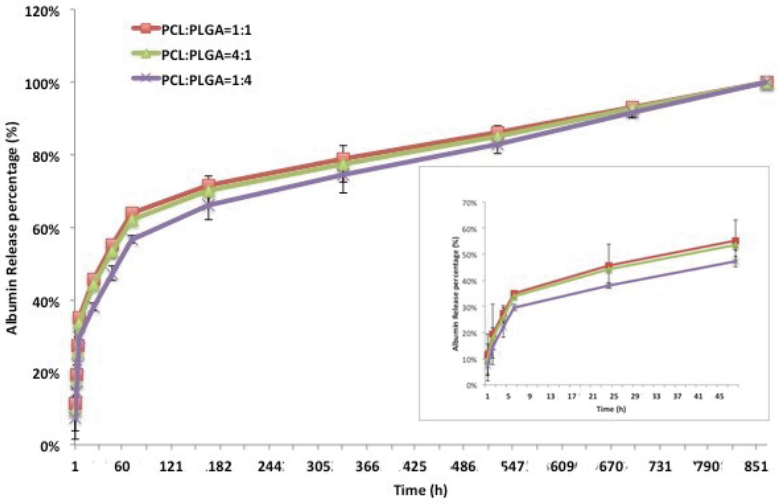

Figure 35. The cumulative albumin one-month release curve (n=3)

According to these three studies, we chose PCL/PLGA (1:1) as the optimal sheath ratio, because it had clear sheath-core structure and enabled to release albumin over a month. A sufficient osseointegration resulting in "the formation of a direct interface between an implant and bone without intervening soft tissue" is critical for the early implant stability (~ 1 month)(Lu, Peter et al.

2000). The degradation rate may be slower than the osseointegration rate in physiological condition, but we believed the NFs with slightly slower degradation rate could keep a constant local microstructure and mechanical strength, which were still important for cell growth.

The physiochemical properties of coaxial 3D Sr^{2+} doped PCL/PLGA (1:1)-PVA NFs

The coaxial 3D Sr^{2+} doped PCL/PLGA (1:1)-PVA NFs had clear sheath and core structure (Figure 36). The ratio of diameter sheath to core was about 4:1. The hydrophilic $SrCl_2$ could not mix evenly with the hydrophobic PCL/PLGA solution. As the result, several Sr^{2+} clusters can be found in the sheath of NFs, as manifested by the EDAX measurement.

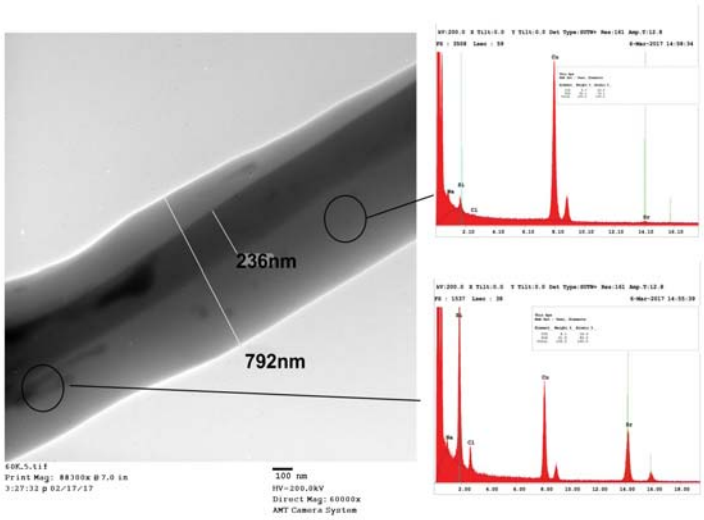

Figure 36. The TEM image showed the clear core/sheath structure of Sr^{2+} doped coaxial PCL/PLGA (1:1)-PVA nanofibers. EDAX was analyzed several Sr^{2+} clusters on the sheath

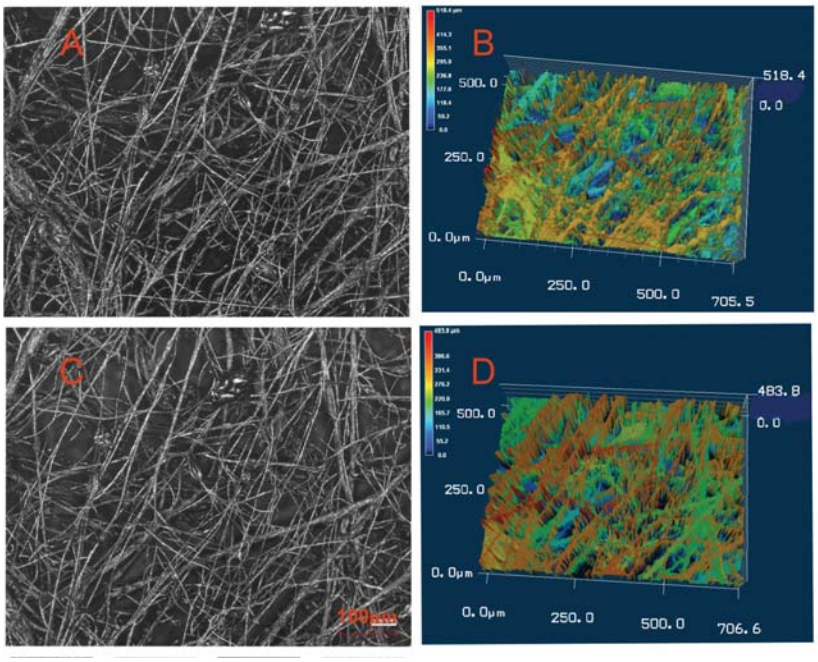

Figure 37. Laser intensity images of coaxial PCL/PLGA (1:1)-PVA NFs (A) and Sr^{2+} doped coaxial PCL/PLGA (1:1)-PVA NFs (C). 3D images of coaxial PCL/PLGA (1:1)-PVA NFs (B) and Sr^{2+} doped coaxial PCL/PLGA (1:1)-PVA NFs (D) by LSCM at 400x magnification. Images scanned by Ameer Al-Shawk

We further compared the microstructure and tensile strength of coaxial 3D PCL/PLGA (1:1)-PVA NFs with and without Sr. The fibrous and 3D structure of coaxial NFs (Figure 38 A and B) and Sr^{2+} doped coaxial NFs (Figure 37 C and D) were observed by LSCM. Based on the height images (400x), VK-Analyzer software was used to measure the total pore volume and the individual pore volume of each sample. The total pore volume of the Sr^{2+} doped coaxial NFs was significantly higher than the NFs without Sr^{2+} ($p<0.05$) (Figure 38).

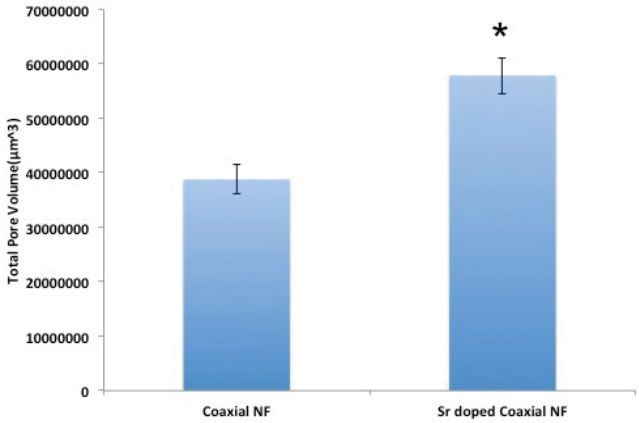

Figure 38. The total pore volume of Sr^{2+} doped coaxial PCL/PLGA (1:1)-PVA NF was significant ($p<0.05$) higher than coaxial NFs (n=3). 3D scanning data measured by Ameer Al-Shawk

For pore volume distribution (Figure 39), in the range of <100,000 μm^3, the pore amount percentage of coaxial NFs was higher than the NFs with Sr^{2+}; whereas in the range of >100,000 μm^3, the pore volume amount of coaxial NFs with Sr^{2+} (54%) was much higher than the other one (18%). Combined these data together, the coaxial NFs with Sr^{2+} had looser structure than the NFs without Sr^{2+}. The looser structure of Sr^{2+} doped coaxial NF directly decreased its ultimate tensile stress (~0.1 N/mm^2), which was significantly lower than the ultimate tensile stress of the coaxial NFs without Sr^{2+} (~0.6 N/mm^2) ($p<0.05$) (Figure 40).

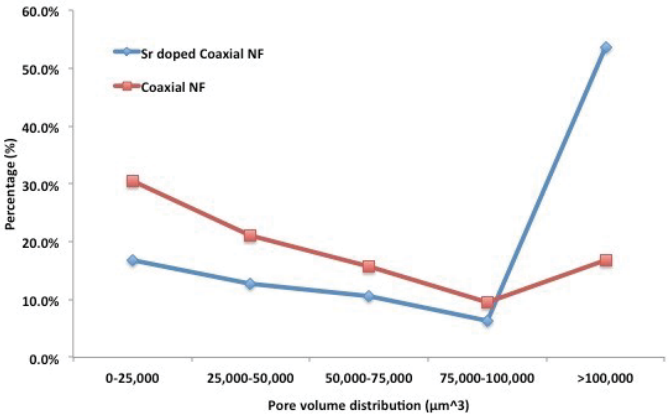

Figure 39. Pore volume distribution of Sr^{2+} doped coaxial PCL/PLGA (1:1)-PVA NFs and coaxial PCL/PLGA (1:1)-PVA NFs. 3D scanning data measured By Ameer Al-Shawk

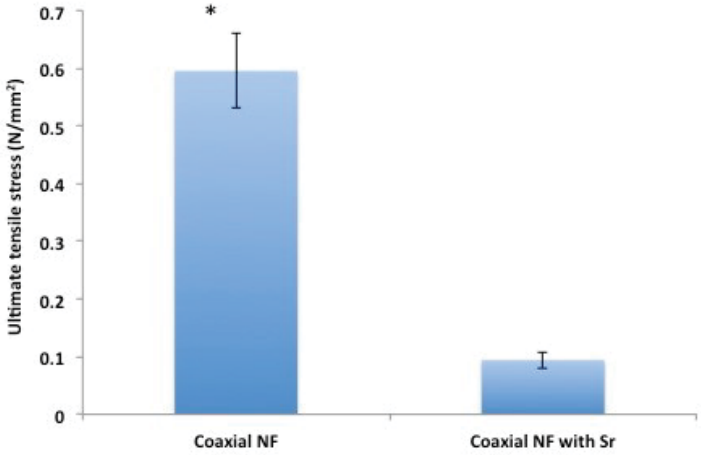

Figure 40. The ultimate tensile stress of coaxial PCL/PLGA (1:1)-PVA NFs was significant ($p<0.05$) higher than the Sr^{2+} doped coaxial PCL/PLGA (1:1)-PVA NFs, n=3.

Strontium (Sr^{2+}) release study

ICP-OES results confirmed that Sr^{2+} ions were released from coaxial NFs when incubated in an aqueous environment. Figure 41 presented a cumulative Sr^{2+} ions release curve. Initial burst release was still found within 6h incubation, in which the maximum Sr^{2+} ions release was 32.25 ppm at 4 hour (Figure 41).

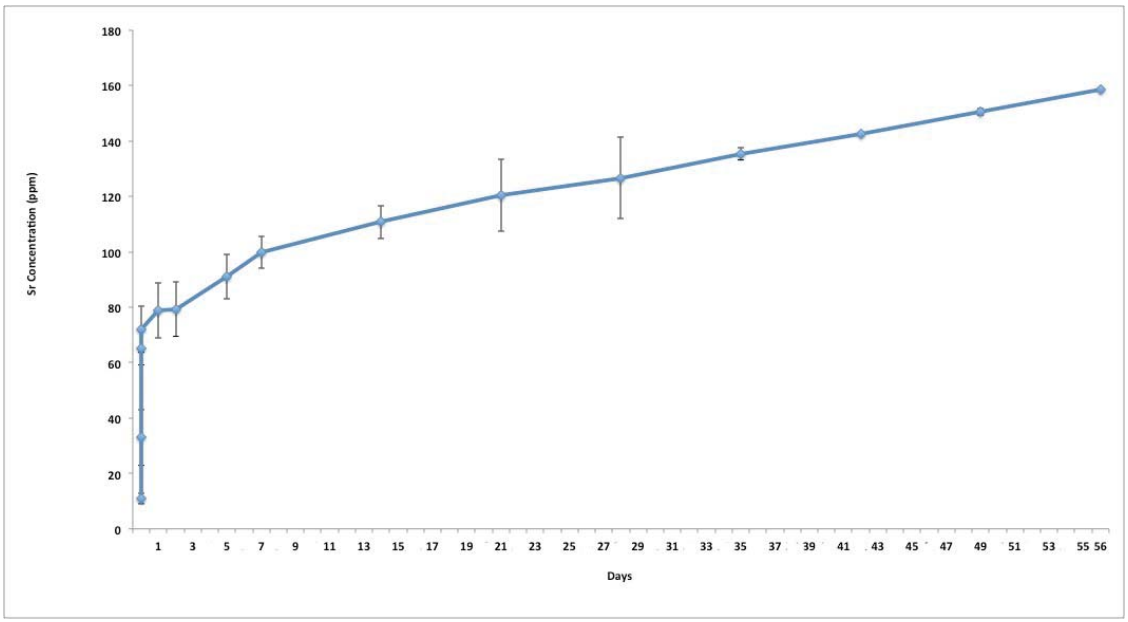

Figure 41. The cumulative Sr^{2+}release curve in 2 month, n=3.

Thereafter, a steady Sr^{2+} ions release was observed at following time points. Overall, the Sr^{2+} ions were released constantly over 2 month. The Sr^{2+} ions concentration measured at last time point (2 month) still had 11.01 ppm. The SEM images of the Sr^{2+} doped coaxial NFs before (Figure 42 A and D) and after (Figure 42B and E) degradation revealed different morphology. After degradation, the fibers were bundled together (Figure 42 B), and clear gaps were found on the sheath for Sr^{2+} ions leak out (Figure 42 D, red box). The images of degraded coaxial NFs without strontium were showed in Figure 42 C and D. No

gaps were founded in these NFs, and the inner fiber was exposed after sheath degradation (Figure 42D).

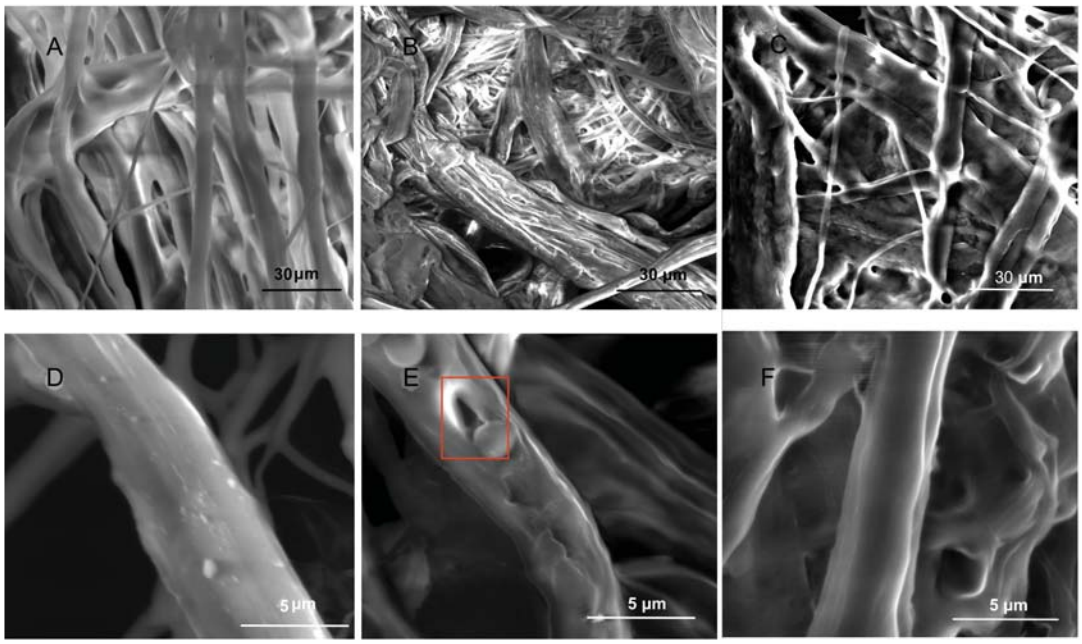

Figure 42. SEM images of Sr^{2+}doped coaxial PCL/PLGA (1:1)-PVA NFs before degradation (A and D), and after two-month degradation (B and E). The gap formed after Sr^{2+} cluster release (red box in E). No gaps found in degraded pure coaxial PCL/PLGA (1:1)-PVA NFs (C and F).

In vitro cellular study—indirect contact

The MC3T3-E1 cells were firstly treated by five eluents based on the release curve (Table 2).

Name	Eluent-1	Eluent-2	Eluent-3	Eluent-4	Eluent-5
Collected time	4 hour	1 week	2 week	3 week	4 week
Concentration (μg/ml)	32.25	11.01	9.53	8.75	6.28

Table 2 List of five eluents for cell treatment

Negative control groups were the cells treated by the eluent of pure coaxial NFs (without Sr^{2+}) collected by corresponding time points. The NFs with or without Sr^{2+} were non-toxic to the cells, as demonstrated by undetectable LDH activity in the culture medium at different time points (Data not shown). We found that the DNA concentrations in cells cultured on NFs with Sr^{2+} were lower than that in cells cultured on NFs without Sr^{2+} (control), especially for the cells treated by eluent-2 and eluent-4 ($p<0.05$) (Figure 43 A). However, on 7 days in culture, the DNA concentrations of Sr^{2+} ions treated groups were increased. Except eluent-5 group, the Sr^{2+} ions treated cells' amounts were higher than negative control groups (Figure 43B).

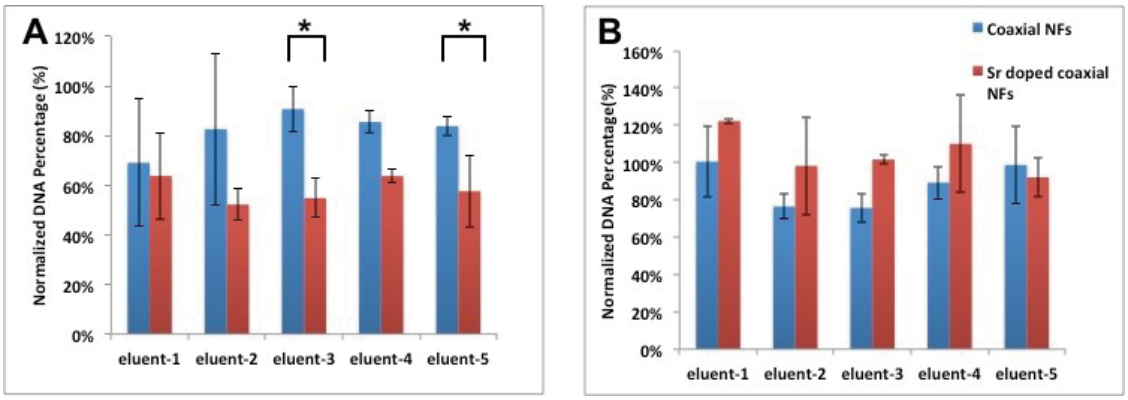

Figure 43. 3 day (A) and 7 day (B) normalized DNA percentage (%) of MC3T3-E1treated by eluents collected after degradation of coaxial PCL/PLGA (1:1)-PVA NFs and Sr^{2+}doped coaxial PCL/PLGA (1:1)-PVA NFs at 4 hour, 1, 2, 3, and 4 weeks respectively (n=3) ($p<0.05$). The DNA concentration of each group divides that of control group (without eluent treatment) to normalize data. Control group was 100%.

AKP enzyme activity was found to vary under the influence of difference Sr^{2+} concentration (Figure 44). Overall, the higher AKP concentration was found in the groups treated by Sr^{2+} ions contained eluent. It meant Sr^{2+} ions stimulated cell differentiation. In eluent-1 and -2 treatment group, the cell differentiation level of Sr^{2+}doped NFs group was significantly higher than the control (100%) and negative control groups respectively ($p<0.05$) (Figure 44).

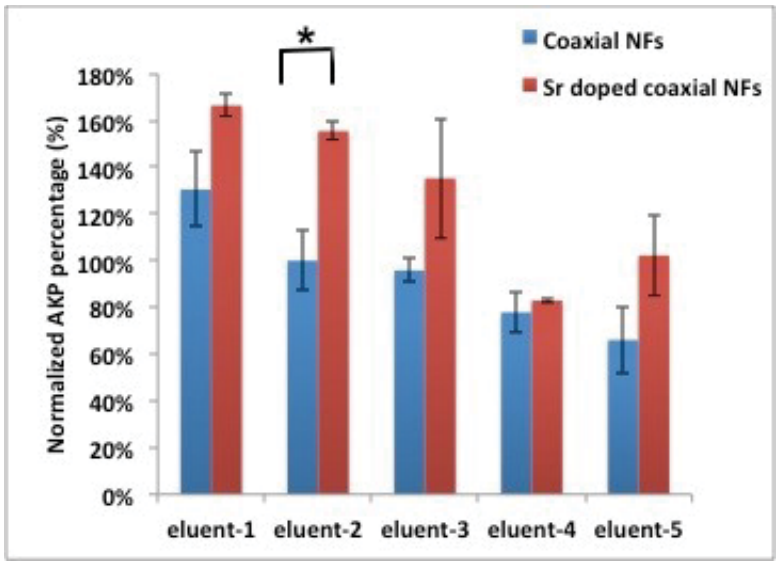

Figure 44. Normalized AKP percentage of MC3T3-E1 treated by eluents collected at different time points after degradation of coaxial PCL/PLGA (1:1)-PVA NFs and Sr^{2+}doped coaxial PCL/PLGA (1:1)-PVA NFs (n=3) ($p<0.05$). Control group was 100%.

In vitro cellular study—direct contact

In this study, the MC3T3-E1 cells were directly cultured on the NFs. The negative control group was the pure coaxial NFs, and the control groups means cell directly grown on culture well plate. Overall, the cell number of control groups was higher than other groups on 3 days (Figure 45A); whereas on 7day, the cell

amount in three groups was similar (Figure 45B). At day 3, the cell amount on Sr^{2+} doped NFs was significantly higher than the cell amount on NFs without Sr^{2+}. Like the in direct contact study, the Sr^{2+} enhanced the cell differentiation. The highest AKP enzyme concentration was found in Sr^{2+} doped NFs ($p<0.05$) (Figure 46).

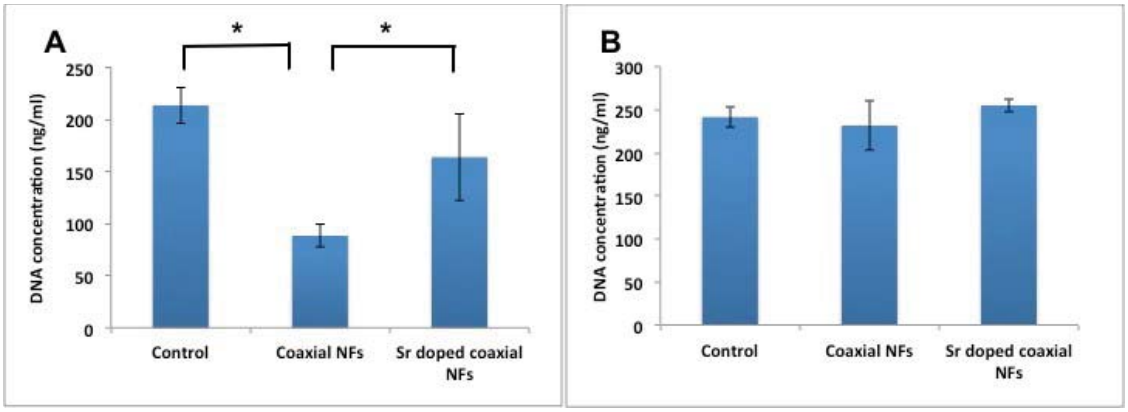

Figure 45. 3 day (A) and 7 day (B) DNA concentration (ng/ml) of MC3T3-E1 grown on culture plate (control), coaxial PCL/PLGA (1:1)-PVA NFs and Sr^{2+}doped coaxial PCL/PLGA (1:1)-PVA NFs respectively, n=3, $p<0.05$.

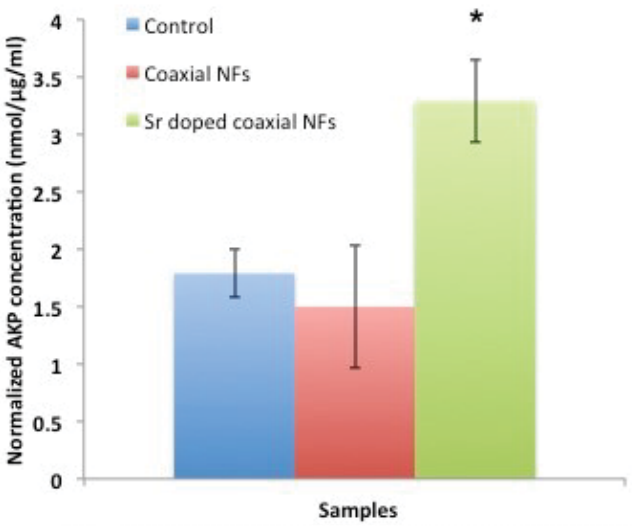

Figure 46. Normalized AKP concentration (nmol/ µg/ml) of MC3T3-E1 grown on culture plate (control), coaxial PCL/PLGA (1:1)-PVA NFs and Sr^{2+}doped coaxial PCL/PLGA (1:1)-PVA NFs respectively, n=3, $p<0.05$.

Discussions

Strontium ions can enhance osteogenesis by stimulating differentiation and function of osteoblast-like cells (Schumacher, Lode et al. 2013, Meka, Jain et al. 2016). Locally delivery of Sr^{2+} ions from bone substitutes for tissue regeneration is considered a promising approach since it could help to avoid the side effect of high dose treatment (Schumacher, Lode et al. 2013). In this study, the influence of Sr^{2+} ions doped coaxial 3D PCL/PLGA-PVA NFs on proliferation and differentiation of MC3T3-E1 cells was investigated in three steps. The in vitro Sr^{2+} ions release study; the cellular response to the Sr^{2+} ions contained eluents and cellular response in direct contact with the NFs were studied separately.

Firstly, we developed controllable Sr^{2+} release nanofibers. To accelerate the degradation rate of our previous developed coaxial PCL-PVA NFs being used

for Ti implant coating(Song, Seta et al. 2017), we added PLGA to the sheath solution (PCL) and developed coaxial 3D PCL/PLGA-PVA NFs that is expected to better match the osseointegration period (~ one month). The degradation rate of NFs is closely related to drug release kinetics (Song, Yu et al. 2013). For these NFs, we can adjust either the poly lactic acid (PLA) poly glycolic acid (PGA) ratio of PLGA or the ratio of PCL to PLGA to achieve ideal degradation rate. The degradation of PLGA is simply hydrolysis of the ester bonds in to lactic and glycolic acid (Lu, Peter et al. 2000). The higher content of hydrophilic glycolic acid units facilitates the absorption and diffusion of water, which results in the faster degradation (Crouch AS 2009). The degradation rate of PLGA (50:50) is about one month, which matches the osseointegration time in vivo. For this reason, the PLGA (50:50) was chosen for this study. We further defined the optimal ratio of PCL to PLGA. The PLGA with shorter degradation period should increase the degradation rate of PCL and PLGA mixture; at the same time, the PCL could decrease the period of PLGA degradation. The weight of three coaxial NFs with different PCL/PLGA ratio remained relatively constant within one month of degradation in water, followed by a dramatic change at 3 month (Figure 34). The remained NFs were conversely proportional to the amount of PLGA. About 60%, 40% and 10% NFs remained for PCL/PLGA (4:1), PCL/PLGA (1:1), and PCL/PLGA (1:4) at 3 month. Since PCL needs much longer time to degradation, we believed the main weight lost of the coaxial NFs was caused by PLGA degradation. Lichu Lu *et al.* found that the weight of PLGA (50:50) porous foams with 90% porosity were dropped 40% after 10 weeks incubation in PBS, and

before 8 weeks the weight change was slightly (Renwen Zhang 2004). Their findings of the PLGA degradation kinetics were similar to our results. We finally selected PCL/PLGA (1:1) mixture as the sheath solution, because this formula enables to create clear sheath/core structure. Although its degradation rate in vitro was slower than osseointegration in vivo, the degradation rate in vivo should be increased by autocatalytic effect that will be further evaluated in a planned in vivo animal model testing.

$SrCl_2$ as Sr^{2+} source was added into both sheath and core materials. The driving force of Sr^{2+} release out of the NFs is gradient concentration. In diffusion across a barrier (sheath), the driving concentration gradient is between the reservoir (core) and the release environment, which are separated by a barrier (sheath). The barrier with slower degradation rate should inhibit burst release of drug and prolong the release period. However, the burst release was still founded in Sr^{2+} release curve, where Sr^{2+} concentration was about 11, 21 and 32 μg/ml (ppm) at 1, 2 and 4-hour time points (Figure 41). The concentration dramatically decreased at 6-hour time point (6.9 μg/ml), and then the concentration fluctuated between 6 to 11 μg/ml by following time points. In the TEM image (Figure 36), many Sr^{2+} clusters were observed in the sheath. As long as the NFs incubated in water, the Sr^{2+} from the cluster diffused first, which left many gaps in the sheath (Figure 43 E). The Sr^{2+} from the core fiber would release out of the sheath via these gaps. Thus, incomplete sheath structure resulted in the burst release of Sr^{2+}. In addition, compare to the coaxial NFs without Sr^{2+}, the Sr^{2+} doped NFs had looser structure with higher total pore

volume (Figure 38) and larger pore volume (Figure 39) because of much lower fiber formation efficiency of Sr^{2+} doped NFs. The larger pore and porosity enhanced contact surface between water and NFs(Lu, Peter et al. 2000). It also accelerated Sr^{2+} release. Although the burst release was observed in our developed NF system, the merit of these NFs was constantly released Sr^{2+} over 2 months. We believe this character should satisfy our requirements.

Indirect cell culture was performed first to evaluate the impacts of culture medium eluents collected at defined time points (containing different concentration of released strontium and other degraded products) on pre-osteoblastic MC3T3-E1 cells. Five types of eluents collected at 4 hour, 1, 2, 3 and 4 weeks after NF incubation was chose (Table 2). Their Sr^{2+} concentration was 32.25, 11.01, 9.53 , 8.75, and 6.28 μg/ml respectively. The final concentration for cell treatment was diluted 10 times by adding 10% (v/v) of eluent into cell medium, which means the concentrations were 3.225, 1.101, 0.953, 0.875 and 0.628 μg/ml corresponding to each time point. Sr^{2+} can trigger mitogenic signal for promoting cell proliferation and survival by act as an agonist for the calcium-sensing receptor (CaSR)(Pi and Quarles 2004, Caverzasio 2008, Brennan, Rybchyn et al. 2009). It had been reported that the Sr^{2+} concentration between 0.5-5mM (44-440 μg/ml) is required for the enhancement of osteoblast-like cells activity in vitro (Morohashi, Sano et al. 1994, Lopez-Hallman 2013). The Sr^{2+} concentrations we used were much lower than this range. Generally, on 3 day, the cells were not sensitive to the various concentration of Sr^{2+} (Figure 43A); on day 7, the cell amount on Sr^{2+} positive group was increased (Figure 43B),

especially in eluent-1 group, the cell amount increased more than 2-folder on day 7 comparing to day 3 under the treatment of 3.225 μg/ml Sr^{2+} (Figure 43). M. Schumacher et al. studied the impact of Sr^{2+} concentration of up to 10mM on human bone marrow derived meschnchymal stem cells (hMSCs) by adding different amount of $SrCl_2$ (Schumacher, Lode et al. 2013). They concluded that constantly adding Sr^{2+} over 14 days with the concentration between 0.01 to 0.1 mM (0.8-8.8 μg/ml) benefited cell proliferation (Meka, Jain et al. 2016). They also found the amount of hMSCs did not obviously increased by higher concentration of strontium under shortly exposure (1-7 days) of strontium (Gittens, McLachlan et al. 2011). This findings could explain the slightly cell number change on 3 day. Another research also summarized this conclusion (Gittens, McLachlan et al. 2011). The amount of hMSCs on PCL nanofiber did not increase by treating more strontium on 1 and 7 days; at day 14, significant higher cell amount was observed on PCL/SrC20 (240 ppm) than on PCL/SrC10 (120 ppm) (Meka, Jain et al. 2016). Thus, a continuous exposure (over 7 days) to certain amount of strontium is important for osteoblast-like cell proliferation in vitro. Another interesting finding from Figure 43 was the amounts of cells on NF and NF with Sr^{2+} was lower than the control groups (100%). We thought ions of medium might be slightly alternated followed by NFs degradation. It was not toxic to cell, but might affect its growth. The effect of Sr^{2+} on osteogenic differentiation was evaluated by AKP assay (Figure 45). The AKP enzyme activity was vary under the influence of different Sr^{2+} concentration. In eluent-1, eluent-2 and eluent-3 groups, the AKP enzyme activities of strontium positive group was

higher than both control (100%) and negative control group, in which a maximum was found in eluent-1 group (Figure 44). Lower strontium concentration treatments were found slightly stimulating effect on pre-osteoblasts cell differentiation. Our results were in agreement with several related researches. M. Schumacher *et al.* found the optimal strontium concentration on hMSCs osteogenic differentiation was 0.1mM(Schumacher, Lode et al. 2013); Braux *et al.* found a maximum osteogenic marker expression on primary human osteoblast cells under 0.05mM (4 μg/ml) Sr^{2+} treatments (Braux, Velard et al. 2011). However, other studies found osteoblast-like cells could be differentiated better if treated by higher Sr^{2+} concentration, such as 2mM (Barbara, Delannoy et al. 2004, Yang, Yang et al. 2011) and 1mM (Barbara, Delannoy et al. 2004). Overall, the differentiation of osteoblast cells is sensitive to the concentration of Sr^{2+}. The optimal Sr^{2+} concentration is vary to different cell and to different release materials.

The last step of this study was cellular response in direct contact with NFs. It is different from the indirect contact study by culturing cells in the presence of culture medium eluent. By culturing cells directly on the NF matrix, the cell response was affected by both the NFs microstructure and the chemical components of NFs. In addition, the Sr^{2+} released from NFs was accumulated until the replacement of cell medium. On 3 days, the cell amount on Sr^{2+} doped NFs was significantly higher than the amount on NFs ($p<0.05$) (Figure 45A); on 7 day, the cell amount on Sr^{2+} doped NFs was still higher and close to control, but was not significant (Figure 45B). Based on Sr^{2+} release curve, the accumulated

Sr^{2+} concentration within 3 days (~80 μg/ml) should be much higher than 3 to 7 days (~10 μg/ml). The higher strontium concentration (within positive influence range) could better stimulate cell proliferation. In 7day culture group (Figure 45B), the strontium concentration for cell treatment was not constant, especially in the second period (3-7 day after changing medium) the strontium concentration was not high enough to keep high proliferation. Moreover, the looser structure of Sr^{2+} doped NFs could help the cell proliferation as well (Chapter 2). Combined these factors may explain the results of Figure 46. Like the in direct contact study, the cell amount on NFs groups was lower than the control group on 3 day. As mentioned above, the degradation products as well as pH change might reduce the cell proliferation. In addition, limited by method of Picogreen assay probably cell lysate was incomplete on NFs groups, and some DNAs were still trapped inside the nanofiber matrixes. This also resulted in lower DNA concentration tested on NF groups. The cell proliferation on Sr^{2+} doped NFs was significantly higher than other groups. We believed positive effect of Sr2+ and looser structure of the NFs assisted the cell differentiation.

In conclusion, the coaxial 3D Sr^{2+} doped PCL/PLGA (1:1)-PVA NFs could sustain release strontium over 2 months. The released strontium had positive effect on pre-osteoblast cell differentiation. For proliferation, the stimulating effect may be more obvious with higher and longer strontium concentration treatment. In future, the system should be adjusted to reach a strontium release with longer time and higher concentration, especially in the later period. To realize this, on one hand we could increase the strontium amount in NFs; on the other hand, we

could choose different types of strontium source to remain a complete sheath structure during the initial period of degradation, such as $SrCO_3$ nanoparticles (Meka, Jain et al. 2016). Further studies, such as application NFs on Ti implant, in vivo test of toxicity, cell adhesion; proliferation and differentiation of the strontium doped NFs and investigation of the osseointegration capability of the coaxial NFs coated Ti implant via previous established rat tibia impact model are necessary to evaluate these nanofibers.

CHAPTER 5 CONCLUSION AND FUTURE WORKS

Nanofiber (NF) is a promising material for orthopedic implant coating to enhance osseointegration as it mimics the nanofibrous collagen network of bone cell extracellular environment. Recently we reported that Ti implant fabricated with Dox doped coaxial PCL/PVA NFs coating significantly enhanced the new bone formation at the bone-implant surface and considerably inhibited the bacterial growth up to 8 weeks after implantation using a rat tibia implantation model. We believe that the implant with a NF coating has a great potential for the enhancement of implant early osseointegration. We propose that a coaxial NFs can be used a periprosthetic delivery tool of different drugs. However, the limitations of previous implant NF coating matrix include the lack of desired 3D structure, and the slower degradation rate that did not match to the osseointegration physiology in vivo (~one month). In the thesis, we aimed to develop 3D coaxial NFs as implant coating to further improve the efficiency of early osseointegration. We have developed and defined an optimal formula of coaxial PCL-PLGA/PVA NFs with desired microstructure (pore size, pore volume and interconnectivity) and physiochemical properties (surface rough ness, mechanical strength, and faster in vitro degradation rate). In addition the in vitro osteogenic cell behavior (adhesion, proliferation and differentiation) has been extensively investigated using a pre-osteoblastic MC3T3 cell line.

Firstly, as described in Chapter 2, we have developed an automatic 3D nanofibers collector. Based on the coronal charge effect and multi-stacking principle, the 3D PCL NFs were formed during electrospinning process. In

addition, we were able to alter the properties of 3D NFs through collector movement. The PCL NFs thickness, surface roughness, pore size/volume and porosity were proportional and gradient increased due to the increase of the collector movement velocity. We observed that the stiffness of single nanofibers was increased due to the increased rate of the collector movement because a higher crystallinity rate is formed during electrospinng. This technique overcame the drawback of electrospinning, which used to fabricate dense and flat membrane, and broaden the application of electrospun NFs for the tissue engineering application.

Secondly, we chose three types of cells related to bone formation, including pre-osteoblast cell (MC3T3-E1), pre-osteoclast cells (RAW) and stem cells (ASCs). We were interested in the cells behaviors on four types of NFs with different physiochemical properties. We further defined the optimal moving speed for coaxial NFs fabrication based on cellular study. The cells were very sensitive to the different living environments. The MC3T3-E1 and ASCs performed significantly higher proliferation on NF-high than other NFs ($p<0.05$); and the MC3T3-E1 differentiated level was also higher on NF-high because looser structure and higher material stiffness helped cell attachment and nutrition exchange. However, the RAW cells prefer the growth on the NFs with relatively dense structure (smaller pore size and porosity). We propose that the RAW cells have much smaller size volume as compared to RAW cells and ASCs. Therefore, RAW cells lack enough contacts with surrounding NFs matrix if they were grown on a NF matrix with larger space and pore sizes. We selected 3D NF matrix with

the large pore size and porosity (NFs-high) as the optimal formula for implant coating matrix based on the following considerations:

- The pre-osteoblasts, bone-forming cells, performed the best proliferation and differentiation on the NFs with larger pores (NFs-high).
- The stem cells (present in the bone marrow) are the main cells that will interact with implant surface coatings. We observed that stem cells showed the highest activity when cultured on the NFs with larger pores (NFs-high).
- However, the pre-osteoclasts (RAW cells) are less inactive when cultured on the NFs with larger pores (NFs-high) than that in denser NFs matrix.

Taken together, we propose this new implant surface 3D NF coating matrix will provide an extracellular environment that will stimulate bone forming cells growing in while slowing down the activities of pre-osteoclasts.

Thirdly, in the last chapter, we imported PLGA to the PCL/PVA coaxial system to accelerate degradation rate; and developed strontium doped coaxial 3D PCL/PLGA (1:1)-PVA nanofibers. The coaxial NFs enabled to control strontium release time. The Sr^{2+} was released from coaxial NFs over 2 month and the concentration was relatively constant. The released Sr^{2+} especially at higher concentrations had positive effects on the proliferation and differentiation of MC3T3-E1 by using indirect contact study approach. In the direct contact study, the strontium doped coaxial 3D NFs benefited MC3T3-E1 differentiation because of Sr^{2+} effect and the looser NF structure.

We believe these coaxial NFs had great potential as the implant coating. It has ideal microstructure and good mechanical properties for pre-osteoblasts and stem cells growth; meantime it is not desired for pre-osteoclasts proliferation and differentiation. Additionally, it is a controllable drug release system. It successfully released Sr^{2+} over 2 month with relatively constant concentration. Thus it should be promising release system for peptides, proteins, and antibiotics release. In the next step, we will develop a rotating device that provides a real time of 3D NF coating during electrospinning process. The 3D NFs will directly deposit on the titanium (Ti) pins without disturbing its microstructures. The direct deposit also increases bonding strength of NFs and underline Ti surface. We will test the cellular behaviors of other cells such as bone marrow stromal stem cells and endothelia cells that are closely involved in the process of implant osseointegration. Finally, the therapeutic efficacies of implant surface 3D NF coating (with and without drug embedding) will be evaluated in our established rat model of tibia implantation.

REFERENCES

A. Cipitria, A. S., T. R. Dargaville, et al. (2011). "Design, fabrication and characterization of PCL electrospun scaffolds—a review." Journal of Materials Chemistry **21**: 9419-9453.

A. Cipitria, A. S., T. R. Dargaville, P. D. Dalton and D. W. Hutmacher (2011). "Design, fabrication and characterization of PCL electrospun scaffolds—a review." Journal of Materials Chemistry(26): 9419.

Abdal-hay, A., M.-G. Hwang and J. K. Lim (2012). "In vitro bioactivity of titanium implants coated with bicomponent hybrid biodegradable polymers." Journal of sol-gel science and technology **64**(3): 756-764.

Ameer Al-Shawk, Liang Chen, et al. (2015). “Topological Characterization of Nano Fiber Coating Layer on Implant Surfaces.” Materials Research Society (MRS) Conference.

Ameer Al-Shawk, to appear in PhD dissertation “ Surface Topology in Manufacturing Processes”, Wayne State University, 2019.

Anagnostakos, K., O. Furst and J. Kelm (2006). "Antibiotic-impregnated PMMA hip spacers: Current status." Acta Orthop **77**(4): 628-637.

Andrea Di Luca, B. O., Ivan Lorenzo-Moldero, Antonio Lepedda, Wojcech Swieszkowski, Clemens Van Blitterswijk and Lorenzo Moroni (2016). "Gradients in pore size enhance the osteogenic differentiation of human mesenchymal stromal cells in three-dimensional scaffolds." Nature **6**: 2289.

Aro, H. T., J. J. Alm, N. Moritz, T. J. Makinen and P. Lankinen (2012). "Low BMD affects initial stability and delays stem osseointegration in cementless total hip

arthroplasty in women: a 2-year RSA study of 39 patients." Acta Orthop **83**(2): 107-114.

Badami AS, K. M., Thompson MS, Riffle JS, Goldstein AS (2006). "Effect of fiber diameter on spreading, proliferation, and differentiation of osteoblastic cells on electrospun poly(lactic acid) substrates." Biomaterials **27**(4): 596-606.

Bahraminasab, M., Sahari, B.B., Edwards, K. L.,Farahmand, F., Arumugam, M., Hong,T.S. (2012). "Aseptic loosening of femoral components – A review of current and future trends in materials used." Materials & Design **42**: 459-470.

Baker BM, G. A., Metter RB, Nathan AS, Marklein RA, Burdick JA, Mauck RL. (2008). "The potential to improve cell infiltration in composite fiber-aligned electrospun scaffolds by the selective removal of sacrificial fibers." Biomaterials **29**(15): 2348-2358.

Baker, B. M., A. M. Handorf, L. C. Ionescu, W. J. Li and R. L. Mauck (2009). "New directions in nanofibrous scaffolds for soft tissue engineering and regeneration." Expert Rev Med Devices **6**(5): 515-532.

Ball SG, S. C., Kielty CM (2007). "Vascular endothelial growth factor can signal through platelet-derived growth factor receptors." J Cell Biol. **177**(3): 489-500.

Barbara, A., P. Delannoy, B. Denis and P. Marie (2004). "Normal matrix mineralization induced by strontium ranelate in MC3T3-E1 osteogenic cells." Metabolism **53**(4): 532-537.

Baroli, B. (2009). "From natural bone grafts to tissue engineering therapeutics: Brainstorming on pharmaceutical formulative requirements and challenges." J Pharm Sci **98**(4): 1317-1375.

Barthes J, Ö. H., Hindié M, Ndreu-Halili A, Hasan A, Vrana NE (2014). "Cell microenvironment engineering and monitoring for tissue engineering and regenerative medicine: the recent advances." Biomed Res Int **2014**.

Barthes, J., H. Ozcelik, M. Hindie, A. Ndreu-Halili, A. Hasan and N. E. Vrana (2014). "Cell microenvironment engineering and monitoring for tissue engineering and regenerative medicine: the recent advances." Biomed Res Int **2014**: 921905.

Berry, D. J., W. S. Harmsen, M. E. Cabanela and B. F. Morrey (2002). "Twentyfive-year survivorship of two thousand consecutive primary Charnley total hip replacements: factors affecting survivorship of acetabular and femoral components." J Bone Joint Surg Am **84-A**(2): 171-177.

Bishop, J. A., A. A. Palanca, M. J. Bellino and D. W. Lowenberg (2012). "Assessment of compromised fracture healing." J Am Acad Orthop Surg **20**(5): 273-282.

Blakeney BA, T. A., Anderson JM, Andukuri A, Lim DJ, Dean DR, Jun (2011). "Cell infiltration and growth in a low density, uncompressed three-dimensional electrospun nanofibrous scaffold." Biomaterials **32**(6): 1583-1590.

Boos, C., K. Fink, P. Stomberg, W. Koeller, B. W. Igl and M. Russlies (2008). "[The influence of bone quality and the fixation procedure on the primary stability of cementless implanted tibial plateaus]." Biomed Tech (Berl) **53**(2): 70-76.

Bozic, K. J., S. M. Kurtz, E. Lau, K. Ong, T. P. Vail and D. J. Berry (2009). "The epidemiology of revision total hip arthroplasty in the United States." JBJS **91**(1): 128-133.

Brandi, M. L. and P. Collin-Osdoby (2006). "Vascular biology and the skeleton." J Bone Miner Res **21**(2): 183-192.

Braux, J., F. Velard, C. Guillaume, S. Bouthors, E. Jallot, J.-M. Nedelec, D. Laurent-Maquin and P. Laquerrière (2011). "A new insight into the dissociating effect of strontium on bone resorption and formation." Acta biomaterialia **7**(6): 2593-2603.

Brennan, T. C., M. S. Rybchyn, W. Green, S. Atwa, A. D. Conigrave and R. S. Mason (2009). "Osteoblasts play key roles in the mechanisms of action of strontium ranelate." British journal of pharmacology **157**(7): 1291-1300.

Bullough, P. G., E. F. DiCarlo, K. K. Hansraj and M. C. Neves (1988). "Pathologic studies of total joint replacement." Orthop Clin North Am **19**(3): 611-625.

C.T. Lim, E. P. S. T., and S.Y.Ng (2008). "Effects of crystalline morphology on the tensile properties of electrospun polymer nanofibers." Appl. Phys. Lett. **92**(14): 14908.

Caverzasio, J. (2008). "Strontium ranelate promotes osteoblastic cell replication through at least two different mechanisms." Bone **42**(6): 1131-1136.

Chen L, S. W., Markel DC, Shi T, Muzik O, Matthew H, Ren W (2016). "Flow perfusion culture of MC3T3-E1 osteogenic cells on gradient calcium polyphosphate scaffolds with different pore sizes." J Biomater Appl. **30**(7): 908918.

Crouch AS, M. D., Luebke KJ, Hu W (2009). "Correlation of anisotropic cell behaviors with topographic aspect ratio." Biomaterials **30**(8): 1560-1567.

Dawes, G., L. Fratila-Apachitei, B. Necula, I. Apachitei, G. Witkamp and J. Duszczyk (2010). "Release of PLGA–encapsulated dexamethasone from microsphere loaded porous surfaces." Journal of Materials Science: Materials in Medicine **21**(1): 215-221.

de Jonge, L. T., S. C. Leeuwenburgh, J. G. Wolke and J. A. Jansen (2008). "Organic-inorganic surface modifications for titanium implant surfaces." Pharm Res **25**(10): 2357-2369.

Doshi J, R. D. (1995). "Electrospinning process and applications of electrospun fibers." J Electrost **35**: 151-160.

Dupont, K. M., J. D. Boerckel, H. Y. Stevens, T. Diab, Y. M. Kolambkar, M. Takahata, E. M. Schwarz and R. E. Guldberg (2012). "Synthetic scaffold coating with adeno-associated virus encoding BMP2 to promote endogenous bone repair." Cell Tissue Res **347**(3): 575-588.

Erica Palin, H. L. a. T. J. W. (2005). "Mimicking the nanofeatures of bone increases bone-forming cell adhesion and proliferation." Nanotechnology **16**(9): 1828-1835.

Ferrara, N., H. P. Gerber and J. LeCouter (2003). "The biology of VEGF and its receptors." Nat Med **9**(6): 669-676.

Fratzl P1, G. M., Vogl G (1992). "Mineral crystals in calcified tissues: a comparative study by SAXS." J Bone Miner Res **7**(3): 329-334.

Fratzl P, G. M., Vogl G, Plenk H Jr, Eschberger J, Fratzl-Zelman N, Koller K, Klaushofer K (1992). "Mineral crystals in calcified tissues: a comparative study by SAXS." J Bone Miner Res **7**(3): 329-334.

Fu, S. Z., X. H. Meng, J. Fan, L. L. Yang, S. Lin, Q. L. Wen, B. Q. Wang, L. L. Chen, J. B. Wu and Y. Chen (2014). "In vitro and in vivo degradation behavior of n-HA/PCL-Pluronic-PCL polyurethane composites." Journal of Biomedical Materials Research Part A **102**(2): 479-486.

G.Kister, G. C., M.Bergounhon, D.Hoarau, M.Vert (2000). "Structural characterization and hydrolytic degradation of solid copolymers of d,l-lactide-coε-caprolactone by Raman spectroscopy." Polymer **41**(3): 925-932.

Geesink RG, d. G. K., Klein CP. (1987). "Chemical implant fixation using hydroxyl-apatite coatings. The development of a human total hip prosthesis for chemical fixation to bone using hydroxyl-apatite coatings on titanium substrates." Clin Orthop Relat Res **225**: 147-170.

Gittens, R. A., T. McLachlan, R. Olivares-Navarrete, Y. Cai, S. Berner, R. Tannenbaum, Z. Schwartz, K. H. Sandhage and B. D. Boyan (2011). "The effects of combined micron-/submicron-scale surface roughness and nanoscale features on cell proliferation and differentiation." Biomaterials **32**(13): 3395-3403.

Gittens RA, M. T., Olivares-Navarrete R, Cai Y, Berner S, Tannenbaum R,

Schwartz Z, Sandhage KH, Boyan BD (2011). "The effects of combined micron/submicron-scale surface roughness and nanoscale features on cell proliferation and differentiation." Biomaterials **32**(13): 3395-3403.

Glawe JD, H. J., Mills DK, McShane MJ (2005). "Influence of channel width on alignment of smooth muscle cells by high-aspect-ratio microfabricated elastomeric cell culture scaffolds." J Biomed Mater Res **75**(1): 106-114.

Gluck, J. M., P. Rahgozar, N. P. Ingle, F. Rofail, A. Petrosian, M. G. Cline, M. C. Jordan, K. P. Roos, W. R. MacLellan and R. J. Shemin (2011). "Hybrid coaxial electrospun nanofibrous scaffolds with limited immunological response created for tissue engineering." Journal of Biomedical Materials Research Part B: Applied Biomaterials **99**(1): 180-190.

Golub, J. S., Y. T. Kim, C. L. Duvall, R. V. Bellamkonda, D. Gupta, A. S. Lin, D. Weiss, W. Robert Taylor and R. E. Guldberg (2010). "Sustained VEGF delivery via PLGA nanoparticles promotes vascular growth." Am J Physiol Heart Circ Physiol **298**(6): H1959-1965.

Gomes, M. E., H. L. Holtorf, R. L. Reis and A. G. Mikos (2006). "Influence of the porosity of starch-based fiber mesh scaffolds on the proliferation and osteogenic differentiation of bone marrow stromal cells cultured in a flow perfusion bioreactor." Tissue Eng **12**(4): 801-809.

Goodman, S. B., Z. Yao, M. Keeney and F. Yang (2013). "The future of biologic coatings for orthopaedic implants." Biomaterials **34**(13): 3174-3183.

Goodrich JT, S. A., Tepper O (2012). "A review of reconstructive materials for use in craniofacial surgery bone fixation materials, bone substitutes, and distractors." Childs Nerv Syst **28**(9): 1577-1588.

Goosen JH, K. A., Kollen BJ, Verheyen CC. (2008). "Porous-coated femoral components with or without hydroxyapatite in primary uncemented total hip arthroplasty: a systematic review of randomized controlled trials." Arch Orthop Trauma Surg **129**(9): 1165-1169.

Haboush, E. J. (1996). "A new operation for arthroplasty of the hip based on biomechanics, photoelasticity, fast-setting dental acrylic, and other considerations. 1953 [classicle article]." Bull Hosp Jt Dis **55**(2): 95-111.

Ho ST, H. D. (2006). "A comparison of micro CT with other techniques used in the characterization of scaffolds." Biomaterials **27**(8): 1362-1376.

Holtorf, H. L., N. Datta, J. A. Jansen and A. G. Mikos (2005). "Scaffold mesh size affects the osteoblastic differentiation of seeded marrow stromal cells cultured in a flow perfusion bioreactor." J Biomed Mater Res A **74**(2): 171-180.

Holzwarth, J. M. and P. X. Ma (2011). "Biomimetic nanofibrous scaffolds for bone tissue engineering." Biomaterials **32**(36): 9622-9629.

Howie, D. W., D. R. Haynes, S. D. Rogers, M. A. McGee and M. J. Pearcy (1993). "The response to particulate debris." Orthop Clin North Am **24**(4): 571581.

Huang, Z., R. H. Daniels, R.-J. Enzerink, V. Hardev, V. Sahi and S. B. Goodman (2008). "Effect of nanofiber-coated surfaces on the proliferation and differentiation of osteoprogenitors in vitro." Tissue Engineering Part A **14**(11): 1853-1859.

Huang, Z., R. H. Daniels, R. J. Enzerink, V. Hardev, V. Sahi and S. B. Goodman (2008). "Effect of nanofiber-coated surfaces on the proliferation and differentiation of osteoprogenitors in vitro." Tissue Eng Part A **14**(11): 1853-1859.

Ifkovits, J. L., H. G. Sundararaghavan and J. A. Burdick (2009). "Electrospinning fibrous polymer scaffolds for tissue engineering and cell culture." J Vis Exp(32).

Ifkovits, J. L., H. G. Sundararaghavan and J. A. Burdick (2009). "Electrospinning fibrous polymer scaffolds for tissue engineering and cell culture." Journal of visualized experiments: JoVE(32).

Jang, J.-H., O. Castano and H.-W. Kim (2009). "Electrospun materials as potential platforms for bone tissue engineering." Advanced drug delivery reviews **61**(12): 1065-1083.

Jang JH, C. O., Kim HW. (2009). "Electrospun materials as potential platforms for bone tissue engineering." Adv Drug Deliv Rev **61**(12): 1065-1083.

K Fujihara A Kumar, R. J., S Ramakrishna and S Uchida (2007). "Spray deposition of electrospun TiO2 nanorods for dye-sensitized solar cell." Nanotechnology **18**: 165604.

Karageorgiou, V. and D. Kaplan (2005). "Porosity of 3D biomaterial scaffolds and osteogenesis." Biomaterials **26**(27): 5474-5491.

Karageorgiou V, K. D. (2005). "Porosity of 3D biomaterial scaffolds and osteogenesis." Biomaterials **26**(27): 5474-5491.

Kärrholm J, B. B., Löwenhielm G, Snorrason F. (1994). "Does early micromotion of femoral stem prostheses matter? 4-7-year stereoradiographic follow-up of 84 cemented prostheses." J Bone Jiont Surg Br. **76**(6): 912-917.

Karrholm, J., B. Borssen, G. Lowenhielm and F. Snorrason (1994). "Does early micromotion of femoral stem prostheses matter? 4-7-year stereoradiographic follow-up of 84 cemented prostheses." Bone & Joint Journal **76**(6): 912-917.

Katti, D. S., K. W. Robinson, F. K. Ko and C. T. Laurencin (2004). "Bioresorbable nanofiber-based systems for wound healing and drug delivery: optimization of fabrication parameters." J Biomed Mater Res B Appl Biomater **70**(2): 286-296.

Ki C S, K. J. W., Hyun J H,Lee K H,Hattori M,Rah D Kand Park Y H (2007). "Electrospun three-dimensional silk fibroin nanofibrous scaffold." J. Appl. Polym. Sci. **106**: 3922.

Kim, H.-W., Y.-H. Koh, Y.-M. Kong, J.-G. Kang and H.-E. Kim (2004). "Strontium substituted calcium phosphate biphasic ceramics obtained by a powder precipitation method." Journal of Materials Science: Materials in Medicine **15**(10): 1129-1134.

Kohgo, T., Y. Yamada, K. Ito, A. Yajima, R. Yoshimi, K. Okabe, S. Baba and M. Ueda (2011). "Bone regeneration with self-assembling peptide nanofiber scaffolds in tissue engineering for osseointegration of dental implants." International Journal of Periodontics & Restorative Dentistry **31**(4).

Kohgo, T., Y. Yamada, K. Ito, A. Yajima, R. Yoshimi, K. Okabe, S. Baba and M. Ueda (2011). "Bone regeneration with self-assembling peptide nanofiber scaffolds in tissue engineering for osseointegration of dental implants." Int J Periodontics Restorative Dent **31**(4): e9-16.

Kroell, A., P. Beaule, M. Krismer, H. Behensky, B. Stoeckl and R. Biedermann (2009). "Aseptic stem loosening in primary THA: migration analysis of cemented and cementless fixation." Int Orthop **33**(6): 1501-1505.

Kurtz, S. M., K. L. Ong, E. Lau, K. J. Bozic, D. Berry and J. Parvizi (2010). "Prosthetic joint infection risk after TKA in the Medicare population." Clinical Orthopaedics and Related Research® **468**(1): 52-56.

Lee, H., D. Lie, K. Lim, T. Thirumoorthy and S. Pang (2009). "Strontium ranelateinduced toxic epidermal necrolysis in a patient with post-menopausal osteoporosis." Osteoporosis International **20**(1): 161-162.

Lee, K. and S. B. Goodman (2008). "Current state and future of joint replacements in the hip and knee." Expert review of medical devices **5**(3): 383393.

Lennox, D. W., B. H. Schofield, D. F. McDonald and L. H. Riley, Jr. (1987). "A histologic comparison of aseptic loosening of cemented, press-fit, and biologic ingrowth prostheses." Clin Orthop Relat Res(225): 171-191.

Leong, M. F., M. Z. Rasheed, T. C. Lim and K. S. Chian (2009). "In vitro cell infiltration and in vivo cell infiltration and vascularization in a fibrous, highly porous poly(D,L-lactide) scaffold fabricated by cryogenic electrospinning technique." J Biomed Mater Res A **91**(1): 231-240.

Li, C., C. Vepari, H.-J. Jin, H. J. Kim and D. L. Kaplan (2006). "Electrospun silkBMP-2 scaffolds for bone tissue engineering." Biomaterials **27**(16): 3115-3124.

Li, D., G. Ouyang, J. T. McCann and Y. Xia (2005). "Collecting electrospun nanofibers with patterned electrodes." Nano Lett **5**(5): 913-916.

Li D, W. Y., Xia Y (2004). "Nanofibers as Uniaxially Aligned Arrays and Layer-byLayer Stacked Films." Nano Lett **3**: 1167-1171.

Li WJ, L. C., Caterson EJ, Tuan RS, Ko FK (2001). "Electrospun nanofibrous structure: a novel scaffold for tissue engineering." J Biomed Mater Res. **60**(4): 613-621.

Li WJ, L. C., Caterson EJ, Tuan RS, Ko FK. (2002). "Electrospun nanofibrous structure: a novel scaffold for tissue engineering." J Biomed Mater Res **60**(3): 613-621.

Lopez-Hallman, R. J. (2013). "Electrospinning of nanofibers solutions with PVDF, DMF, acetone and Fe3O4 nanoparticles." 2013 NCUR.

Lowery, J. L., N. Datta and G. C. Rutledge (2010). "Effect of fiber diameter, pore size and seeding method on growth of human dermal fibroblasts in electrospun poly(epsilon-caprolactone) fibrous mats." Biomaterials **31**(3): 491-504.

Lowery JL, D. N., Rutledge GC. (2010). "Effect of fiber diameter, pore size and seeding method on growth of human dermal fibroblasts in electrospun poly(epsilon-caprolactone) fibrous mats." Biomaterials **31**(3): 491-504.

Lu, L., S. J. Peter, M. D. Lyman, H.-L. Lai, S. M. Leite, J. A. Tamada, S. Uyama, J. P. Vacanti, R. Langer and A. G. Mikos (2000). "In vitro and in vivo degradation of porous poly (DL-lactic-co-glycolic acid) foams." Biomaterials **21**(18): 18371845.

Ma, J. M. H. a. P. X. (2011). "3D nanofibrous scaffolds for tissue engineering." J Materials Chemistry **21**: 10243-10251.

Makadia, H. K. and S. J. Siegel (2011). "Poly lactic-co-glycolic acid (PLGA) as biodegradable controlled drug delivery carrier." Polymers **3**(3): 1377-1397.

Marelli B, A. A., Farè S, Freddi G, Mantovani D, Tanzi MC. (2010). "Compliant electrospun silk fibroin tubes for small vessel bypass grafting." Acta Biomater **6**(10): 4019-4026.

Marie, P. (2003). "Optimizing bone metabolism in osteoporosis: insight into the pharmacologic profile of strontium ranelate." Osteoporosis international **14**(3): 912.

Meka, S. R. K., S. Jain and K. Chatterjee (2016). "Strontium eluting nanofibers augment stem cell osteogenesis for bone tissue regeneration." Colloids and Surfaces B: Biointerfaces **146**: 649-656.

Mendonça G, M. D., Aragão FJ, Cooper LF (2010). "The combination of micron and nanotopography by H(2)SO(4)/H(2)O(2) treatment and its effects on osteoblast-specific gene expression of hMSCs." J Biomed Mater Res A **94**(1): 169-179.

Meunier, P., C. Roux, S. Ortolani, M. Diaz-Curiel, J. Compston, P. Marquis, C. Cormier, G. Isaia, J. Badurski and J. Wark (2009). "Effects of long-term strontium ranelate treatment on vertebral fracture risk in postmenopausal women with osteoporosis." Osteoporosis international **20**(10): 1663-1673.

Miyamoto, K., M. Atarashi, H. Kadozono, M. Shibata, Y. Koyama, M. Okai, A. Inakuma, E. Kitazono, H. Kaneko, T. Takebayashi and T. Horiuchi (2009). "Creation of cross-linked electrospun isotypic-elastin fibers controlled celldifferentiation with new cross-linker." Int J Biol Macromol **45**(1): 33-41.

Morohashi, T., T. Sano and S. Yamada (1994). "Effects of strontium on calcium metabolism in rats i. a distinction between the pharmacological and toxic doses." The Japanese Journal of Pharmacology **64**(3): 155-162.

Mygind, T., M. Stiehler, A. Baatrup, H. Li, X. Zou, A. Flyvbjerg, M. Kassem and C. Bunger (2007). "Mesenchymal stem cell ingrowth and differentiation on coralline hydroxyapatite scaffolds." Biomaterials **28**(6): 1036-1047.

Nam, J., Y. Huang, S. Agarwal and J. Lannutti (2007). "Improved cellular infiltration in electrospun fiber via engineered porosity." Tissue Eng **13**(9): 22492257.

Nielsen, S. P. (2004). "The biological role of strontium." Bone **35**(3): 583-588.

Ogawa, T., L. Saruwatari, K. Takeuchi, H. Aita and N. Ohno (2008). "Ti nanonodular structuring for bone integration and regeneration." Journal of dental research **87**(8): 751-756.

PaolaTaddei, A., MatteoReggiani, ConcezioFagnano (2005). "In vitro mineralization of bioresorbable poly(ε-caprolactone)/apatite composites for bone tissue engineering: a vibrational and thermal investigation." J Molecular Structure **744-747**: 135-143.

Pham, Q. P., U. Sharma and A. G. Mikos (2006). "Electrospun poly(epsiloncaprolactone) microfiber and multilayer nanofiber/microfiber scaffolds: characterization of scaffolds and measurement of cellular infiltration." Biomacromolecules **7**(10): 2796-2805.

Pi, M. and L. D. Quarles (2004). "A Novel Cation-Sensing Mechanism in Osteoblasts Is a Molecular Target for Strontium." Journal of Bone and Mineral Research **19**(5): 862-869.

Pramanik, N., D. Mishra, I. Banerjee, T. K. Maiti, P. Bhargava and P. Pramanik (2009). "Chemical synthesis, characterization, and biocompatibility study of hydroxyapatite/chitosan phosphate nanocomposite for bone tissue engineering applications." Int J Biomater **2009**: 512417.

Pulido, L., E. Ghanem, A. Joshi, J. J. Purtill and J. Parvizi (2008). "Periprosthetic joint infection: the incidence, timing, and predisposing factors." Clinical orthopaedics and related research **466**(7): 1710-1715.

Ramaseshan R, S. S., Liu YJ, Barhate RS, Lala NL, Ramakrishna S. (2006). "Functionalized polymer nanofibre membranes for protection from chemical warfare stimulants." Nanotechnology **17**(12): 2947.

Rammelt, S., E. Schulze, R. Bernhardt, U. Hanisch, D. Scharnweber, H. Worch, H. Zwipp and A. Biewener (2004). "Coating of titanium implants with type-I collagen." J Orthop Res **22**(5): 1025-1034.

Rampichová M, C. J., Buzgo M, Prosecká E, Mikeš P, Vysloužilová L, Tvrdík D, Kochová P, Gregor T, Lukáš D, Amler E. (2013). "Elastic three-dimensional poly (ε-caprolactone) nanofibre scaffold enhances migration, proliferation and osteogenic differentiation of mesenchymal stem cells." Cell Prolif **46**(1): 23-37.

Reginster, J.-Y., E. Seeman, M. De Vernejoul, S. Adami, J. Compston, C. Phenekos, J.-P. Devogelaer, M. D. Curiel, A. Sawicki and S. Goemaere (2005). "Strontium ranelate reduces the risk of nonvertebral fractures in postmenopausal

women with osteoporosis: Treatment of Peripheral Osteoporosis (TROPOS) study." The journal of clinical endocrinology & metabolism **90**(5): 2816-2822.

Ren, W., X. H. Li, B. D. Chen and P. H. Wooley (2004). "Erythromycin inhibits wear debris-induced osteoclastogenesis by modulation of murine macrophage NF-kappaB activity." J Orthop Res **22**(1): 21-29.

Ren, W., R. Zhang, M. Hawkins, T. Shi and D. C. Markel (2010). "Efficacy of periprosthetic erythromycin delivery for wear debris-induced inflammation and osteolysis." Inflamm Res **59**(12): 1091-1097.

Reneker DH, C. I. (1996). "Nanometre diameter fibres of polymer, produced by electrospinning." Nanotechnology **7**: 216-223.

Renwen Zhang, D. X., Tracy L., Carol T. (2004). "Ectopic bone formation using osteogenic protein-1 carried by a solution precipitated hydroxyapatite." J Biomed Mater Res **71A**(3): 412-418.

Røhl L, L. E., Linde F, Odgaard A, Jørgensen J. (1991). "Tensile and compressive properties of cancellous bone." J Biomech. **24**(21): 1143-1149.

Rosenzweig, D. H., S. Solar-Cafaggi and T. M. Quinn (2012). "Functionalization of dynamic culture surfaces with a cartilage extracellular matrix extract enhances chondrocyte phenotype against dedifferentiation." Acta biomaterialia **8**(9): 33333341.

Ryd, L. (1992). "Roentgen stereophotogrammetric analysis of prosthetic fixation in the hip and knee joint." Clin Orthop Relat Res(276): 56-65.

S Weiner, H. W., S Weiner, HD Wagner, S Weiner, H Wagner, Anthony D. Wagner, H.D. Wagner, Peter Wagner, S Weiner, Paul D. Wagner, H.J. Wagner

(1998). "The Material Bone: Structural-Mechanical Function Relations." Annu. Rev. Mater. Sci **28**.

Saran, U., S. Gemini Piperni and S. Chatterjee (2014). "Role of angiogenesis in bone repair." Arch Biochem Biophys **561**: 109-117.

Sartori, M., G. Giavaresi, A. Parrilli, A. Ferrari, N. N. Aldini, M. Morra, C. Cassinelli, D. Bollati and M. Fini (2015). "Collagen type I coating stimulates bone regeneration and osteointegration of titanium implants in the osteopenic rat." Int Orthop **39**(10): 2041-2052.

Schneider O D, W. F., Brunner T J, Loher S, Ehrbar M, Schmidlin P R and Stark W J (2009). "In vivo and in vitro evaluation of flexible, cottonwool-like nanocomposites as bone substitute material for complex defects." Acta Biomater. **5**(5): 1775-1784.

Schofer MD, F.-W. S., Gräbedünkel C, Wack C, Dersch R, Rudisile M, Wendorff JH, Greiner A, Paletta JR, Boudriot U (2008). "Influence of poly(L-lactic acid) nanofibers and BMP-2-containing poly(L-lactic acid) nanofibers on growth and osteogenic differentiation of human mesenchymal stem cells." ScientificWorldJournal **8**: 1269-1279.

Schumacher, M., A. Lode, A. Helth and M. Gelinsky (2013). "A novel strontium (II)-modified calcium phosphate bone cement stimulates human-bone-marrowderived mesenchymal stem cell proliferation and osteogenic differentiation in vitro." Acta biomaterialia **9**(12): 9547-9557.

Shah, N. J., J. Hong, M. N. Hyder and P. T. Hammond (2012). "Osteophilic multilayer coatings for accelerated bone tissue growth." Adv Mater **24**(11): 14451450.

Shim, I. K., W. H. Suh, S. Y. Lee, S. H. Lee, S. J. Heo, M. C. Lee and S. J. Lee (2009). "Chitosan nano-/microfibrous double-layered membrane with rolled-up three-dimensional structures for chondrocyte cultivation." J Biomed Mater Res A **90**(2): 595-602.

Shing-Chung Wong, A. B., Siwei Leng (2008). "Effect of fiber diameter on tensile properties of electrospun poly(ε-caprolactone)." Polymer **49**(21): 4713-4722.

Skotak, M. R., J.; Gonzalez, D.; Subramanian (2011). "Improved cellular infiltration into nanofibrous electrospun cross-linked gelatin scaffolds templated with micrometer-sized polyethylene glycol fibers." Biomedical Materials **6**(5).

Smit, E. B., U.; Sanderson, R. D. (2005). " Continuous yarns from electrospun fibers." Polymer **46**(8): 2419-2423.

Song, W., D. C. Markel, S. Wang, T. Shi, G. Mao and W. Ren (2012). "Electrospun polyvinyl alcohol-collagen-hydroxyapatite nanofibers: a biomimetic extracellular matrix for osteoblastic cells." Nanotechnology **23**(11): 115101.

Song, W., J. Seta, L. Chen, C. Bergum, Z. Zhou, P. Kanneganti, R. E. Kast, G. W. Auner, M. Shen, D. C. Markel, W. Ren and X. Yu (2017). "Doxycycline-loaded coaxial nanofiber coating of titanium implants enhances osseointegration and inhibits Staphylococcus aureus infection." Biomed Mater **12**(4): 045008.

Song, W., X. Yu, D. C. Markel, T. Shi and W. Ren (2013). "Coaxial PCL/PVA electrospun nanofibers: osseointegration enhancer and controlled drug release device." Biofabrication **5**(3): 035006.

Song Y, Z. S., Li J, Zhao C, Zhang X (2010). "Electrodeposition of Ca-P coatings on biodegradable Mg alloy: in vitro biomineralization behavior." Acta Biomater **6**(5): 1736-1742.

Stadlinger, B., E. Pilling, R. Mai, S. Bierbaum, R. Berhardt, D. Scharnweber and U. Eckelt (2008). "Effect of biological implant surface coatings on bone formation, applying collagen, proteoglycans, glycosaminoglycans and growth factors." J Mater Sci Mater Med **19**(3): 1043-1049.

Sundararaghavan HG, M. R., Burdick JA (2010). "Electrospun fibrous scaffolds with multiscale and photopatterned porosity." Macromol Biosci **10**(3): 265-270.

Szentivanyi, A., T. Chakradeo, H. Zernetsch and B. Glasmacher (2011). "Electrospun cellular microenvironments: understanding controlled release and scaffold structure." Advanced drug delivery reviews **63**(4): 209-220.

Teo, W. E. and S. Ramakrishna (2006). "A review on electrospinning design and nanofibre assemblies." Nanotechnology **17**(14): R89-R106.

Teo, W. E. I., R.; Ramakrishna, S. (2011). "Technological advances in electrospinning of nanofibers." Sci. Technol. Adv. Mater. **12**(1).

Thorvaldsson, A., H. Stenhamre, P. Gatenholm and P. Walkenstrom (2008). "Electrospinning of highly porous scaffolds for cartilage regeneration." Biomacromolecules **9**(3): 1044-1049.

Uccelli, A., F. Frassoni and G. Mancardi (2007). "Stem cells for multiple sclerosis: promises and reality." Regen Med **2**(1): 7-9.

Veronesi F, P. S., Della Bella E, Giavaresi G, Fini M (2014). "Estrogen deficiency does not decrease the in vitro osteogenic potential of rat adipose-derived mesenchymal stem cells." Age (Dordr **36**(3): 9647.

Wang, X., R. A. Gittens, R. Song, R. Tannenbaum, R. Olivares-Navarrete, Z. Schwartz, H. Chen and B. D. Boyan (2012). "Effects of structural properties of electrospun TiO 2 nanofiber meshes on their osteogenic potential." Acta biomaterialia **8**(2): 878-885.

Weber, G. F., M. A. Bjerke and D. W. DeSimone (2011). "Integrins and cadherins join forces to form adhesive networks." J Cell Sci **124**(8): 1183-1193.

Wei, G. and P. X. Ma (2004). "Structure and properties of nanohydroxyapatite/polymer composite scaffolds for bone tissue engineering." Biomaterials **25**(19): 4749-4757.

Wei S. , L. C., Joseph S., David C. Markel, Xiaowei Yu, and Weiping Ren (2017). "Corona Discharge: A Novel Approach To Fabricate Three- Dimensional Electrospun Nanofibers for Bone Tissue Engineering." ACS Biomater. Sci. Eng. **3**(6): 1146-1153.

Weiner S, W. H. (1998). "The material bone: structure mechanical function relations." Annu Rev Mater Sci **28**(271-98).

White, C. A., S. Carsen, K. Rasuli, R. J. Feibel, P. R. Kim and P. E. Beaule (2012). "High incidence of migration with poor initial fixation of the Accolade stem." Clin Orthop Relat Res **470**(2): 410-417.

White CA, C. S., Rasuli K, Feibel RJ, Kim PR, Beaulé PE (2012). "High incidence of migration with poor initial fixation of the Accolade stem." Clin Orthop Relat Res. **470**(2): 410-417.

Xiao, D., Q. Liu, D. Wang, T. Xie, T. Guo, K. Duan and J. Weng (2014). "Roomtemperature attachment of PLGA microspheres to titanium surfaces for implantbased drug release." Applied Surface Science **309**: 112-118.

Xiao, Y., H. Fu, I. Prasadam, Y. C. Yang and J. O. Hollinger (2007). "Gene expression profiling of bone marrow stromal cells from juvenile, adult, aged and osteoporotic rats: with an emphasis on osteoporosis." Bone **40**(3): 700-715.

Yang, F., D. Yang, J. Tu, Q. Zheng, L. Cai and L. Wang (2011). "Strontium enhances osteogenic differentiation of mesenchymal stem cells and in vivo bone formation by activating Wnt/catenin signaling." Stem cells **29**(6): 981-991.

Yokoyama, Y. H., S.; Yoshikawa, C.; Yasuda, Y.; Koyama, H.; Takato, T.; Kobayashi, H. (2009). "Novel wet electrospinning system for fabrication of spongiform nanofiber 3-dimensional fabric." Materials Letters **63**(9-10): 754-756.

Yu, H. S., J. H. Jang, T. I. Kim, H. H. Lee and H. W. Kim (2009). "Apatitemineralized polycaprolactone nanofibrous web as a bone tissue regeneration substrate." Journal of Biomedical Materials Research Part A **88**(3): 747-754.

Zhang, L. and K. G. Ten Hagen (2011). The cellular microenvironment and cell adhesion: a role for O-glycosylation, Portland Press Limited.

Zhang R, M. P. (2000). "Synthetic nano-fibrillar extracellular matrices with predesigned macroporous architectures." J Biomed Mater Res **52**(2): 430-438.

Zhang R, M. P. (2000). "Synthetic nano-fibrillar extracellular matrices with predesigned macroporous architectures." J Biomed Mater Res. **52**(2): 430-438.

Zhang, W., Y. Shen, H. Pan, K. Lin, X. Liu, B. W. Darvell, W. W. Lu, J. Chang, L. Deng and D. Wang (2011). "Effects of strontium in modified biomaterials." Acta Biomaterialia **7**(2): 800-808

ABSTRACT

DEVELOPMENT OF A PROGRAMMED ELECTROSPUN THREE DIMENSIONAL (3D) NANOFIBER COLLECTER AND IT'S APPLICATION TO ORTHOPEDIC IMPLANT COATINGS

by

LIANG CHEN

December 2017

Advisor: Dr. Weiping Ren

Major: Biomedical Engineering

Degree: Doctor of Philosophy

Orthopedic implants might not directly unite with bones especially in compromised patients even if they have been appropriately fixed. The lack of early osseointegration would lead to the failure of the orthopedic implant. A "bone-like" implant surface is urgently needed to accelerate osseointegration. Electrospun nanofiber (NF) is a promising implant coating due to its highly porous nanoscale structure. It mimics the collagen I nanofibrous network of bone tissue; meanwhile it has been widely used as a drug delivery device. However, its compact and dense structure is not ideal for cell growth. Our strategy was to develop a functional three-dimensional (3D) NF implant coating to enhance osseointegration. Firstly, based on a coronal discharge effect 3D polycaprolactone (PCL) NF-zero, -low, -mid, and –high were fabricated by a self-developed automatic 3D NF collector with different collector movement speeds. Simply, the properties of the 3D PCL NFs were altered by the different speeds of the collector movement. The thickness, pore sizes/volumes, porosity and surface

roughness of NFs were proportional to the moving speeds; and the fiber stiffness was increased by a faster movement due to higher fiber crystallinity. Cells should be very sensitive to the changes of living environments. With the aim to investigate how cells choose their preferred environments and to define the optimal NFs for drug release, we cultured pre-osteoblast MC3T3-E1 cells, pre-osteoclast RAW cells and rat adipose derive stem cells (ASCs) on the four types of NFs and studied the proliferation, distribution and differentiation of these cells. The looser structure, higher surface roughness and stiffness of the NF-high enhanced the proliferation and distribution of preosteoblasts and ASCs. Additionally, they had a positive effect on the differentiation of pre-osteoblast cells. Interestingly, the RAW cells preferred the dense NFs and had a higher proliferation. Combining the results above, we chose NF-high as the optimal NF for the drug delivery device study. Finally, we imported PLGA to the previously developed PCL/PVA coaxial system to accelerate degradation and developed strontium doped coaxial 3D PCL/PLGA (1:1)-PVA nanofibers. The coaxial NFs enabled the control of strontium release. The Sr^{2+} was released from the coaxial NFs over 2 months and the concentration was relatively constant. The released Sr^{2+} had a positive effect on the proliferation and differentiation of preosteoblast cells in both indirect cell contact and direct cell contact studies. We believe these coaxial NFs have a great potential as implant coatings. We will test the osseointegration efficiency of NF coated Titanium implants in a rat tibia defect model in the future.

AUTOBIOGRAPHICAL STATEMENT

Liang Chen
Department of Biomedical Engineering
Wayne State University
Detroit, MI 48201
E-mail: ej7518@wayne.edu

EDUCATION

Ph.D Candidate of Biomedical Engineering, December 2017 (expect)
Wayne State University, College of Engineering
Master of Biomedical Engineering, May 2013
Wayne State University, College of Engineering
Bachelor of Biotechnology, July 2010
Harbin Normal University, College of Biology and Chemistry

RESEARCH EXPERIENCE

Molecular/Cell Biology: Cell culture, RT-PCR techniques, flow cytometer, ELISA, western blot, confocal microscopy, fluorescent microscopy, bioreactor system design and dynamic cell culture
Materials: Electrospinning, bio-ceramics and bio-polymer materials fabrication,
materials characterization techniques
Thomas C. Rumble University Graduate Fellowship 2014-2015
Teaching Assistant 2015-2017

PUBLICATIONS

Liang Chen, Wei Song, David C Markel, Tong Shi, Otto Muzik, Howard Matthew1, Weiping Ren, Flow perfusion culture of MC3T3-E1 osteogenic cells on gradient calcium polyphosphate scaffolds with different pore sizes. J Biomater Appl., 908-18, 2016

Song, Wei; **Chen, Liang**; Seta, Joseph; Markel, David; Yu, Xiaowei; Ren, Weiping, "Corona discharge: a novel approach to fabricate three-dimensional electrospun nanofibers, ACS Biomater. Sci. Eng., 2017

Song, Wei; Seta, Joseph; **Chen, Liang**; Bergum, Christopher.; Zhou, Zhubin; Kanneganti, Praveen ; Kast, Rachel ; Auner, Gregory ; Shen, Ming ; Markel, David; Ren, Weiping; Yu, Xiaowei, Doxycycline-loaded coaxial nanofiber coating of titanium implants enhances osseointegration and inhibits Staphylococcus aureus infection, Biomed Mater., 2017

Wei Song, Joseph Seta, Rachel E. Kast, Gregory W. Auner, **Liang Chen**, David C. Markel, Weiping Ren, Influence of Particle Size and Soaking Conditions on Rheology and Microstructure of Amorphous Calcium Polyphosphate Hydrogel. J. Am. Ceram. Soc., 1–12, 2015